UNIVERSITY OF CALIFORNIA,
IRVINE

Multimodal Synaptic Integration in the Posterior Parietal Cortex

DISSERTATION

submitted in partial satisfaction of the requirements
for the degree of

DOCTOR OF PHILOSOPHY

in Biological Sciences

by

Daniel Jun Rindner

Dissertation Committee:
Associate Professor Gyorgy Lur, Chair
Professor Raju Metherate
Professor Katumi Sumikawa

2023

TABLE OF CONTENTS

LIST OF FIGURES iii

LIST OF TABLES v

ACKNOWLEDGEMENTS vi

VITA viii

ABSTRACT OF THE DISSERTATION xi

INTRODUCTION 1

CHAPTER 1: Multi-color optogenetic approaches for studying complex neural circuits
- 1.1 Introduction 21
- 1.2 Methods 25
- 1.3 Results 28
- 1.4 Discussion 32

CHAPTER 2: Cell-type-specific integration of feedforward and feedback synaptic input in the posterior parietal cortex
- 2.1 Introduction 37
- 2.2 Methods 40
- 2.3 Results 50
- 2.4 Discussion 71

CHAPTER 3: Differential persistent firing is a cell-autonomous property of projection-specific layer 5 pyramidal neuron types in the posterior parietal cortex
- 3.1 Introduction 78
- 3.2 Methods 83
- 3.3 Results 86
- 3.4 Discussion 93

SUMMARY 98

REFERENCES 101

LIST OF FIGURES

Figure 1. Simplified schematic of major input and output pathways of the PPC..... 4
Figure 2. Schematic of input and output pathways of layer 5 PT and IT projection neurons..... 13
Figure 3. History, concerns, and testing of multicolor optogenetics..... 22
Figure 4. Stimulus irradiance, duration, wavelength, and opsin choice contribute to crosstalk risk..... 29
Figure 5. A red opsin "lookup table" for maximizing blue stimulus dynamic range..... 31
Figure 6. Dual-color optogenetic approach for selective activation of feedforward and feedback pathways to L5 cells..... 50
Figure 7. Intrinsic membrane properties in IB and RS cells..... 51
Figure 8. Pharmacological approach for testing dual monosynaptic connections..... 52
Figure 9. Dual monosynaptic innervation of layer 5 PPC neurons by feedforward and feedback afferents..... 53
Figure 10. Cell-type-specific nonlinear integration of feedforward and feedback synaptic inputs..... 54
Figure 11. Temporal dynamics of synaptic integration are independent of stimulus order and opsin identity..... 55
Figure 12. Differential involvement of ionic conductances to coincident and delayed integration..... 57
Figure 13. Coincident integration in RS cells is linearized by a feedforward inhibitory circuit..... 59
Figure 14. Internal block of $GABA_A$ receptors uncovers coincident supralinear integration.. 60
Figure 15. Relative kinetics of excitatory and inhibitory currents in RS cells..... 61
Figure 16. Depressing short-term dynamics of feedforward inhibition to RS cells..... 61
Figure 17. Pharmacological testing of IB model predictions..... 62
Figure 18. Integration profiles are stable over extended whole cell recordings..... 62
Figure 19. Cell-type-specific EPSP and NMDA receptor decay kinetics..... 63
Figure 20. Projection-specific labelling of IB and RS cells..... 64
Figure 21. Pharmacological testing of RS model predictions..... 65
Figure 22. Temporal dynamics of action potential output mimic subthreshold feedforward-feedback integration dynamics..... 66
Figure 23. Input specificity of nonlinear synaptic interactions differs between IB and RS cells..... 68
Figure 24. Distribution of feedforward and feedback afferents in PPC..... 69
Figure 25. Synapse location plays a key role in nonlinear interactions..... 70
Figure 26. Feedforward-feedback integration triggers persistent firing in the PPC..... 79
Figure 27. Differential persistent firing in PT and IT neurons in the PPC..... 87
Figure 28. PT and IT neurons do not engage local excitatory recurrent circuits..... 88
Figure 29. Persistent activity is associated with long-lasting increases in intracellular calcium. 90
Figure 30. Potential mechanisms for cell-type-specific persistent firing..... 91

LIST OF TABLES

Table 1. Experimental replicates and statistical test results 30

ACKNOWLEDGEMENTS

Before all, I want to thank my committee chair and graduate advisor, Dr. Gyorgy (Gyuri) Lur. None of the research in this dissertation would be possible without his boundless knowledge and support. Thank you for pushing me in the right (and sometimes wrong) directions, and being my mentor, colleague, and friend as we figure out, together, the best way forward.

To my committee members, both past and present, thank you for your kindness and guidance throughout the years. Dr. Raju Metherate, in an otherwise hectic field, your calm and collected way of doing science served as my ground. When fellowships were unfunded, or papers land with hard reviewers, talking with you reminded me – research is a lifelong pursuit, just keep going. Dr. Katumi Sumikawa, thank you for the endless generosity you have with your reagents, equipment, and time. I always felt your office and lab were open doors, and that our first-floor hallway was a physiologists' dream. I also want to thank Dr. Fan-Gang Zeng, whose ability to enchant his audience with talks is unmatched. You inspire me to use my voice and my science to better the world in ways that no other researcher does. Finally, Dr. Laura Ewell, thank you for being the only faculty member who will "whoop" at my presentations when I mention our paper being published – there should be more. You remind me that the best people make the best scientists, which is perhaps the most valuable lesson of them all.

Thank you to all the members of the Lur lab, Ali Ozgur, Soo Park, Aby Flores, Mikko Oijala, Dr. Hyeijung Yoo, and all others, for making the days (and sometimes nights) in lab bright no matter what the hour. Dr. Archana Proddutur, thank you for normalizing my love of synapses. Going back and forth on what we think our data means has been some of the most intellectually stimulating and cherished parts of graduate school.

I also want to thank the UCI Center for Hearing Research, and particularly Dr. Michelle Kapolowicz, who gave me a "home away from home" in a side of campus I would otherwise never see. Thank you also to the Department of Neurobiology and Behavior staff, who keep the show running. Naima Louridi, Maggie Davis, Joann Lozano, Tina Dominguez, our department would fall apart without you.

To my family, and those I love, thank you for being there with me through it all. You are the reason this work was completed, and no amount of thanks is enough.

Lastly, I want to acknowledge the institutions who believed in our science, and invested in our team and our research. Funding for the work in this dissertation was provided by the Whitehall Foundation (Grant# 2018-12-09), the National Institute of Mental Health (Grant# R01MH123686), the National Institute of Neurological Disorders and Stroke (Grant# R01NS127785), and the National Institute on Deafness and Other Communication Disorders (Grant# T32DC010775).

Parts of Chapter 1 of this dissertation is a reprint of the material as it appears in Rindner, D.J., Lur, G., 2023. Practical considerations in an era of multicolor optogenetics. Frontiers in Cellular Neuroscience 17, used with permission from Frontiers Media S.A.. The co-author listed in this publication is Gyorgy Lur, who supervised the research.

Parts of Chapter 2 of this dissertation is a reprint of the material as it appears in Rindner, D.J., Proddutur, A., Lur, G., 2022. Cell-type-specific integration of feedforward and feedback synaptic inputs in the posterior parietal cortex. Neuron 110, 3760-3773.e5, used with permission from Elsevier Inc.. The co-author Archana Proddutur listed in this publication was a crucial collaborator in this project, and co-author Gyorgy Lur supervised the research.

Thank you all.

VITA

Daniel Jun Rindner

EDUCATION

University of California, Irvine — Irvine, CA
Ph.D., Biological Sciences (focus: Neuroscience) — 2023

Tohoku University — Sendai, Japan
M.S., Developmental Biology and Neuroscience — 2018

University of California, San Diego — La Jolla, CA
B.S., Biochemistry and Cell Biology — 2016

RESEARCH

University of California, Irvine — Irvine, CA
Graduate Student Researcher, Advisor: Dr. Gyorgy Lur — 2018 - 2023
Thesis: Multimodal synaptic integration in the posterior parietal cortex

- Built electrophysiology rig with multi-color imaging and stimulation capabilities to interrogate interactions of auditory, visual, and frontal synapses in mouse brain slices.
- Designed *in vitro* pharmacological tests to evaluate *in silico* model predictions.
- Custom-wrote all electrophysiology data analysis code in Python.
- Employed viral methods and transgenic animal models for inducing pathway-specific opto- and chemogenetic construct expression.
- Secured NIDCD T32 grant and submitted F31 application receiving a favorable impact score of 32.

Tohoku University — Sendai, Japan
Graduate Student Researcher, Advisor: Dr. Daisuke Yamamoto — 2016 - 2018
Thesis: Role of sex-specific gene fruitless *in regulating* D. melanogaster *courtship neuron excitability*

- Identified differential modulation of delayed-rectifier and A-type K^+ currents by social experience in *fruitless* loss-of-function mutants.
- Explored candidate channel mediators via *in vivo* patch clamp in K^+ channel subtype loss-of-function mutants.
- Determined putative neuromodulatory synaptic partners using GRASP fluorescence imaging.

Salk Institute for Biological Studies — La Jolla, CA
Undergraduate Intern, Advisor: Dr. Kenta Asahina — 2016

- Designed and optimized behavioral assay to screen for aggression in *D. melanogaster.*
- Trained an automated behavior classifier to increase screening throughput.

RESEARCH (Cont.)

Tohoku University — Sendai, Japan
Research Exchange Student, Advisor: Dr. Kensaku Mizuno — 2014 - 2015

- Investigated role of Rho-GEF Solo in regulating actin/keratin networks and cell adhesion complexes during epithelial cell migration.
- Daily use of standard molecular biology techniques (transfection, siRNA knockdown, western blot).
- Cultured MDCK cells in 3D gel matrix to test role of Solo during tubule formation.

Qualcomm Institute — La Jolla, CA
Undergraduate Intern, Advisor: Dr. Jacqueline Kerr — 2013 - 2014

- Aided development of early detection system for behavioral correlates of unhealthy aging.
- Managed longitudinal dataset of physical activity levels in study participants.

TEACHING

Teaching assistant, Graduate course: "Cellular Neurobiology Lab", *UCI*	2022
Teaching assistant, Undergraduate course: "Hearing and the Brain", *UCI*	2022
Teaching assistant, Undergraduate course: "Neurobiology Lab", *UCI*	2020

MENTORSHIP

Coursework mentor, Graduate student peers, *UCI INP*	2020
Techniques mentor, Graduate rotation students, *Lur Lab*	2019
Research mentor, UCI undergraduate student, *Lur Lab*	2019-2020

LEADERSHIP AND OUTREACH

Lead Organizer, Weekly Journal Club, *UCI CHR*	2021-2023
Graduate Student Representative, *UCI INP*	2019-2021
Graduate Student Ambassador, *UCI CNLM*	2018-2020
K-6 Class Teacher, Anatomy and Physiology, *CodeNinjas Long Beach, CA*	2018-2019

HONORS AND AWARDS

Howard A. Schneiderman Fund Award, *UCI School of Biological Sciences*	2023
Best Poster Award (Honorable Mention), *Optogenetics Gordon Research Conference*	2022
Graduate Travel Award, *UCI School of Biological Sciences*	2022
NIDCD T32 Predoctoral Fellowship, *UCI CHR*	2019-2022
Business Pitch Competition Second Place, *UCI Beall Applied Innovation*	2021
Jared M. Roberts Memorial Award, *UCI CNLM*	2021
Selected Participant, Advanced Imaging, *Leibniz Institute for Neurobiology, Germany*	2021
Monbukagakushō Scholarship, *Japanese Ministry of Education*	2016-2018
$1 Million Scholarship Initiative, *UC Education Abroad Program*	2014

PEER-REVIEWED PUBLICATIONS

First author

1. Rindner DJ, Lur G. Practical considerations in an era of multicolor optogenetics. *Front. Cell. Neurosci.* 2023, 17:1160245.

2. Rindner DJ, Produttur A, Lur G. Cell-type-specific integration of feedforward and feedback synaptic inputs in the posterior parietal cortex. *Neuron.* 2022*,* 110:2, 3760-3773.e5.

Co-author

3. Chen Y-C, Rindner DJ, Fowler JP, Lallai V, Hnasko T, Demuro A, Lur G, Fowler CD. Extracellular ATP neurotransmission and nicotine sex-specifically modulate habenular neuronal activity in adolescence. *In submission.*

4. Nave C, Roberts R, Hwu P, Estrella J, Vo T, Nguyen T, Pervolarakis N, Bui T, Rindner DJ, Shaw P, Leise T, Holmes T. Weekend light shifts evoke Drosophila circadian neural network desynchrony. *J. Neurosci*. 2021, 3074-19

5. Isozaki Y, Sakai K, Kohiro K, Kagoshima K, Iwamura Y, Sato H, Rindner D, Fujiwara S, Yamashita K, Mizuno K, Ohashi K. The Rho-guanine nucleotide exchange factor Solo decelerates collective cell migration by modulating the Rho-ROCK pathway and keratin networks. *Mol. Bio. Cell.* 2020, 31:8.

SELECT PRESENTATIONS

Posters

1. Rindner DJ, Proddutur A, Lur G. Cell-type specific nonlinear interactions of top-down and bottom-up synaptic inputs to the posterior parietal cortex. *Optogenetics Gordon Research Conference*. 2022.
2. Rindner DJ, Lur G. Cell-type specific nonlinearities of multi-modal inputs to posterior parietal cortex. *Neuroscience 2021*.
3. Rindner DJ, Lur G. Audio-frontal synaptic integration in the posterior parietal cortex. *Center for Hearing Research Annual Symposia.* 2019.
4. Rindner DJ, Hara Y, Yamamoto D. Experience-dependent non-synaptic plasticity in Drosophila central brain neurons. *Annual Meeting of the Japan Neuroscience Society*. 2018.
5. Rindner DJ, Mizuno K. Role of Rho-GEF Solo on epithelial collective cell migration. *Tohoku University International Scholarship Poster Session*. 2015.

Invited Talks

6. Rindner DJ, Proddutur A, Lur G. Cell-type specific nonlinearities of multimodal inputs to posterior parietal cortex. *UCI Dept. Anatomy and Neurobiology Progress in Neurobiology Seminar Series*. 2021
7. Rindner DJ, Lur G. Cell-type specific synaptic integration of feed-forward and feed-back afferents in the posterior parietal cortex. *UCI Dept. Neurobiology and Behavior, Neuroblitz*. 2021.
8. Rindner DJ, Lur G. Multimodal integration in the mouse posterior parietal cortex. *UCI Dept. Neurobiology and Behavior, Neuroblitz*. 2019.

ABSTRACT OF THE DISSERTATION

Multimodal Synaptic Integration in the Posterior Parietal Cortex

by

Daniel Jun Rindner

Doctor of Philosophy in Biological Sciences

University of California, Irvine, 2023

Associate Professor Gyorgy Lur, Chair

Integration of feedforward and feedback synaptic input is a core feature of neural circuits. Proper interaction between these pathways is critical for nearly all cognitive processes, ranging from basic sensory perception to goal-oriented behaviors including decision making, learning, attention shifting, and working memory. Due to a technical inability to selectively manipulate feedforward and feedback synaptic pathways, previous efforts to examine their interaction rely on passive measures of neural activity in human and other animals, revealing a signature, transient enhancement of neural signals during periods of top-down control. In a largely non-overlapping body of work, detailed studies of dendritic physiology have uncovered basic mechanisms underlying nonlinear enhancement of synaptic input, albeit largely agnostic to input identity. Taking advantage of recent advances in multicolor optogenetics, my thesis aims to uncover cellular mechanisms which explain the neural enhancement observed during top-down modulation. In Chapter 1, I report procedural improvements to a dual-color optogenetic approach for selectively stimulating feedforward and feedback afferents. I demonstrate an exhaustive test of experimental parameters influencing crosstalk, and lastly propose a “lookup table” strategy which minimizes cross-activation of synaptic pathways. Next, in Chapter 2 I explore how deep-layer neurons integrate synaptic input from feedforward and feedback sources, using dual-color

optogenetics to expand on decades of synaptic integration work based on electrical stimulation methods. I show that layer 5 pyramidal cells in the posterior parietal cortex (PPC) receive monosynaptic dual innervation, combining inputs from sensory and frontal cortex. I then describe the distinct temporal dynamics by which subclasses of layer 5 pyramidal neurons integrate these synapses. Specifically, regular spiking (RS) cells exhibit supralinear enhancement of delayed, but not coincident inputs, while intrinsic burst firing (IB) neurons selectively boost coincident synaptic events. In explanation of this difference, I next present pharmacological and computational modelling data collected in collaboration with a postdoc in the Lur lab, indicating that distinct integration profiles arise from a cell-type specific interaction of ionic mechanisms and feedforward inhibition. Finally, in Chapter 3 I address how nonlinear enhancement of converging synaptic pathways may generate persistent firing, a neural hallmark of working memory in the PPC. In this Chapter I mimic the effect of optogenetically-evoked synaptic input via direct electrical activation of single cells, showing that projection-specific cells corresponding to RS and IB subtypes have differential propensity for persistent firing. Namely, cells corresponding to the IB subtype display longer-lasting, higher-frequency spike firing than RS during periods of sustained activation, which was not driven by differences in network connectivity between the cell types. I end with speculation of the intrinsic mechanisms which may position IB cells as preferentially engaged during periods of persistent firing.

INTRODUCTION

Cognitive role of feedforward-feedback interactions

Brain regions are organized hierarchically, with anatomical connections permitting information flow in both "bottom-up" and "top-down" directions. At the "bottom" of this hierarchy are sensory receptor cells, responsible for the initial transformation of external cues to electrical signals. This signal is sent via feedforward afferents, to be filtered and interpreted by higher brain structures such as visual, auditory, or somatosensory cortices dedicated to processing one sensory domain. In turn, domain-unspecific regions at the "top" – such as the prefrontal cortex, cingulate cortex, and hippocampus – send information related to internal state to lower brain areas via feedback projections, forming a reciprocal processing loop responsible for nearly all aspects of human cognition.

The importance of feedback in modulating feedforward processing has been clear for many decades. Top-down factors including motivation (Sanford, 1936), attitude (Zajonc, 1968), and memory (Bugelski and Alampay, 1961) have all been shown to alter sensory perception in humans. Given the sensitivity of perception to top-down influence it is perhaps unsurprising that patients diagnosed with disorders classically associated with decreased cognitive function – Alzheimer's disease (AD) (Gates et al., 1995; Waldton, 1974), Schizophrenia (Adler et al., 1982; Jeon and Polich, 2003; Moberg et al., 2006), Attention-deficit hyperactivity disorder (ADHD) (Ghanizadeh et al., 2012; Mangeot et al., 2001), and post-traumatic stress disorder (PTSD) (Cisler et al., 2011; Jedlicka and Zhen, 2023; Olatunji et al., 2015) – often co-present with deficits in sensory processing that persist across modalities and are independent of basic sensory

thresholds. Perceptual abnormalities thus likely arise from a dysfunctional interaction of feedback signals with otherwise typical feedforward sensory information.

Central position of posterior parietal cortex within a cortical hierarchy

Human neuroimaging studies of higher cognitive function often implicate activity of frontal and parietal areas, particularly prefrontal (PFC) and posterior parietal cortices (PPC) (Braver et al., 2003; Dosenbach et al., 2007, 2006; Sheffield et al., 2015). Together, these regions comprise a frontoparietal network first proposed by Dosenbach et al. 2007 based on their functional connectivity in the resting state (Dosenbach et al., 2007). Activity correlations between frontal and parietal network nodes increase during periods of top-down control (Buschman and Miller, 2007; Haegens et al., 2010; Zanto et al., 2011), which has been linked to cognitive processes of attention (Greenberg et al., 2010; Serences et al., 2004; Szczepanski et al., 2010), working memory (Bunge et al., 2003; Jerde et al., 2012; Salazar et al., 2012), and decision making (Pesaran et al., 2008; Rens et al., 2017; Thimm et al., 2012). Moreover, the strength of frontoparietal network connectivity has been shown to positively correlate with certain intelligence metrics (Sheffield et al., 2015). As such, the frontoparietal network has been proposed to represent one of several central control systems for cognitive function (Marek and Dosenbach, 2018).

Despite having highly correlated activity patterns, frontal and parietal areas have dissociable roles in cognition and position in a cortical hierarchy. A classic study by Brenda Milner demonstrates that patients with frontal, but not parietal, lobe lesions have difficulty shifting between alternating task rules (Milner, 1963). A later study using a visual search task

showed that activation of frontal areas is stronger during top-down (goal-driven) search, while activation of parietal regions is stronger during bottom-up (stimulus-driven) capture of attention (Li et al., 2010). Furthermore, using the same task as Li et al. 2010, Buschman and Miller showed that neurons in the non-human primate PFC encode target location roughly 150 ms before the PPC during top-down search (Buschman and Miller, 2007). This sequence of activation reverses during bottom-up attention capture, during which posterior parietal regions encode target location roughly 100 ms before frontal areas (Buschman and Miller, 2007). These data are consistent with a hierarchical model of brain organization, and support the notion that the parietal regions are "below" frontal cortex, providing an input pathway for sensory information to interact with the frontoparietal control network.

Detailed anatomical studies in rodents also support the central hierarchical position of PPC between PFC and sensory cortices. However, the existence of a "true" PFC in rodents has been the subject of much debate, and a consensus opinion of which anatomical regions do – or would – constitute this region remains unreached (Laubach et al., 2018). Rather, functions of human PFC seem distributed between other "frontal" regions in the rodent brain, particularly the prelimbic/infralimbic (PL/ILA), orbitofrontal (OFC), and anterior cingulate cortices (ACC) (Preuss, 1995; Seamans et al., 1995). Despite this, anatomical mapping of projections to and from PPC provides valuable insight to the function of these highly interconnected brain areas (Figure 1). Systematic retro- and anterograde tracer injections have repeatedly shown densest feedback projections to PPC from ACC (Wilber et al., 2014; Zhang et al., 2016; Zingg et al., 2014), suggesting that top-down input from ACC is distinctly important for modulating PPC function (Figure 1). Notably, there exists also a clear bias in the strength of sensory innervation of PPC over other association (retrosplenial (RSC), temporal association (TEA), and entorhinal

(ENT)) and frontal areas (Wilber et al., 2014; Zhang et al., 2016; Zingg et al., 2014). In fact, PPC has privileged access to sensory information, remaining the only non-canonical sensory cortical region to have direct, convergent innervation by all auditory (AUD), visual (VIS), and somatosensory (SOM) cortices (Zhang et al., 2016; Zingg et al., 2014). Furthermore, alternative, more direct pathways for sensory information to reach the PPC from thalamic relay stations – lateral geniculate (LGN), medial geniculate (MGN), ventral posteromedial nucleus (VPM) – are hardly found (Cappe et al., 2009; Chandler et al., 1992). However, recent open-source neural tracing data published by the Allen Institute for Brain Science suggest that limited projections from LGN to postero-medial portions of the PPC (also referred to as Oc2) can be found ("Projection :: Allen Brain Atlas: Mouse Connectivity," n.d.), although the anatomical

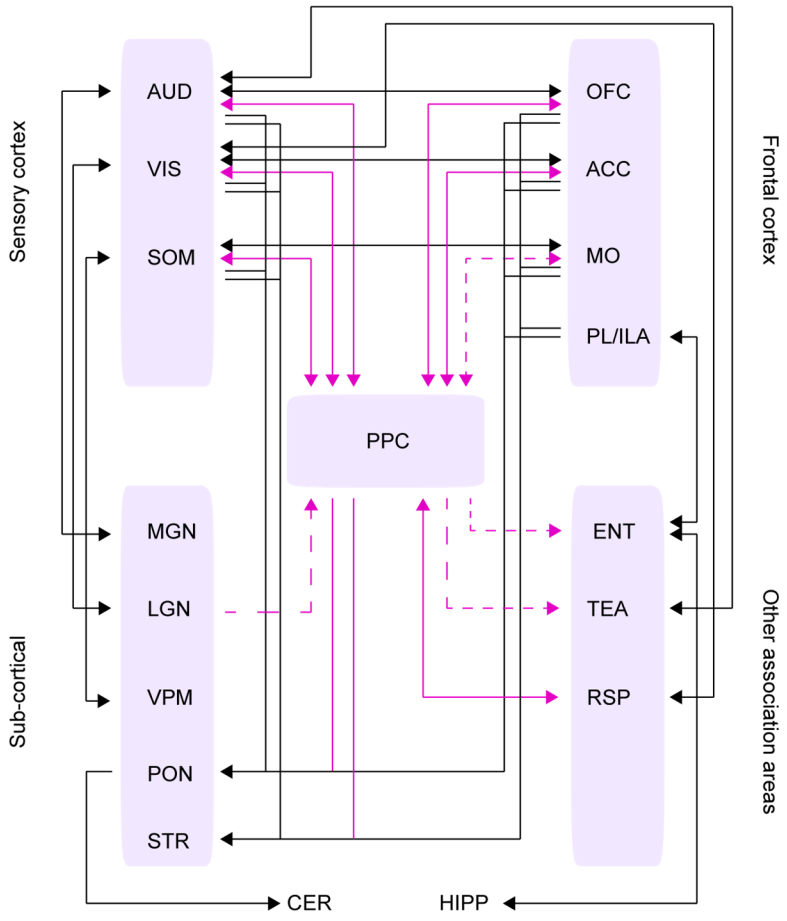

Figure 1. Simplified schematic of major input and output pathways of the PPC. Dark arrows represent known pathways bypassing the PPC. Purple arrows depict pathways either from or to the PPC. Dotted arrows indicate relatively weak pathways. ACC, anterior cingulate cortex; AUD, auditory area; CER, cerebellum; ENT, entorhinal cortex; HIPP, hippocampus; LGN, lateral geniculate nucleus; MGN, medial geniculate nucleus; MO, motor cortex; OFC, orbitofrontal cortex; PL/ILA, prelimbic/infralimbic area; PON, pons; PPC, posterior parietal cortex; RSP, retrosplenial cortex; SOM, somatosensory area; STR, striatum; TEA, temporal association area; VIS, visual area; VPM, ventral posteriomedial nucleus. Data referenced from Chandler et al. 1992, Cappe et al. 2009, Wilber et al. 2014, Zhang et al. 2016, Zingg et al. 2014, Projection: Allen Brain Atlas: Mouse Connectivity, n.d..

classification of this region as part of PPC is still debated (Palomero-Gallagher and Zilles, 2015; Whitlock et al., 2008). Thalamocortical input from non-principal sensory thalamic regions including known projections from the lateral posterior and pulvinar nuclei may also transmit multisensory information to PPC (Cappe et al., 2009; Gharbawie et al., 2010). Nevertheless, the density of direct feedforward projections from sensory cortex indicate that these cortico-cortico pathways represents a substantial source of high-level sensory input to PPC.

Feedforward-feedback integration in the posterior parietal cortex

The role of parietal areas as an integrative "hub" for feedforward and feedback information is moreover supported by clinical evidence in human patients with parietal cortex lesions. Patients with parietal damage present with impaired working memory (Koenigs et al., 2009; Mackey et al., 2016; Warrington et al., 1971) and visuospatial navigation (Ciaramelli et al., 2010; Wilson et al., 2005). Deficits in contextual sensory processing (Walter and Dassonville, 2008), sensorimotor transformation (Desmurget et al., 2009, 1999; Ro et al., 2001; Snyder et al., 1997), and mapping sensory cues in egocentric space (Lacquaniti et al., 1995; Murphy et al., 2016; Wilson et al., 2005) may reasonably underly these indications, however the precise role of PPC in these cognitive processes is still an area of active investigation. In support of a role for PPC in sensory-spatial binding, lesions of the parietal cortex result in neglect (Mesulam, 1999; Tanaka et al., 1999), a condition characterized by a reduced awareness towards the contralateral sensory space (Bisiach and Luzzatti, 1978; Hjaltason et al., 1996). Similarly to in AD, Schizophrenia, ADHD, and PTSD, PPC lesion-induced cognitive impairments are not explained by "pure" sensory deficits, as other measures of sensory processing (for example, pure tone audiometry)

show normal levels even with such lesions (Tanaka et al., 1999). Rather, behavioral manifestations are consistent with an impaired attentional process resulting in an inability for sensory information to enter conscious space. Furthermore, there is evidence that certain elements of unconscious visual processing remain intact in patients with neglect (Berti and Rizzolatti, 1992). Thus, parietal areas likely have a higher-order role in sensory processing involving the conscious evaluation (for example, feature abstraction and categorization) of sensory information, rather than a downstream role in engaging specific motor programs in response to sensory input. In support of this theory, work in non-human primates using a visual saccade task recently demonstrated that PPC inactivation preferentially impairs monkeys' ability to discriminate visual stimuli rather than the downstream initiation of a saccade response (Zhou and Freedman, 2019).

Indeed, neuroimaging and electrical recording efforts in humans (Chivukula et al., 2021; Regev et al., 2018) and other animals (Goard et al., 2016; Lohuis et al., 2022; Olcese et al., 2013; Pho et al., 2018; Zhong et al., 2019) indicate that PPC is engaged by a range of sensory stimuli. Yet, such studies often measured "sensory" responses when stimuli encoded information relevant for a behavioral task, and thus represents a highly multiplexed signal combining sensory and feedback cues related to the subject's internal demands. Several recent studies suggest that interactions of such feedforward sensory and feedback information streams are important for PPC function. One such study used transient inactivation of the rodent PPC to show that activity in this area is important for the categorization of new auditory stimuli (Zhong et al., 2019). However, PPC inactivation did not inhibit perception of the stimulus itself, as categorization of learned stimuli was not sensitive to PPC manipulations (Zhong et al., 2019), suggesting that sensory processing in PPC is highly dependent on behavioral context. In a second particularly

notable study, Pho et al. directly compared activity in primary visual cortex (V1) and PPC in mice during both passive and task-engaged states. They demonstrate that while V1 exhibits visual responses to viewing in both behavioral conditions, PPC responses are selectively gated by their importance to the task (Pho et al., 2018). In fact, while a topographic representation of the visual field was for many years considered absent in human parietal areas, such organization is observed when the mapping task involves storing the visual location in working memory (Sereno et al., 2001). Dynamic, task-dependent encoding of stimulus properties have also been extensively described in monkeys (Fanini and Assad, 2009; Ibos and Freedman, 2014; Sarma et al., 2016; Stoet and Snyder, 2004; Toth and Assad, 2002). For example, PPC neurons have been demonstrated to shift between color and location (Toth and Assad, 2002) or direction response (Ibos and Freedman, 2014) tunings based on task demands. Together, these studies indicate that sensory encoding in PPC is flexible, and furthermore governed by top-down contextual influence.

What is the source of these top-down modulatory cues? As anatomical evidence suggests, a major source of feedback to PPC is from the ACC. The ACC is most commonly associated with prediction error monitoring (Gehring and Willoughby, 2002), selective attention (Pardo et al., 1990; Totah et al., 2009; Weissman et al., 2006) and working memory (Osaka et al., 2004; Otsuka et al., 2006). Visual attention tasks increase coherence between ACC and PPC in primates (Buschman and Miller, 2007), suggesting that the coordinated activity of ACC and PPC is important for cognitive control. Transient reductions in ACC activity have been proposed to underly momentary lapses in attention, thereby contributing to trial-by-trial variance in behavior performance (Weissman et al., 2006). Indeed, chemical inactivation of ACC in rodents appears to causally regulate attention and susceptibility to visual distractors in rodents (Kim et al., 2016; Koike et al., 2016). In general terms, frontal areas are thus thought to primarily provide top-

down information including selective attention, context, and behavioral rules(Koechlin et al., 1999; Miller and Cohen, 2001; Milner, 1963; Suzuki and Gottlieb, 2013). Parietal areas then integrate this information with incoming sensory evidence to guide future action (Bunge et al., 2003; Rowe et al., 2008). Based on both anatomical and functional evidence, the rodent PPC appears to represent a homolog of PPC in humans. Furthermore, given its strong innervation by sensory and frontal regions, and functional role in higher-level sensory processing, the PPC represents an ideal model region for studying the mechanistic interactions of feedforward and feedback pathways.

Multimodal enhancement of neural activity

Feedforward-feedback interactions have been studied extensively in the human brain. The bulk of such studies focus on mechanisms of selective attention, due to the relative ease of instructing top-down attention in human subjects. In general, the effect of attentional feedback from higher brain areas either enhances (Flevaris and Murray, 2015; Fritz et al., 2003; Warren et al., 2014) or suppresses (Gazzaley et al., 2005a, 2005b; Pinsk et al., 2004) bulk neural activity (measured via whole-brain imaging or electrical recording techniques with relatively low spatiotemporal resolution) in lower brain regions. Single unit recordings in monkey visual areas suggest that attentional feedback increases stimulus-evoked spike responses, without changing the neuron's receptive field or stimulus preferences (McAdams and Maunsell, 1999). An important recent study showed that optogenetic activation of cingulate cortex enhances stimulus-evoked spiking responses in the primary visual cortex (V1) and improves behavioral visual discriminability in mice (Zhang et al., 2014). Notably, in Zhang et al., optogenetic activation of the mouse cingulate

cortex was performed at levels which do not produce suprathreshold responses in downstream V1 neurons (Zhang et al., 2014). Thus, two mechanistic explanations could theoretically explain the visual stimulus-evoked enhancement seen in V1 cells. One possibility is simply that tonic activation of cingulate cortex provides a source of background excitation of V1 neurons, resulting in these cells sitting closer to action potential threshold. An alternative possibility is that subthreshold synaptic input from cingulate fibers is nonlinearly integrated with feedforward signals from visual thalamus. Nevertheless, these data and that from other studies indicate that synaptic signals encoding attentional demand interact with feedforward sensory information in lower brain areas, resulting in increased spiking activity in local neurons. However, the precise mechanism by which these multimodal synaptic pathways interact are not well understood.

The notion that input from one pathway can directly influence response to another has its origins in multi-sensory integration, and now-classic experiments on audio-visual integration done by M. Alex Meredith and Barry Stein. One of their early *in vivo* observations was a nonlinear enhancement of neural responses in the cat superior colliculus to simultaneously presented auditory and visual cues, which were many times greater than the simple summation of spiking responses to each stimulus (Meredith and Stein, 1996, 1983). In extreme cases, cells appeared to not respond to either sensory modality, but responded robustly only when both stimuli were presented simultaneously (Meredith and Stein, 1996, 1983). Similar enhancement of multisensory input is observed elsewhere in the brain, including in neurons of the cat anterior ectosylvian sulcus (Wallace et al., 1992) and more recently in the mouse PPC (Olcese et al., 2013). These findings suggests that an active process exists that specifically amplifies neural activity to multimodal input, the effect of which is the improved speed and likelihood of detecting a multisensory event (Bell et al., 2005; Diederich and Colonius, 2004; Frens et al.,

1995; Nozawa et al., 1994). Such a mechanism may involve a specialized circuit motif, or synaptic integration in individual cells. Which of these mechanisms are engaged during multisensory integration, and whether the same mechanisms are involved in the integration of feedforward and feedback inputs is unknown.

Dendritic integration: Fundamental principles and evidence of *in vivo* function

Decades of work has established that neuronal dendrites are highly dynamic sites for synaptic integration, capable of performing a wide array of nonlinear computations including supralinear enhancement of precisely timed synaptic inputs. Dendritic nonlinearities have been reported *in vivo* (Helmchen et al., 1999; Suzuki and Larkum, 2017; Xu et al., 2012), and previously suggested to enable context-dependent sensory coding (Larkum et al., 1999; Xu et al., 2012). Dendrites have enormous computational power, owing to a wealth of voltage-dependent channels expressed in dendritic membranes. These active mechanisms can result in nonlinear voltage events called dendritic spikes first reported in brain slice preparations in cerebellar neurons (Llinás et al., 1968) and later demonstrated in cortical (Polsky et al., 2004; Schiller et al., 1997) and hippocampal (Losonczy and Magee, 2006; Takahashi and Magee, 2009) cells. Dendritic spikes result from the rapid opening of voltage-gated ion channels, and provide a robust mechanism for supralinear enhancement of synaptic input. Several voltage-gated channel conductances have been implicated in dendritic spikes, including calcium channel (Losonczy and Magee, 2006; Schiller et al., 1997), sodium channel (Golding and Spruston, 1998; Kim and Connors, 1993), and NMDA receptor conductances (Losonczy and Magee, 2006; Polsky et al., 2004). The generation of dendritic spikes is highly dependent on the timing (<250 ms)

(Gasparini et al., 2004; Takahashi and Magee, 2009) and location (within a dendritic branch) (Gasparini et al., 2004; Polsky et al., 2004) of synaptic inputs along the dendritic process. Dendritic activity is usually relatively localized (Palmer et al., 2014), however dendritic spikes can have a measurable impact on the spiking activity at the soma. This was first predicted in computational modeling studies (Traub et al., 1991), and later confirmed in acute slices (Larkum et al., 1999; Schiller et al., 1997). Still, dendritic spikes initiated in apical dendrites often fail at branch points due to sudden increases in input impedance (Goldstein and Rall, 1974; Jarsky et al., 2005; Manor et al., 1991), and are therefore unreliable messengers of distal synaptic activity for the cell soma (Golding and Spruston, 1998). However, simultaneous input to more proximal dendritic segments can allow forward propagation of the dendritic spike to the cell body (Jarsky et al., 2005). Thus, convergent synaptic input to different regions of the dendritic tree can nonlinearly influence somatic spiking in two ways – first, by increasing the likelihood of generating a dendritic spike, and second, by allowing the passage of such nonlinear dendritic voltage events to the soma. In addition to supralinear dendritic spikes, several sublinear processes have also been reported in pyramidal cell dendrites (Abrahamsson et al., 2012; Cash and Yuste, 1999; Kim et al., 1995; Larkum et al., 1999; Tran-Van-Minh et al., 2016). The wide array of nonlinear computations present in neuronal dendrites make them likely sites of integration for feedforward and feedback information pathways.

There is evidence, albeit limited, that neuronal dendrites are involved in integrating top-down and sensory signals *in vivo*. Sensory input can trigger nonlinear dendritic events in pyramidal neurons of primary sensory regions, including NMDA (Palmer et al., 2014; Smith et al., 2013) and sodium spikes (Smith et al., 2013). Top-down signals in the cortex are classically thought to target apical dendrites in cortical layer 1 (L1) (Kaas et al., 1977; Markov et al., 2014;

Rockland and Pandya, 1979; Tigges et al., 1977). In a particularly impressive study, Palmer et al. used two-photon calcium imaging to test dendritic response of pyramidal neurons in somatosensory cortex when stimulating the hindpaw, L1, or paired stimulation of both (Palmer et al., 2014). While electrical activation of L1 induced no response and hindpaw stimulation only mild responses, co-activation induced large calcium transients at significantly higher frequency than either stimulus alone (Palmer et al., 2014). Furthermore, co-stimulation-induced calcium signals were absent in the presence of an NMDA receptor antagonist, suggesting that NMDA spikes (and the underlying changes in calcium influx) are important for the association of feedforward and feedback synaptic input. In a second notable study, Xu et al. demonstrate that dendritic calcium spikes in the barrel cortex are triggered only when whisker deflections coincide with periods of active whisking (a top-down process likely involving feedback from motor association areas) (Xu et al., 2012). Nevertheless, mechanisms by which synaptic input from feedforward and feedback pathways interact is far from known.

Cell types in layer 5 of the neocortex

The neocortex is a highly stratified and genetically diverse structure, with complex wiring principles and intrinsic electrophysiological features which are likely to impact synaptic integration. Indeed, even the concept of distinct cortical “layers” has been argued as misleading, as such a cell body-centric classification scheme (i.e. “ layer 5 cells”) fails to capture the true functionally relevant processing regions (dendrites, axons) of neurons, which are rather distributed across multiple “layers” (Larkum et al., 2018). Even within a cortical layer, many distinct cell types are found, including non-excitable glial cells, and GABAergic inhibitory and

glutamatergic excitatory pyramidal neurons. Most of the examination of dendritic integration was performed in neurons in layer 5 (L5), owing to their relatively large apical dendrite accessible for intracellular recording. L5 cells extend dendrites throughout the entire cortical column (Chagnac-Amitai et al., 1990; Yang et al., 1996), and is thought to compose a distinct "output" layer of cortex, as their axons ramify to cortical and non-cortical targets (Kim et al., 2015). L5 cell types have furthermore been classified by their electrophysiological features and genetic profiles (Chagnac-Amitai et al., 1990; Connors et al., 1982; Dembrow et al., 2010, 2010; Gao and Zheng, 2004, 2004; Harris and Shepherd, 2015; Hattox and Nelson, 2007; Kasper et al., 1994; Kim et al., 2015; Larkman and Mason, 1990; Mason and Larkman, 1990; Morishima et al., 2011; Yang et al., 1996). From these classification schemes, two broad categories of cell types in L5 emerge. The first are intratelencephalic (IT) neurons, which send axons to contralateral cortical regions and have tonic action potential firing patterns (and are thus also referred to as regular spiking, or "RS" neurons) (Figure 2). The second are pyramidal tract (PT) neurons (also referred to as extratelencephalic, or "ET"), which project outside the telencephalon to the spinal

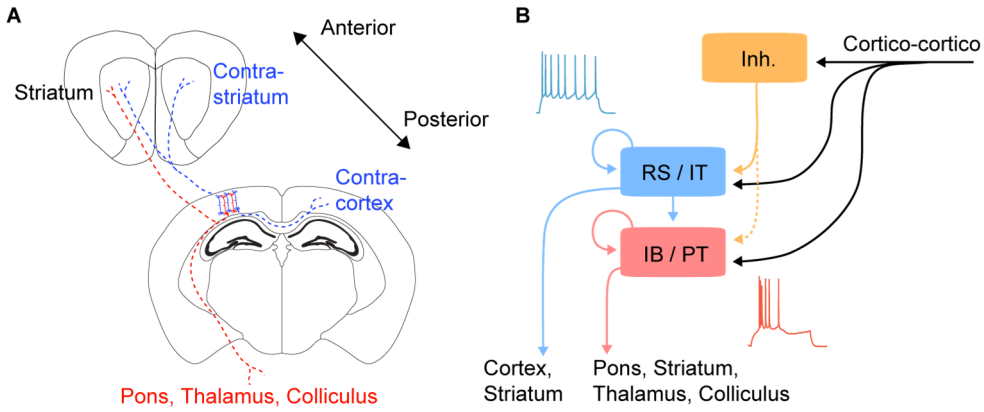

Figure 2. Schematic of input and output pathways of layer 5 projection neurons. (**A**) Diagram of pyramidal tract (PT, red) and intratelencephalic (IT, blue) neurons in an acute slice of PPC (bottom). PT and IT projection targets are shown. (**B**) Local circuit connectivity of PT and IT neurons, including inhibitory (Inh., orange) and excitatory cortico-cortico inputs (black). Insets display representative firing patterns of PT (red) and IT (blue) neurons. A classification scheme based on firing pattern often refer to PT and IT subtypes as intrinsically bursting (IB) or regular spiking (RS), respectively.

cord and brainstem, and have the propensity to fire bursts of action potentials (and are thus also referred to as intrinsically bursting, or "IB" neurons). The exact method used by each study for identifying IT/RS or PT/IB cell types – either retrograde fluorescent labelling or from their firing responses to direct current injection – determines the precise term used to classify each. However, anatomical and electrophysiological phenotypes are highly correlated and thus either label is commonly accepted to refer to the same neural population.

IT and PT neurons can have complex projection targets, with the same neuron innervating multiple cortical, sub-cortical, and extratelencephalic regions (Hooks et al., 2018; Peng et al., 2021). For example, while PT neurons are defined by their extratelencephalic projections, many also project to regions within the telencephalon, including the thalamus and striatum (Baker et al., 2018; Kim et al., 2015), which can have distinct roles in behavior (Takahashi et al., 2020). The location of IT and PT fibers also overlap in the striatum, suggesting that these cells represent parallel channels of information flow to sub-cortical targets (Hooks et al., 2018). While PT neurons are highly restricted to deep layer 5, IT neurons are also found in other layers of the cortex, particularly L2/3. In addition to differences in long-range targets, IT and PT neurons also have distinct local wiring schemes. While PT neurons primarily innervate other PT neurons, IT cells innervate both other IT and PT (Brown and Hestrin, 2009; Kiritani et al., 2012; Lefort et al., 2009), suggesting a unidirectional flow of information from IT to PT. Local inhibitory influence also appears stronger in IT than PT cells. Electrical stimulation of white matter tracts in rat brain slices led to clear excitatory postsynaptic potential (EPSP)-inhibitory postsynaptic potential (IPSP) sequences in RS cells (Chagnac-Amitai et al., 1990). However, in IB cells, stimulation induced an EPSP in the absence of an IPSP, suggesting weaker feedforward inhibition of PT than IT cells. Nevertheless, IT and PT cell dendrites span the entire length of the cortical column,

suggesting that both are equally poised to integrate information arriving to any given layer. Still, the apical dendritic arbors of PT cells ramify more extensively than that of IT (Hattox and Nelson, 2007; Larkman, 1991), suggesting that input to L1 could be differentially processed by each of these cell types.

The classical view of inputs distributions to cortical layers is that feedforward projections target L4, while feedback projections target L1 and L6 (Kaas et al., 1977, Rockland and Pandya, 1979, Tigges et al., 1977, Markov et al., 2014). However, these assumptions are based nearly exclusively on anatomical evidence of axon fiber density, and thus do not explicitly represent the true distribution of functional synapses. One way to address this discrepancy is to use subcellular channelrhodopsin-2-assisted circuit mapping (sCRACM), an activity-based method for assessing the location of synapses to a given neuron (Petreanu et al., 2009, 2007). sCRACM involves inducing channelrhodopsin expression in a defined axon population and recording whole-cell synaptic currents from a putative downstream neuron while optically dot-stimulating across the cortical slice. The resulting grid map of evoked synaptic currents provides a rough estimate of the location of functional synapses from the defined afferent population. Using sCRACM, Lafourcade et al. mapped inputs to L5 neurons in the RSC, an association area highly interconnected with PPC, from visual cortex, motor cortex, and thalamus. Comparing axon distribution and sCRACM maps, authors found that fiber density in RSC L1, particularly feedforward inputs from visual and motor areas, overestimates functional synapses from these pathways in that region (Lafourcade et al., 2022), likely due to increased fluorescent signal from fibers of passage. Furthermore, recent data from a different group performed a systematic comparison of feedforward and feedback synaptic input locations in the mouse secondary visual (V2) cortex (Galloni et al., 2022). Here, authors demonstrate also that while anatomical maps

suggest that ACC feedback to V2 primarily targets L1 dendrites, functional synapses on L5 cells are primarily in middle to deep layers (Galloni et al., 2022). Conversely, feedforward projections from V1 appear to target L4 based on fiber distribution, however functional synapses are primarily present in L1 and superficial L2 (Galloni et al., 2022). Together, these recent studies indicate that the classical view of feedforward input targeting L4, and feedback inputs targeting L1 and L6, may be incorrect. This could be due to the fact that canonical laminar projection density maps were primarily based on data from sensory cortical regions (Rockland and Pandya, 1979; Tigges et al., 1977), particularly feedforward thalamocortical projections to visual regions. However, data in higher-order sensory areas such as V2 (Galloni et al., 2022) and association areas including RSC (Lafourcade et al., 2022) and PPC (described in Chapter 2) suggest that feedforward cortico-cortico connectivity patterns differ from canonical targets of thalamocortical projections ("Projection :: Allen Brain Atlas: Mouse Connectivity," n.d.).

Integration of feedforward and feedback inputs will also be highly sensitive to intrinsic electrophysiological characteristics of L5 cells. Given the dramatic differences in firing pattern, IT (regular spiking) and PT (burst firing) cells are also presumed to have unique ion channel compositions. Burst firing is driven by a combination of slow-inactivating ionic mechanisms including T-type voltage gated calcium (T-VGCC) (Huguenard and Prince, 1992; Wong and Prince, 1978) and persistent sodium currents (Azouz et al., 1996; Brumberg et al., 2000; Su et al., 2001), which generate a slow (10's of milliseconds) depolarizing envelope triggered by action potential firing on top of which subsequent sodium spikes ride. A second mechanism involving a reverberatory interaction of back-propagating sodium spikes triggering forward-propagating dendritic calcium spikes also appears to contribute to burst firing (Lemon and Turner, 2000; Mainen and Sejnowski, 1996; Williams and Stuart, 1999). Interplay between somatic and

dendritic action potentials have also been implicated in detecting coincident synaptic input arriving in different cortical layers (Larkum et al., 1999). Synaptic interactions are highly sensitive to intrinsic conductances, particularly those involved in generating dendritic nonlinearities. Thus, based on their intrinsic electrophysiological dissimilarities alone, it is reasonable to expect that IT and PT differentially integrate synaptic input.

Perhaps unsurprisingly, IT and PT neurons are also known to have unique roles in the characteristic processing of information in cortical regions. In V1, IT neurons were shown to have higher detection thresholds and sharper orientation tuning than PT neurons (Lur et al., 2016). In primary motor cortex (M1), IT neurons were found to encode the amplitude, while PT neurons encoded direction of movements (Park et al., 2022). Selective inactivation of IT and PT neurons have also revealed distinct roles in behavior. Optogenetic inhibition of PT, but not IT, neurons in V1 impaired performance on a visually cued eyeblink conditioning task in mice (Tang and Higley, 2020). In the ACC, inhibition of specifically PT neurons enhanced rewarding properties, while inhibition of IT neurons suppressed the aversive properties of cocaine (Garcia et al., 2021). Complementing evidence of distinct behavioral roles for IT and PT cells, Takahashi et al. recorded *in vivo* calcium dynamics in apical dendrites of labelled L5 cells in primary somatosensory cortex. They demonstrate that when animals receive passive whisker stimulation, responsivity of IT and PT dendrites were equal (Takahashi et al., 2020). However, when whisker stimulation was an important signal for receiving reward, PT dendrites were significantly more responsive than IT (Takahashi et al., 2020). In total, the extensive differences in innervation patterns, electrophysiological profiles, behavioral roles, and early *in vivo* evidence of differential dendritic signaling in IT and PT neurons suggest that L5 cell types differentially integrate feedforward and feedback information streams.

Manipulating activity of distinct neural pathways

Our understanding of feedforward-feedback integration has been hampered by a lack of suitable methods for simultaneous manipulation of more than one neural pathway. For many decades, electrical stimulation has been the standard method for experimental and therapeutic activation of neurons. Electrical stimulation produces robust physiological responses (Borchers et al., 2012; Ranck, 1975) and is highly versatile, with applications ranging from large-scale activation of brain areas, from deep brain stimulation in treatment of Parkinson's (Lachenmayer et al., 2021), to the relatively localized activation of neural processes in cochlear implants (Zeng et al., 2008). While clinically successful, radial current spread guarantees that intermingled cells, terminating axons, and axons of passage have equal likelihood of excitation. Thus, the precise source of stimulation effects often remains unclear. In experimental settings, specialized preparations have allowed limited use of electrical stimulation for studying identified synaptic pathways, for example in thalamocortical (Agmon and Connors, 1991; Cruikshank et al., 2002) and hippocampal (Takahashi and Magee, 2009) circuits. In fact, taking advantage of the relatively structured input pathways of the hippocampus, Takahashi and Magee showed that simultaneous electrical stimulation of perforant path and Schaffer collateral input pathways were necessary to trigger dendritic spikes in CA1 neurons. Nevertheless, in most cortical applications, experimenters have limited pathway specificity if relying on electrical stimulation alone.

An attractive alternative to electrical stimulation is the use of optogenetic actuators to manipulate activity in brain circuits. A key benefit of optogenetic approaches is the namesake requirement to genetically express protein actuators or reporters, conferring light-sensitivity to select groups of experimenter-defined cells. As non-opsin-expressing cells remain insensitive to

light, optogenetic tools allows precise cell- and pathway-specific activation in otherwise spatially overlapping neural circuits. Optogenetic actuators include light-activated ion channels, ion pumps, and G protein-coupled receptors (Emiliani et al., 2022; Rost et al., 2017). Perhaps the most widely used actuators for circuit manipulation are channelrhodopsins. Channelrhodopsins are transmembrane ion channel proteins which incorporate retinal, the light-sensing molecule. Photon absorpotion induces an isomerization reaction in retinal from an all-*trans* to a 15-*cis* conformation, which in turn induces a reorganization of surrounding amino acid residues which opens an ion-selective pore (Ardevol and Hummer, 2018; Becker-Baldus et al., 2015; Xin et al., 2023). The net charge of pore residues then determines the ion species the specific channelrhodopsin protein passes (Berndt et al., 2016), while the color-sensitivity of each opsin is derived from the unique protein structure (Kishi et al., 2022; Prigge et al., 2012).

From the early days of optogenetics there was interest in combining multiple optogenetic tools with distinct wavelength sensitivity to independently control distinct neuron populations. Successfully applied, multicolor optogenetics would permit co-manipulation of feedforward and feedback pathways, allowing detailed study of their synaptic interactions with millisecond precision. Nonetheless, cross-activation of opsins with broad wavelength sensitivity remains a major concern. Extensive efforts have been taken to limit optical crosstalk (Anisimova et al., 2023; Bauer et al., 2021; Birdsong et al., 2019; Hooks et al., 2015; Joffe et al., 2022; Klapoetke et al., 2014; Prasad et al., 2020; Rindner et al., 2022; Shelton et al., 2022; Xia et al., 2020). Many groups have engineered new channelrhodopsin variants with more narrow activation spectra, covering a wider range of peak excitation wavelengths. In applied settings, experimenters have also adopted several optical approaches for limiting cross-activation. Unquestionably, the problem of crosstalk is ongoing.

Discovery roadmap

In the following 3 chapters, I optimize and employ optical approaches to study synaptic mechanisms of feedforward-feedback integration in the posterior parietal cortex (PPC). I begin this dissertation by describing advancements I make to increase the applicability of dual-color optogenetics for everyday users. I make procedural improvements which limit crosstalk, facilitating the adoption of a powerful multi-color optogenetic approach for other labs. I then use this technique to reveal key features of feedforward-feedback synaptic integration, including the importance of input timing, ionic conductances, and local microcircuitry for successful interaction between these critical information pathways. My experiments also reveal a novel role for layer 5 cell types in integrating feedforward and feedback inputs. Finally, I dive into the contribution of feedforward-feedback integration and projection-specific neuron populations to the generation of persistent firing, one of the defining characteristics of working memory in the PPC.

CHAPTER 1

Multi-color optogenetic approaches for studying complex neural circuits

1.1 Introduction

Multicolor optogenetic approaches are enormously valuable for studying the function of complex neural circuits. Optogenetic constructs with distinct wavelength sensitivity can be combined in actuator pairs, sensor pairs, or an actuator and sensor together in independent pathways, relying on spectral separation to bypass limitations imposed by spatial overlap of the tools. However, most current red-shifted optogenetic constructs exhibit sensitivity to blue light, leading to cross-activation concerns regardless of the precise tool combination used. I focus here exclusively on excitatory actuators, in particular channelrhodopsins. The earliest described channelrhodopsins were channelrhodopsin-1 (ChR1) (Nagel et al., 2002) and channelrhodopsin-2 (ChR2) (Nagel et al., 2003), discovered in the algal species *C. reinhardtii* (Figure 3A). ChR2 quickly became the protein backbone of many engineering efforts to increase speed (Gunaydin et al., 2010; Lin et al., 2009) and photocurrent amplitude (Berndt et al., 2011; Nagel et al., 2005), leading to the optimization of the protein for mammalian expression (Boyden et al., 2005). The excitation peak of wild-type ChR2 is at 470 nm (Nagel et al., 2003). Similarly, activation spectra for many popular mutant variants – ChR2(H134R) (Nagel et al., 2005), ChEF/ChIEF (Lin et al., 2009), ChETA (Gunaydin et al., 2010), ChR2(E123T/T159C) (Berndt et al., 2011) – as well as newly identified channelrhodopsins such as sdChR (Hochbaum et al., 2014) and Chronos (Klapoetke et al., 2014), peak in the 460-500 nm range (Figure 3A). Notably, these blue-light-activated opsins (referred to as “blue opsin(s)” going forward) also exhibit minimal sensitivity to wavelengths

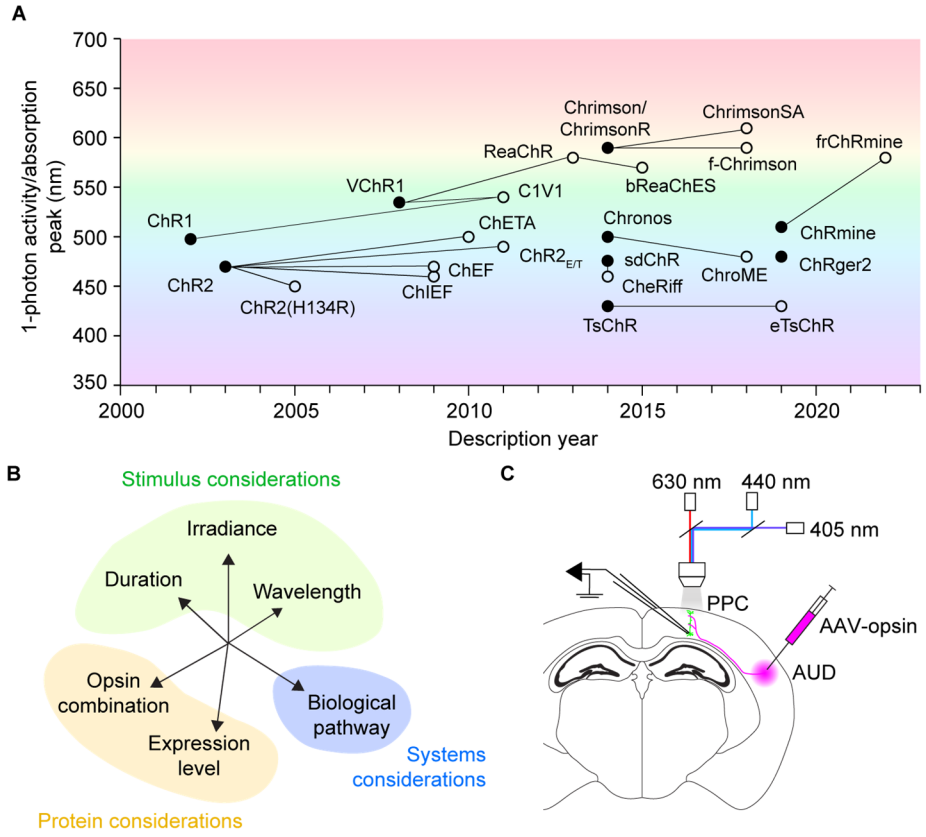

Figure 3. History, concerns, and testing of multicolor optogenetics. (**A**) Discovery history of commonly used channelrhodopsins for neural excitation. Filled circles designate novel opsins discovered by screening or created with rational design. Empty circles indicate mutant opsin variants, with connecting lines to their protein backbones. The mutant variant ChrimsonR overlaps with the native opsin Chrimson. Figure background color illustrates the wavelength of 1-photon activity/absorption peaks. (**B**) A representation of the multidimensional factors affecting opsin crosstalk. Each should be considered when designing any multicolor optogenetic experiment. (**C**) Schematic of experimental testing for crosstalk between excitatory optogenetic actuators for use in acute slice synapse activation applications. PPC: posterior parietal cortex; AUD: auditory cortex; AAV-opsin: Adeno-associated virus carrying opsin construct, either ChR2(H134R), Chronos, or ChrimsonR.

above 550 nm. Thus, an ideal red-shifted actuator for dual-color applications will be strongly activated by wavelengths longer than 550 nm, and insensitive to those under 500 nm.

VChR1, discovered in the algae *V. carteri*, was the first-reported opsin red-shifted over 50 nm from ChR2, with an excitation peak at 530 nm (Zhang et al., 2008) (Figure 3A). However, VChR1 has considerable blue-light sensitivity, which prevented its immediate use in dual-color applications. Perhaps the first widely adopted red opsin was the fusion protein C1V1 (Yizhar et al., 2011), a portmanteau of its component opsins ChR1 and VChR1. While the C1V1 peak absorption was hardly red-shifted compared to VChR1, it had appreciably less sensitivity to wavelengths under 500 nm (Yizhar et al., 2011). Still, C1V1 retains ~40% absorbance of 470 nm

light commonly used for activating blue optogenetic tools (Yizhar et al., 2011). The search for other red-shifted channelrhodopsins has yielded many protein alternatives, including ReaChR (Lin et al., 2013), Chrimson and ChrimsonR (Klapoetke et al., 2014), ChrimsonSA (Oda et al., 2018), ChRmine (Marshel et al., 2019), and frChRmine (Kishi et al., 2022). Nonetheless, all currently known red-shifted actuators (referred to as "red opsin(s)" going forward) exhibit non-negligible blue-light sensitivity, which can lead to possible cross-activation during blue stimulation periods if not properly controlled for.

Two strategies exist to minimize crosstalk, which have been applied to opsin combinations including Chronos/ChrimsonR (Bauer et al., 2021; Christoffel et al., 2021; Klapoetke et al., 2014), CheRiff/ChrimsonR (Anisimova et al., 2023), ChR2/ReaChR (Hooks et al., 2015), and ChR2(H134R)/ChrimsonR (Birdsong et al., 2019; Chiu et al., 2018; Joffe et al., 2022; Prasad et al., 2020; Rindner et al., 2022; Xia et al., 2020). Indeed, the precise strategy used will depend on experimental context. The first, introduced by Hooks et al., is often used to test pathway convergence (Bauer et al., 2021; Hooks et al., 2015; Prasad et al., 2020; Shelton et al., 2022). This approach involves utilizing a long, 50-250 ms, red light stimulus to forcibly inactivate the red opsin expressing neuron population before immediately stimulating the blue opsin. As the blue stimulus is applied while axons expressing the red opsin remain unresponsive, any postsynaptic response can be solely attributed to activation of blue opsin expressing cells. However, this method is not feasible in contexts where precise timing between blue and red channels is desired, for example in studies of spike-timing-dependent plasticity (Anisimova et al., 2023) or synaptic integration (Rindner et al., 2022; Xia et al., 2020). A second strategy is to limit stimulation parameters to ranges which do not cross-activate opsins (Anisimova et al., 2023; Birdsong et al., 2019; Joffe et al., 2022; Klapoetke et al., 2014; Rindner et al., 2022; Xia et al.,

2020). With this approach, blue stimulus irradiance, and less commonly duration, are first titrated in a separate experimental population where only the red opsin is expressed. The upper blue light exposure limit averting red opsin cross-activation is then used across all later experiments. This approach requires thorough testing (described in detail in *Results*), however, it allows maximum temporal control of independent neuron populations. A caveat of this approach is that population-derived blue light exposure limits may provide inadequate excitation in instances where blue opsin expression levels are low, resulting in cases where experiments must be discarded (Xia et al., 2020). This is particularly true when near-violet stimulation wavelengths, over 50 nm blue-shifted from the excitation peak of most blue opsins, are chosen (for example, 405 nm in Anisimova et al. 2023) in an effort to minimize cross-activation of red opsins. Thus, alternative strategies that maximize the dynamic range of crosstalk-free blue stimulus could improve the throughput of dual-color optogenetic experiments.

Here, I focus on a single synaptic pathway to test how the scope of experimental variables chosen by the investigator (Figure 3B) influences crosstalk risk, showcasing an example control experiment expanding on those done by others. I demonstrate an exhaustive test of crosstalk parameters, systematically varying the irradiance and duration of three different stimulus wavelengths – 405, 440, and 630 nm. In consideration of the range of opsins available, I furthermore test crosstalk between three commonly used actuators – ChR2(H134R), Chronos, and ChrimsonR. Lastly, I propose a "lookup table" approach leveraging red opsin responses on a cell-by-cell basis to maximize crosstalk-free blue excitation in multicolor optogenetic experiments.

1.2 Methods

Animals

Wild-type C57BL/6 mice of both sexes were used for all experiments. Mice were bred and maintained with *ad libitum* access to food and water on 12-hour light/dark cycles in University of California Irvine vivarium facilities. All mice were housed and used in accordance with the NIH guidelines on the care and use of laboratory animals.

Optogenetic construct expression

To express various optogenetic constructs, I transcranially injected either AAV2.9-hSyn-hChR2(H134R)-EYFP (titer: 3.6×10^12, Addgene: 26973-AAV9) (Zhang et al., 2010), AAV2.9-hSyn-ChrimsonR-tdTomato (titer: 2.9×10^12, Addgene: 59171-AAV9) (Klapoetke et al., 2014), or AAV2.9-Syn-Chronos-GFP.WPRE.bGH (titer: 1.6×10^12, originally obtained from the Penn Vector Core, now available from Addgene: 59170) (Klapoetke et al., 2014). Injections were targeted to auditory cortex (AUD, coordinates from bregma: anterior-posterior -2.8 mm, medial-lateral 4.1 mm, dorsal-ventral 0.8 mm) under isoflurane anesthesia between postnatal day (p) 28-40. Opsin constructs (150 nL) were injected at a rate of 25 nl / minute and allowed to express for (in days): ChR2(H134R), 32.2 ± 5; ChrimsonR, 29.9 ± 2.4; Chronos, 28.0 ± 7.2; mean ± standard deviation. Opsin expression was visually inspected at the beginning of all physiology experiments via band-pass illumination with a X-Cite mercury lamp (Excelitas Technologies). Slices were discarded if opsin-expressing fibers were not visually apparent.

Electrophysiology

Electrophysiology recordings were performed in 400μm thick coronal brain slices prepared on a vibrating microtome (smz7000-2, Campden Instruments) cut to contain the PPC (approximate coordinates from bregma: anterior-posterior: 2.0 mm, medial-lateral: 1.3-1.8 mm). After cutting, slices were maintained at 32°C for 15 minutes in solution comprised of (in mM): 110 choline, 25 $NaHCO_3$, 1.25 NaH_2PO_4, 3 KCl, 7 $MgCl_2$, 0.5 $CaCl_2$, 10 glucose, 11.6 sodium ascorbate, and 3.1 sodium pyruvate, bubbled with carbogen gas (95% O_2, 5% CO_2). Slices were then transferred to room-temperature ACSF comprised of (in mM): 126 NaCl, 25 $NaHCO_3$, 1.25 NaH_2PO_4, 3 KCl, 1 $MgCl_2$, 2 $CaCl_2$, and 10 glucose, and allowed to recover for a minimum of 20 minutes before recording.

Whole-cell recordings were performed in a submersion-type recording chamber mounted on an Olympus BX61-WI microscope. The extracellular bath solution consisted of oxygenated ACSF maintained at close to physiological temperature (32-34°C). Recording glass micropipettes were pulled on a P-1000 puller (Sutter Instruments) to have pipette resistances of 2-4 MΩ. Intracellular solution contained (in mM): 135 $KMeSO_3$, 10 HEPES, 1 EGTA, 4 $MgCl_2$, Na_2ATP, 0.4 NaGTP, and 10 sodium creatine phosphate, adjusted to pH 7.3 with KOH. Signals were amplified on a MultiClamp 700B amplifier (Molecular Devices) and digitized on National Instruments DAQ boards. Data were sampled at 10kHz, filtered at 4kHz, and acquired using WaveSurfer (HHMI Janelia Research Campus). Recordings were targeted to pyramidal cells in layer 5 (depth from pia: 0.5-0.65 mm), identified by their characteristic wide somatic morphology and non-fast-spiking firing patterns. Cells were held at ~-75mV, and series resistance constantly monitored for changes greater than 20% at which point cells were discarded. All analysis routines were custom written in Python 3.7.

Multi-color optogenetic stimulation

Multi-color excitation light was delivered through a 40x water immersion objective lens (Olympus). 405 nm, 440 nm, and 630 nm high speed LEDs (Sutter Instruments) were integrated into the light path using an optical beam combiner (Lambda OBC, Sutter Instruments) mounted directly to the microscope. I used a reverse mounting order such that higher power LEDs were mounted further from the OBC output. Stimulus properties (irradiance, duration) were controlled using WaveSurfer with a sampling rate of 100 kHz. All LED irradiances were tested using a stimulus duration of 100 μs and measured at the microscope objective with a PM100D power meter and S121C sensor (Thorlabs). All durations were tested with a stimulus irradiance of (in mW/cm^2): 21.06 (405 nm), 20.50 (440 nm), or 8.23 (630 nm).

Experimental design and statistical analysis

On occasion, stimulus parameters were sufficient to evoke action potentials in recorded neurons. In these instances, EPSP amplitudes were fixed at 25 mV. The PPC and AUD are reciprocally connected (Zingg et al., 2014), raising the risk of retrograde opsin expression in PPC contributing to evoked responses. However, opsin-expressing PPC cells were never observed, excluding this possibility. Non-zero postsynaptic responses were determined by comparing the maximum post-stimulus membrane potential to the peak-to-peak noise estimate taken pre-stimulus using paired t tests performed in Python 3.7. Stimulus parameters were tested through 10 repeated measurements in each cell. Each repeat was considered a single experimental replicate (n) when determining single cell response minimums. Responses from a given neuron

were averaged to form a single experimental replicate when determining population response minimums. No more than two cells were recorded from the same animal for a given condition.

1.3 Results

Multidimensional considerations in crosstalk testing

To demonstrate how stimulus wavelength, irradiance, duration, and opsin choice affect crosstalk in a system, I first chose a model synaptic pathway from the auditory cortex (AUD) to the posterior parietal cortex (PPC). AUD neurons synapse on pyramidal cells in PPC layer 5 and provide strong excitation when optogenetically stimulated (Rindner et al., 2022). I expressed ChR2(H134R), Chronos, or ChrimsonR in AUD using adeno-associated viral vectors (see *Methods*) and recorded light-evoked responses in layer 5 pyramidal cells of the PPC using whole-cell patch-clamp (Figure 3C). By varying stimulus irradiance or duration, I determined the dose-response relationship to excitation by 405 nm (blue/violet) (Figure 4A, B), 440 nm (blue) (Figure 4C, D), and 630 nm (red) (Figure 4E, F) LEDs. When expressed in AUD afferents, ChR2(H134R) and Chronos drove robust postsynaptic responses to 405 and 440 nm stimuli (Figure 4A–D). Stimulation of either opsin with 630 nm resulted in no detectable response (see *Methods*) across the range of irradiances or durations tested (Figure 4E, F, Table 1). In contrast, when afferents expressed ChrimsonR, light-evoked responses could be observed to stimulation with 405 nm (Figure 4B), 440 nm (Figure 4C, D) and 630 nm (Figure 4E, F, Table 1) wavelengths, as expected given the blue shoulder of the ChrimsonR activation spectra (Klapoetke et al., 2014). Notably, brief, low-irradiance stimulation at 405 nm and 440 nm averted ChrimsonR responses while eliciting EPSPs driven by ChR2(H134R)- and Chronos-expressing afferents (Figure 4A–D). This parameter range represents the ideal excitation window

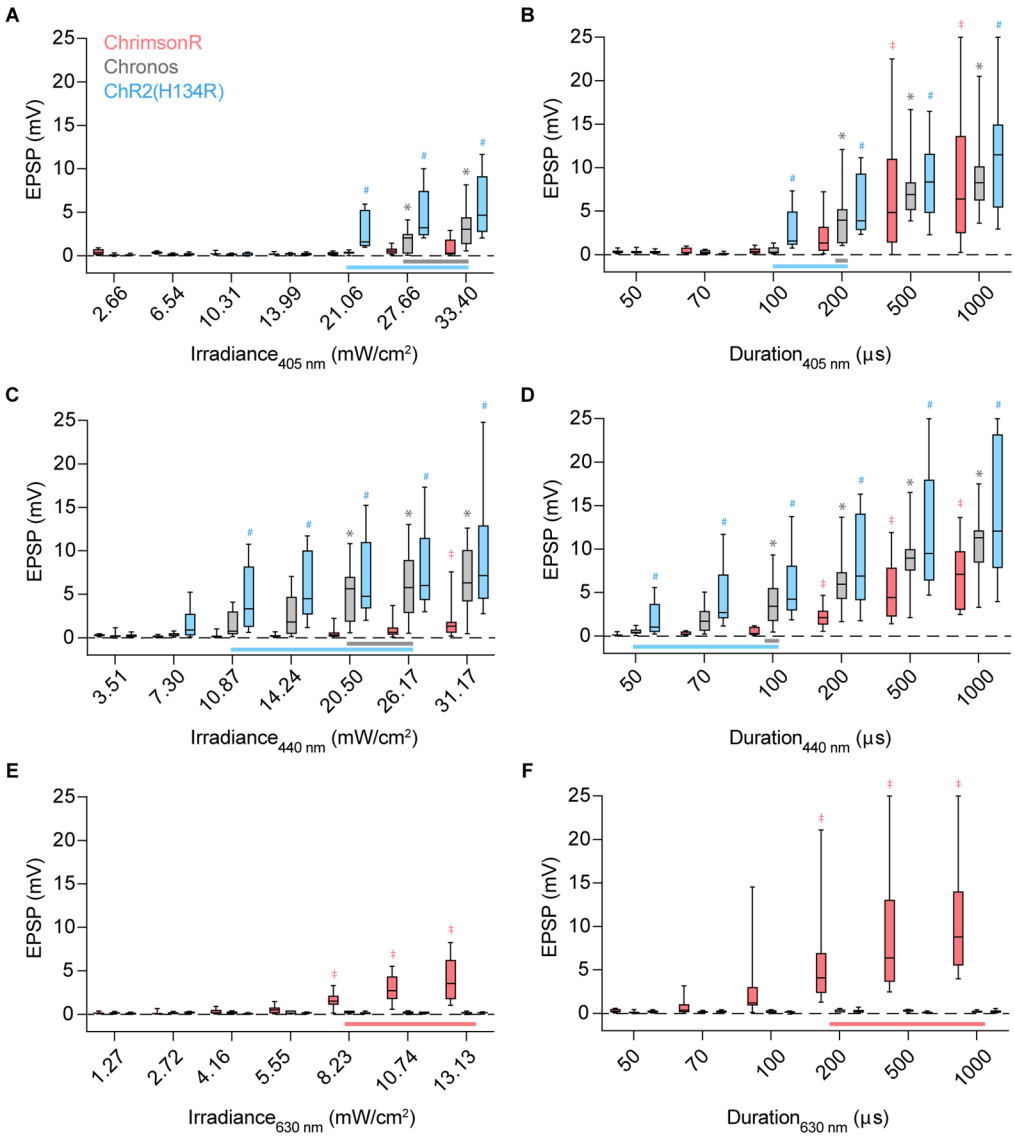

Figure 4. Stimulus irradiance, duration, wavelength, and opsin choice contribute to crosstalk risk. (**A**) Excitatory postsynaptic potential (EPSP) amplitudes when ChrimsonR (red), Chronos (grey), or ChR2(H134R) (blue) -expressing afferents are stimulated by a 100 µs pulse of 405 nm light with increasing irradiance. Vertical bars extend from the 25th to 75th percentiles, with the median represented by a horizontal line. Whiskers indicate minimum and maximum recorded values. Horizontal bars at bottom (in A–D) represent the stimulus parameter range which can be used to activate Chronos (grey) or ChR2(H134R) (blue) without cross-activating ChrimsonR. Symbols above the boxes indicate opsin (*: Chronos, #: ChR2(H134R), ‡ : ChrimsonR) and stimulus parameter combinations resulting in population-level non-zero responses ($p < 0.05$, t test, experimental replicates (n) listed in Table 1). (**B**) Response amplitudes when afferents are stimulated with a 21.06 mW/cm2 pulse of 405 nm light with increasing pulse durations. (**C**) Response amplitudes when afferents are stimulated with a 100 µs pulse of 440 nm light with increasing irradiance. (**D**) Response amplitudes when afferents are stimulated with a 20.50 mW/cm2 pulse of 440 nm light with increasing pulse durations. (**E**) Response amplitudes when afferents are stimulated with a 100 µs pulse of 630 nm light with increasing irradiance. (**F**) Response amplitudes when afferents are stimulated with a 8.23 mW/cm2 pulse of 630 nm light with increasing pulse durations. Red horizontal bar at bottom (in E–F) represents the stimulus parameter range which can be used to activate ChrimsonR without cross-activating Chronos and ChR2(H134R). ‡, *, # $p < 0.05$, t test.

(indicated by horizontal bars in Figure 4A-D) where ChrimsonR can be used in tandem with ChR2(H134R) (light blue) or Chronos (grey) without substantial risk of cross-activation on a population level. To determine the ideal blue opsin and wavelength combination for high

ChrimsonR
Chronos
ChR2(H134R)

405 nm Irradiance (mW/cm²)							405 nm Duration (µs)					
2.66	**6.54**	**10.31**	**13.99**	**21.06**	**27.66**	**30.4**	**50**	**70**	**100**	**200**	**500**	**1000**
(7)	(7)	(8)	(8)	(8)	(8)	(8)	(8)	(8)	(8)	(8)	(8)	(8)
0.996	0.999	>0.999	>0.999	0.999	0.997	0.747	>0.999	>0.999	0.999	0.158	**0.03**	**0.023**
(9)	(9)	(9)	(9)	(11)	(11)	(11)	(10)	(10)	(10)	(11)	(11)	(11)
>0.999	>0.999	>0.999	>0.999	>0.999	**0.031**	**0.002**	>0.999	>0.999	0.976	**0.003**	**<0.001**	**<0.001**
(8)	(8)	(8)	(8)	(8)	(8)	(8)	(10)	(10)	(10)	(10)	(10)	(10)
>0.999	>0.999	>0.999	0.999	**0.018**	**0.005**	**0.003**	>0.999	>0.999	**0.022**	**0.001**	**<0.001**	**<0.001**

440 nm Irradiance (mW/cm²)							440 nm Duration (µs)					
3.51	**7.3**	**10.87**	**14.24**	**20.5**	**26.17**	**31.17**	**50**	**70**	**100**	**200**	**500**	**1000**
(11)	(11)	(11)	(11)	(11)	(11)	(11)	(11)	(11)	(11)	(11)	(11)	(11)
>0.999	>0.999	>0.999	>0.999	0.887	0.209	**0.043**	>0.999	0.997	0.762	**<0.001**	**<0.001**	**<0.001**
(10)	(10)	(10)	(10)	(11)	(11)	(11)	(12)	(12)	(12)	(12)	(12)	(12)
>0.999	>0.999	0.058	0.054	**<0.001**	**<0.001**	**<0.001**	0.994	0.059	**0.002**	**<0.001**	**<0.001**	**<0.001**
(13)	(14)	(14)	(14)	(14)	(14)	(14)	(14)	(14)	(14)	(14)	(14)	(14)
>0.999	0.361	**<0.001**	**<0.001**	**<0.001**	**<0.001**	**<0.001**	**0.017**	**<0.001**	**<0.001**	**<0.001**	**<0.001**	**<0.001**

630 nm Irradiance (mW/cm²)							630 nm Duration (µs)					
1.27	**2.72**	**4.16**	**5.55**	**8.23**	**10.74**	**13.13**	**50**	**70**	**100**	**200**	**500**	**1000**
(11)	(11)	(11)	(11)	(12)	(12)	(12)	(11)	(11)	(11)	(11)	(11)	(11)
>0.999	>0.999	>0.999	0.98	**0.001**	**<0.001**	**<0.001**	>0.999	0.62	0.069	**0.005**	**<0.001**	**<0.001**
(7)	(7)	(7)	(7)	(7)	(7)	(7)	(7)	(7)	(7)	(7)	(8)	(8)
>0.999	>0.999	>0.999	>0.999	0.996	0.998	>0.999	0.999	>0.999	>0.999	0.999	>0.999	>0.999
(8)	(8)	(8)	(8)	(8)	(8)	(8)	(9)	(9)	(9)	(9)	(9)	(9)
>0.999	>0.999	>0.999	>0.999	0.992	>0.999	>0.999	>0.999	>0.999	0.991	0.998	>0.999	>0.999

Table 1. Experimental replicates and statistical test results. Experimental replicates (n) (top) and paired t test p values (bottom) of the recorded postsynaptic response to opsin excitation by indicated stimulus parameters. Colored rows represent replicates of (from top to bottom): ChrimsonR (red), Chronos (grey), ChR2(H134R) (light blue) stimulation. Bolded p values indicate $p < 0.05$.

dynamic range, crosstalk-free use with ChrimsonR, I next collapsed across irradiance and duration and compared peak ChR2(H134R) and Chronos responses at the maximum 405 and 440 nm radiant exposure level averting ChrimsonR responses (405 nm: 42.12 mJ/m^2; 440 nm: 26.17 mJ/m^2). Largest crosstalk-free blue opsin evoked EPSPs were obtained when ChR2(H134R)-expressing afferents were stimulated at 440 nm (ChR2(H134R): 11.14 mV at 405 nm, 17.31 mV at 440 nm; Chronos: 12.09 mV at 405 nm, 13.05 mV at 440 nm). These results suggest that, within the tested blue opsin and wavelength combinations, ChR2(H134R) excited at 440 nm allowed for the highest dynamic range activation of the AUD to PPC synaptic pathway.

Experiment-to-experiment maximization of crosstalk-free blue excitation

By definition, a population-derived maximum usable blue light exposure underestimates the true crosstalk-free exposure limit in a majority of experiments. To maximize crosstalk-free blue light stimulus, I next asked whether the upper limit of blue radiant exposure could be determined on an experiment-to-experiment basis, accounting for variable red opsin expression levels. I hypothesized that in dual-color experiments, red light responses could be used to estimate red opsin expression levels and predict sensitivity to blue light induced cross-activation. Indeed, within-cell comparison of EPSPs evoked by ChrimsonR-expressing afferents suggested that the maximum usable 440 nm radiant exposure level that averts cross-activation, increases linearly with the minimum 630 nm exposure necessary to evoke a response (Pearson r = 0.715, p = 0.046, n = 8; Figure 5A). I therefore propose that this red opsin "lookup table" (Figure 5A) can be pre-established in red opsin-only expressing preparations and later referenced in dual-color experiments to determine an experiment-specific maximum blue radiant exposure for crosstalk-

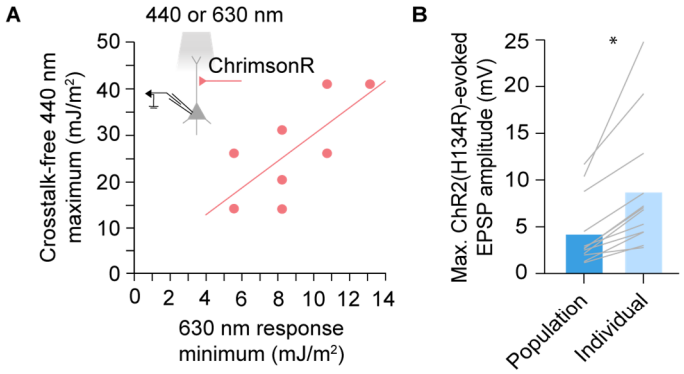

Figure 5. A red opsin "lookup table" for maximizing blue stimulus dynamic range. (**A**) Comparison of the minimum 630 nm radiant exposure necessary to elicit a detectable ChrimsonR postsynaptic response and maximum 440 nm radiant exposure averting a cross-activated excitatory postsynaptic potential (EPSP). Dots represent individual cells. Solid line represents the linear regression. Pearson r = 0.715, n = 8, p = 0.046. (**B**) Maximum evoked EPSP amplitudes when afferents expressing ChR2(H134R) are stimulated at population-derived or individually-derived blue radiant exposure limits. Grey lines represent individual cells. * p < 0.05, n = 12, paired t test.

free excitation. To quantify the improvement in blue opsin dynamic range using the lookup table approach, I compared ChR2(H134R)-evoked responses at the population-derived maximum usable 440 nm radiant exposure level (4.40 ± 1.07 mV, mean ± SEM) to peak responses with blue light exposure calibrated for individual experiments (8.88 ± 1.97 mV) (Figure 5B). I found that use of this lookup table allows an up to two-fold increase in the blue opsin response dynamic range ($p = 0.001$, $n = 12$, paired t test).

1.4 Discussion

The expansion of the optogenetic toolkit brings exciting new opportunities in neuroscience. With high-performance, spectrally shifted actuators becoming widely available, many groups have begun to newly implement multicolor optogenetic strategies, for example to stimulate converging synaptic pathways (Anisimova et al., 2023; Bauer et al., 2021; Birdsong et al., 2019; Hooks et al., 2015; Joffe et al., 2022; Rindner et al., 2022), activate intermingled cell types (Yizhar et al., 2011), or bidirectionally control neuronal populations (Atallah et al., 2012; Christoffel et al., 2021; Han and Boyden, 2007; Kampasi et al., 2016; Li et al., 2022; Vierock et al., 2021; Zhang et al., 2007). Here, I focus on synapse activation to consider how multiple experimenter-controlled variables (Figure 3B) combine to affect crosstalk. I furthermore introduce a red opsin "lookup table" approach for calibrating maximum blue light exposures on an experiment-to-experiment basis.

Indeed, stimulus irradiance and duration are often considered for their impact on crosstalk. However, my data indicates that cross-activation is a highly multidimensional issue, determined by interactions between stimulus irradiance, duration, wavelength, and additionally opsin choice. Ideally, each dimension should be properly tested when designing a dual-color

optogenetic experiment. This is important as theoretical advantages for dual-color optogenetics, particularly those measured directly in opsin-expressing cells, may not translate to similar advantages in a given biological system. For example, Chronos has large photocurrents and faster kinetics than ChR2(H134R) (Klapoetke et al., 2014). However, postsynaptic responses to ChR2(H134R) activation were detected at lower irradiances (Figure 4A, C) and durations (Figure 4B, D) than Chronos in the AUD to PPC synaptic pathway (although, note the 440 nm stimulus used here is ~50 nm blue-shifted from the excitation peak of Chronos). Furthermore, 440 nm stimulation consistently required lower irradiances and durations (at comparable irradiances: 405 nm, 21.06 mJ/m^2; 440 nm, 20.50 mJ/m^2) than 405 nm to elicit detectable responses, from both ChR2(H134R)- and Chronos-expressing fibers (Figure 4A–D). This resulted in a narrowing of the 405 nm ideal excitation window. Thus, using near-violet stimulation to avoid red opsin activation may paradoxically promote crosstalk, as the lower sensitivity of currently available blue opsins to these wavelengths necessitates use of higher radiant exposure level stimuli. These data suggest that while favorable opsin or stimulus properties may offer theoretical advantages in dual-color applications, in-house testing is necessary to select the ideal opsin combination for any particular use case.

The ability to elicit large, crosstalk-free opsin responses is critical for experimenters. Predictably, raising stimulus irradiance or duration will increase photon exposure and thus also response magnitude (given that certain biological factors, like number of synapses, do not saturate). One limiting factor can therefore be the experimental hardware, as irradiance will be limited by the power output of the stimulus light source. In our setup, this was most noticeable in my exploration of 630 nm responses, where a comparatively weak LED was used. In contrast, stimulus duration can be increased without constraint, its impact on membrane responses limited

only by the charge integration kinetics of the cell and the relatively slow process of opsin desensitization. In practice, stimulus duration may therefore offer the greatest opportunity to increase response amplitudes, given that cross-activation radiant exposure thresholds are not exceeded. Blue opsins are largely insensitive to red light (Figure 4E, F). Thus, red opsin responses can be enhanced by simply increasing stimulus radiant exposure levels, with upper light limits capped by hardware rather than crosstalk risks (however, note that cross-activation by blue stimuli may be possible by radiant exposure levels higher than tested here). In contrast, red opsins are sensitive to blue wavelengths (Figure 4A–C) (Kishi et al., 2022; Klapoetke et al., 2014; Lin et al., 2013; Marshel et al., 2019; Oda et al., 2018; Yizhar et al., 2011). The need to restrict blue radiant exposure levels below the red opsin's activation threshold can therefore limit an experimenter's potential to elicit large blue opsin responses. Here, I propose a lookup table approach for determining the maximum crosstalk-free blue radiant exposure using a functional assessment of red opsin expression levels, thereby maximizing the dynamic range available in each individual experiment (Figure 5A). In my hands, this approach increased blue light responses up to two-fold (Figure 5B). To ensure applicability to future experiments, the lookup table should encompass a large range of expression levels in each pathway or cell population. While light-evoked responses often scale with the observed brightness of the fluorescent tag carried by the opsin, this relationship can be construct specific and, in some cases, fluorescence signal from the tag may not ensure the presence of an evoked response (Klapoetke et al., 2014). I therefore propose that directly measured opsin responses are a more reliable predictors of crosstalk thresholds when constructing this lookup table.

In synapse activation experiments, crosstalk can be measured in opsin-expressing cells or downstream in postsynaptic neurons. I agree with previous studies (Birdsong et al., 2019; Joffe

et al., 2022; Xia et al., 2020) that downstream measurements better capture the functional implication of cross-activation. Nonetheless, it is likely that ChrimsonR photocurrents were activated at lower blue light intensities and durations than discernible from postsynaptic responses alone. However, this stimulus may either not activate enough ChrimsonR to trigger action potential firing in the afferents or engage enough synapses to produce a detectable response in the recorded postsynaptic neuron. Additionally, while the lookup table approach can improve blue opsin response ranges, it may overestimate crosstalk-free light levels for adjacent cells more strongly innervated by opsin expressing afferents. It is important to remember that crosstalk is subject to filtering by the biological system studied. In extreme cases, indirect measures including behavioral (Schild and Glauser, 2015) or paired-pulse response characteristics (Christoffel et al., 2021) can also been used as evidence against appreciable crosstalk, although opsin cross-activation almost certainly occurred. It is the experimenter's responsibility to consider subthreshold effects of such cross-activation and determine their potentially confounding influence on the process studied. As in any experiment, there is no substitute for high-quality controls for ensuring the validity of results. Whenever possible, swapping opsins between cell populations is one such necessary control.

Cross-activation concerns are not specific to excitatory actuator pairs. Other optogenetic tool combinations are equally subject to crosstalk, including excitatory with inhibitory actuators (Atallah et al., 2012; Christoffel et al., 2021; Han and Boyden, 2007; Kampasi et al., 2016; Li et al., 2022; Vierock et al., 2021; Zhang et al., 2007), actuators with sensors (Carrillo-Reid et al., 2016; Lim et al., 2012; Packer et al., 2015; Rickgauer et al., 2014; Seidenthal et al., 2023; Yang et al., 2018), and sensors with sensors (Akerboom et al., 2013; Han et al., 2019; Li et al., 2013; Zhao et al., 2011). Multicolor sensitivity is also a core feature of bistable step-function opsins

(Berndt et al., 2009; Gong et al., 2020; Wietek et al., 2017; Yizhar et al., 2011), where an additional wavelength-to-response relationship must be carefully considered. Efforts to produce optogenetic tools with decreased blue light sensitivity and further red-shifted peak activation are ongoing (Kishi et al., 2022; Mermet-Joret et al., 2021). Parallel modifications to blue-activated tools may also decrease crosstalk risk. High-photocurrent, high-sensitivity blue opsins, such as ChRger2, could further reduce the necessary blue radiant exposure to stimulate neurons (Bedbrook et al., 2019), thus reducing crosstalk risk. Opsins with fast activation kinetics, such as Chronos and ChroME (Mardinly et al., 2018), have also been successfully applied in multicolor experiments. A third avenue that saw limited success was to further blue-shift action spectra. TsChR, a channelrhodopsin discovered in *T. striata*, has an excitation peak at 430 nm and is the most blue-shifted channelrhodopsin known to date (Klapoetke et al., 2014). Membrane trafficking of TsChR was further optimized to generate eTsChR (Farhi et al., 2019). While promising, the efficacy of eTsChR in multicolor applications has yet to be verified. The continued spectral and kinetic expansion of the optogenetic toolkit, combined with experimental strategies for minimizing crosstalk, will ultimately broaden the adoption of dual-color approaches for studying brain function.

CHAPTER 2

Cell-type-specific integration of feedforward and feedback synaptic input in the posterior parietal cortex

2.1 Introduction

Integrating feedforward and feedback neuronal signals is a principal function of the neocortex. Cortical feedforward systems, originating in primary sensory areas, relay environmental signals to higher order brain structures. These higher order regions in turn send afferents to lower order cortices, forming feedback pathways that carry contextual information like task structure, goals, expectations, and memories. The convergence of feedforward and feedback streams is ubiquitous to most cortical areas and their interaction is fundamental to cognitive processes like attention (Ito et al., 1998; McMains and Kastner, 2011; Morishima et al., 2009; Olson et al., 2001), sensory scene analysis (Habtegiorgis et al., 2019; Snyder et al., 2012), and motor planning (Churchland and Shenoy, 2007; Habtegiorgis et al., 2019; Narayanan and Laubach, 2006). In sensory regions, feedforward-feedback interactions are thought to contribute to gain control (McAdams and Maunsell, 1999; Moran and Desimone, 1985; Treue and Trujillo, 1999; Zhang et al., 2014) and the tuning of neuronal receptive fields (Fritz et al., 2003; Li et al., 2004; Spitzer et al., 1988), thereby enabling context-dependent sensory processing. Similar interactions have been observed in the thalamus (O'Connor et al., 2002) and in association cortices (Ibos and Freedman, 2014; Toth and Assad, 2002). Despite this prevalence of feedforward-feedback integration in the neocortex, the synaptic mechanism of how these neuronal pathways interact remains elusive.

According to the canonical circuit model, feedforward projections target layer 4 of the cortex while feedback axons terminate in layers 1 and 6 (Kaas et al., 1977; Markov et al., 2014; Rockland and Pandya, 1979; Tigges et al., 1977). Dendritic trees of layer 5 pyramidal neurons vertically span most of the cortex, making them uniquely positioned to integrate contextual information with sensory input (Larkum et al., 1999; Larkum and Zhu, 2002; Llinás et al., 2002; Takahashi et al., 2020; Xu et al., 2012). However, principal cells in layer 5 are not comprised of a homogeneous population. Neuronal categories have been identified via genetic markers, morphology, and electrophysiological properties (Ascoli et al., 2008, p. 200; Groh et al., 2010; Kim et al., 2015; Oswald et al., 2013; Tasic et al., 2018). Recent work suggests that this diversity extends to patterns of connectivity, indicating the existence of independent, parallel cortical networks (Anderson et al., 2010; Brown and Hestrin, 2009; Dantzker and Callaway, 2000; Jiang et al., 2015; Morishima et al., 2017). In layer 5, multiple pyramidal cell types have been identified, broadly clustering into regular spiking neurons (RS), typically projecting to other cortical regions and the striatum, and intrinsic burst firing cells (IB) that project subcortically (Chagnac-Amitai et al., 1990; Connors et al., 1982; Dembrow et al., 2010; Gao and Zheng, 2004; Harris and Shepherd, 2015; Hattox and Nelson, 2007; Kasper et al., 1994; Larkman and Mason, 1990; Mason and Larkman, 1990; Morishima et al., 2011; Yang et al., 1996). This segregation of cell types appears to be conserved from mice to humans (Hodge et al., 2019). Previous work demonstrated that these physically interspersed excitatory neurons play distinct roles in encoding sensory stimuli and behavior (Glickfeld et al., 2013; Kwon et al., 2016; Lur et al., 2016; Tang and Higley, 2020; Yamashita and Petersen, 2016). The two cell types have also been shown to receive unequal excitation by layer 1 synaptic inputs (Cauller and Connors, 1994). Accordingly, one recent study found that behavioral context modulated dendritic signaling in IB, but not in RS

neurons (Takahashi et al., 2020). Detailed mapping of synaptic inputs revealed that IB cells in the visual cortex received a greater proportion of their input from the higher order retrosplenial and anterior cingulate cortices than RS neurons (Kim et al., 2015). These data suggest that layer 5 cell types may be differentially regulated by feedforward and feedback information. Nonetheless, whether IB and RS receive direct, monosynaptic innervation from both feedforward and feedback sources, and how these inputs may sum at the synaptic level has yet to be directly examined.

In this chapter, I explore the interaction of identified feedforward and feedback synaptic inputs in the posterior parietal cortex (PPC), an association area involved in multimodal integration, attention, working memory and decision making (Goard et al., 2016; Mohan et al., 2018; Musall et al., 2023; Olcese et al., 2013; Raposo et al., 2012; Zhang et al., 2016; Zingg et al., 2014). Using the dual color optogenetic strategy (Klapoetke et al., 2014) calibrated in detail in Chapter 1, I show that both IB and RS cells in layer 5 of the PPC receive direct, converging input from the anterior cingulate cortex (ACC) and sensory cortical regions including the auditory (AUD) and visual cortices (VIS). Both IB and RS neurons displayed nonlinear integration of these input pathways, however there were marked differences in the temporal dynamics of this interaction. These subthreshold integration characteristics translated to nonlinear action potential firing. Furthermore, using a combination of electrophysiology and computational modeling in a collaborative effort between myself and Dr. Archana Proddutur in Dr. Gyorgy Lur's lab, I found that distinct integration profiles arose from an interaction of multiple ionic mechanisms and cell-type-specific feedforward inhibition.

2.2 Methods

Animals

All experiments were performed in accordance with the NIH guidelines on the care and use of laboratory animals and approved by the Institutional Animal Care and Use Committee. All animals were group-housed in a quiet, uncrowded facility on a 12 h light/dark cycle, with *ad libitum* access to lab chow and water. Male and female C57BL/6J wild-type mice were used in the study. No differences were detected between sexes thus data were pooled.

Optogenetic construct expression

For independent control of distinct synaptic inputs to the PPC, I expressed the blue light-sensitive channelrhodopsin ChR2(H134R) alongside the red light-sensitive ChrimsonR (Klapoetke et al., 2014) in separate afferent populations. ChR2 and ChrimsonR were introduced via transcranial injection of adeno-associated virus (AAV) constructs AAV2.1-Syn-hChR2(H134R)-EYFP (titer: 2.1 x 10^12, Addgene: 26973-AAV1) or AAV2.9-Syn-hChR2(H134R)-EYFP (titer: 3.6 x 10^12, Addgene: 26973-AAV9) for ChR2, and AAV2.1-Syn-ChrimsonR-tdTomato (titer: 2.1 x 10^12, Addgene: 59171-AAV1) or AAV2.9-hSyn-ChrimsonR-tdTomato (titer: 2.9 x 10^12, Addgene: 59171-AAV9) for ChrimsonR. Opsin constructs were injected at volumes of 150nL into AUD, 150nL into VIS, 200 nL into ACC. Virus titers and volumes were kept unchanged throughout the experimental series. Mice were injected under isoflurane anesthesia at postnatal day 25-40 (P25 - P40). Injections were targeted to either the anterior cingulate cortex (ACC, coordinates from bregma: anterior-posterior +1.0 mm, medial-lateral 0.3 mm, dorsal-ventral 1.0 mm), auditory cortex (AUD, anterior-posterior -2.8 mm, medial-lateral 4.1 mm, dorsal-ventral 0.8 mm), or visual cortex (VIS, anterior-posterior

-3.5 mm, medial-lateral 2.1 mm, dorsal-ventral 0.5 mm). Opsins were allowed to express for a minimum of 14 - 30 days before physiology experiments. To confirm expression and check for potential retrograde or spillover labeling of PPC neurons, ChR2-EYFP and Chrimson-tdTomato positive afferents were visualized in acute PPC slices via band-pass illumination using an X-Cite mercury lamp (Excelitas Technologies). Slices with overall low expression, with a notable difference of expression between the two opsins, or with PPC neurons expressing either construct, were discarded.

Electrophysiology

For physiology recordings, 300 µm thick coronal brain slices containing the PPC were prepared on a vibrating microtome (smz7000–2, Campden Instruments) from P45 - P60 mice. Immediately after sectioning, slices were maintained at 32°C for 15 minutes in solution comprised of (in mM): 110 choline, 25 $NaHCO_3$, 1.25 NaH_2PO_4, 3 KCl, 7 $MgCl_2$, 0.5 $CaCl_2$, 10 glucose, 11.6 sodium ascorbate and 3.1 sodium pyruvate, and bubbled with 95% O_2 and 5% CO_2. Slices then were allowed to recover for at least 20 minutes in oxygenated room-temperature ACSF containing (in mM): 126 NaCl, 25 $NaHCO_3$, 10 Glucose, 3 KCl, 2 $CaCl_2$, 1.25 NaH_2PO_4, and 1 $MgSO_4$ prior to recording. All experiments were conducted close to physiological temperature (32-34 °C) in a submersion type recording chamber mounted on an Olympus BX61-WI microscope. The hippocampus was used as a histological landmark to identify PPC in coronal sections. Recordings were targeted to the mediolateral section of PPC between 1300-1800 µm from the midline to minimize influence of potential subregion-specific differences. This approach resulted in targeting the approximate coordinates of (in mm from the Bregma) AP: 2.0, ML: 1.3-1.8, DV: 0.5-0.65. Whole-cell patch-clamp recordings were obtained from layer 5

pyramidal cells (450-650 μm from the pial surface) identified with video-infrared / differential interference contrast microscopy. For current-clamp recordings, glass electrodes (2-4 MΩ) were filled with internal solution containing (in mM): 135 $KMeSO_3$, 10 HEPES, 1 EGTA, 4 $MgCl_2$, 4 Na_2ATP, 0.4 NaGTP, and 10 sodium creatine phosphate, and adjusted to pH 7.3 with KOH. To record AMPA and NMDA currents, K^+ was substituted for Cs^+ to improve space clamp. Series resistance was 9-16 MΩ. Recordings outside of this range, or if series resistance changed more than 20% over the course of the experiment, were discarded. Subthreshold integration experiments were performed in current clamp at a steady-state membrane potential held close to the estimated reversal potential for inhibitory currents (-75 mV). Suprathreshold experiments were performed with a pre-stimulus membrane potential of -60 mV. Voltage clamp measurements of AMPA receptor currents were conducted at -70 mV, NMDA currents were measured at +40 mV and inhibitory currents at 0 mV membrane potential. Signals were amplified using a MultiClamp 700B amplifier (Molecular Devices). Data were sampled at 10 kHz, filtered at 4 kHz, and digitized on National Instruments DAQ boards. WaveSurfer software written in Matlab (HHMI Janelia Research Campus) was used for data acquisition. Offline analysis was performed using custom routines in Python 3.7.

Dual-color optogenetic stimulation

In order to deliver dual-color excitation through the microscope objective, I introduced a 440 nm (blue) and a 630 nm (red) LED (Sutter Instruments) into the light path of the BX61 WII microscope via an optical beam combiner (Lambda OBC, Sutter Instruments). Stimulus duration and amplitude were controlled via the WaveSurfer stimulus library with a stimulus sampling rate of 100 kHz. To determine the LED power windows that avoid cross-excitation of the two opsins,

I transduced AUD with either ChR2 or Chrimson in separate animals (single opsin expression). Following at least two weeks of expression, I made whole cell recordings of layer 5 pyramidal neurons in acute PPC slices. I recorded evoked EPSPs in response to independently activating the 440nm and 630nm LEDs. I plotted ChR2 and Chrimson mediated postsynaptic responses to each wavelength against the corresponding LED power, measured post-hoc with a light meter (Thorlabs). These measurements outlined the excitation power window for the 440 nm LED that enables the separation of input pathways (as in Chapter 1).

To account for potential differences in expression levels in dual opsin containing mice (both ChR2 and Chrimson in the same preparation), LED power on both channels was adjusted to elicit ~4 mV EPSPs in subthreshold experiments or trigger action potentials on 40-50% of trials in suprathreshold experiments. LED powers were determined for each cell approximately 5 minutes after break in and kept constant for the duration of the experiment. Unimodal blue and red stimuli were sequentially interleaved with dual activation throughout the full length of each recording.

Cell type classification

PPC layer 5 pyramidal neurons were classified as either intrinsically bursting (IB) or regular spiking (RS) cells based on membrane potential responses to 500ms step current injections. I measured resting membrane potential, input resistance, sag potential, depolarizing envelope, initial burst, slow afterhyperpolarization (sAHP), and action potential (AP) half-width (Figure 7). Input resistance was determined from a -150 pA step. Sag was calculated as the voltage difference between peak and steady-state hyperpolarization and expressed as a percentage of peak response. Depolarizing envelope was quantified as the maximum difference between the

afterhyperpolarization potential of two spikes. Initial burst refers to the percentage of action potentials fired within 40 ms of the first spike. Cells that had a combination of low input resistance, high initial burst value, larger sag, and larger depolarizing envelope were classified as intrinsic bursting (IB). Cells with high input resistance, low initial burst value, lower sag, and smaller depolarizing envelope were deemed regular spiking (RS). While at the population level there is overlap between these measures, at the level of individual cells, the combination of these metrics separates IB and RS cells. Cell type assignment was performed during *post hoc* analyses, blind to experimental condition or results. In a subset of experiments (Figure 19), putative-IB and putative-RS cell-types were identified based on anatomical projection patterns. To do this, I utilized one of three methods. First, in wild type mice, I injected red (555 nm) Alexa Fluor-conjugated cholera toxin subunit B (CTB, ThermoFisher) into the dorsal Striatum (350 nl, AP: 0.85, ML: 1.5, DV: 2.0 in mm from Bregma) or into the Pons (500 nl, AP: -4.1, ML: 0.8, DV: 5.5 in mm from Bregma) prepared according to the description in (Conte et al., 2009). Second, in wild type mice, I transduced the dorsal Striatum or the Pons with AAVrg-hSyn-mCherry (titer: 2.0 x 10^12, volume: 500nl, Addgene: 114472-AAVrg). Third, in the Ai14 mouse line, I transduced the dorsal Striatum or the Pons with pENN.AAV.hSyn.Cre.WPRE.hGH (titer: 1.2 x 10^12, volume: 500nl, Addgene: 105553-AAVrg). The retrograde constructs were injected at volumes of 350nL into dStr, and 500nL into Pons. For all physiology experiments, only one cell type was labelled in each animal.

Testing monosynaptic inputs

To determine whether afferent inputs were monosynaptic, I utilized a combination of two methods. In a subset of experiments, I performed a pharmacological test following integration

measurements, using TTX (Tocris) and 4-Aminopyridine (4-AP, Tocris) (Petreanu et al., 2009). Inputs were considered monosynaptic if the EPSP could be recovered in 4-AP (100-500 μM) after 1 μM TTX application. After recovery, I applied a combination of AMPA- and NMDA receptor blockers – 2,3-Dioxo-6-nitro-1,2,3,4-tetrahydrobenzo[f]quinoxaline-7-fulfonamide (NBQX, 10 μM, Tocris) and 2-amino-5-phosphonopentanoic acid (AP5, 50 μM, Tocris), respectively – to confirm synaptic responses were indeed glutamatergic. The shortest EPSP latency, measured prior to TTX application, of inputs failing the TTX/4-AP test was 4.0 ms. Thus, I chose 4 ms as our latency cutoff which was then applied *post hoc* to all experiments. Recordings where inputs failed either the pharmacological or latency test were removed from further analyses.

Histology

Afferent fibers in the PPC were visualized via the EYFP and tdTomato fluorescent tags on the ChR2 and ChrimsonR constructs, respectively. For histology experiments, both projection neuron types were identified in the same animal, using Alexa Flour 555 in tandem with Alexa Flour 488 conjugated CTB, injected in pons and dStr, respectively. After 14-30 days of opsin expression, (7-10 days for CTB), mice were deeply anesthetized using isoflurane and transcardially perfused with 4% paraformaldehyde (PFA) in Sorenson's buffer. Brains were extracted and post-fixed in 4% PFA overnight. Coronal slices (50 mm) were prepared on a vibrating microtome (Compresstome, Precisionary Instruments). Slices were mounted on gelatin coated microscope slides and cover slips were affixed with Prolong Diamond (ThermoFisher). Neurons throughout the tissue were visualized via NeuroTrace 435/455 fluorescent Nissl staining (ThermoFisher). Some slices without NeuroTrace staining were instead mounted with Prolong

containing 4',6-diamidino-2-phenylindole (DAPI) (ThermoFisher). Samples were imaged either on a BZ-9000 fluorescence microscope (Keyence, Sumikawa Lab, UC Irvine) or a Zeiss LSM900 confocal microscope using a 20x air immersion objective and appropriate filter sets. Tiled images were assembled, and channels assigned faux color in the Zen software (Zeiss). Fluorescent intensities throughout the cortical column were quantified using the plot profile tool in ImageJ with a line width of 100 pixels. Intensities were normalized to peak fluorescence within each measurement. I used the integral of mean fluorescence to compare the relative density of ACC, AUD, and VIS afferents in superficial (0-150 μm), intermediate (150-400 μm), and deep (400-800 μm) cortical layers.

Drugs and salts

For pharmacological experiments, drug effects were recorded at 5-10 minutes after the addition of the compounds to the perfusion fluid. Agents were used at the following concentrations: mibefradil (Tocris): 20 μM, 2-amino-5-phosphonopentanoic acid (AP5, Tocris): 50 μM, tetrodotoxin (TTX, Tocris): 100 nM, picrotoxin (PTX, Tocris): 6 μM, NBQX (Tocris): 10 μM, 4-AP (Tocris): 100-500 μM. To specifically block postsynaptic $GABA_A$ receptors, I included picrotoxin in the pipette solution at 10 mM concentration (Inomata et al., 1988, Metherate and Ashe, 1993, Yazaki-Sugiyama et al., 2009). All other materials, including standard salts, were acquired from Sigma or Fisher Scientific.

Computational modeling of synaptic interactions

To test potential mechanisms of integration in layer 5 neurons, Dr. Archana Proddutur produced model in the NEURON simulation environment (Hines and Carnevale, 1997), that included a

soma and dendrites with a proximal and distal component. Each dendritic segment had a length of 150 µm and diameter of 1 µm with additional models testing 0.5 and 2 mm dendritic diameters. The somatic compartment had a length of 15 µm and diameter of 15 µm. Two morphologies were tested: a simple arrangement with one dendrite attached to the soma and a more complex morphology with two identical dendrites, both originating from the soma. Passive properties of the model cell include input resistance: 94.8 MΩ; axial resistance: 100 Ω·m; capacitance of each compartment: 1.5 µF/cm^2; leak channel conductance: 0.9 mS/cm^2 with a reversal potential of -70 mV. The resting membrane potential of the model cell was -68 mV. Ion channel conductances were distributed in the compartments as shown in Figure 12. Sodium and potassium channel conductances (gNa and gK) were uniformly distributed whereas low threshold T-type calcium channel conductance (gT-Ca) distribution was highest in the proximal dendritic segment in a 1 : 2 : 1 = soma : proximal : distal ratio (Zomorrodi et al., 2008). A calcium-dependent potassium channel conductance (gSK) was evenly distributed in all segments. A hyperpolarization-activated potassium conductance modeled after the HCN1 channel (gHCN1) was also included and distributed with concentration increasing towards the distal dendrite (Harnett et al., 2015; Stadler et al., 2014). To simulate frontal and sensory inputs, glutamatergic excitatory synapses were placed in the dendritic compartments as indicated in the figure schematics and were driven via NetCon objects. They included AMPA and NMDA receptor-mediated conductances and were modeled with exponential rise and decay kinetics using the Exp2Syn class, as adapted from (Egger et al., 2015). AMPA receptor current rise and decay time constants (τ) were 0.2 and 2 ms, respectively. NMDA receptor currents had a τ_{rise} = 4 ms, while the τ_{decay} parameter was varied from 30-70 ms in increments of 5ms (Schulz et al., 2018). To compare the performance of various model configurations in Figure 24, conductances

were adjusted to produce identical unimodal EPSP magnitudes across morphologies. Where described, an inhibitory $GABA_A$ receptor synapse was included on either the dendritic segment targeted by excitation or on the soma. $GABA_A$ receptor synapses had rise and decay kinetics of τ_{rise} = 0.5 ms and τ_{decay} = 20 ms, with conductance matching the conductance of the respective excitatory synapses (Egger et al., 2015). To represent the short-term depression of $GABA_A$ synaptic inputs, the maximal conductance of delayed inhibitory inputs was reduced in the model by 40%, mimicking values observed in my physiology experiments. The reversal potential of $GABA_A$ receptor synapses was set to -75 mV after our calculated chloride reversal potential. To mimic conditions of in vitro experiments, the model cell was clamped at -75 mV for the duration of synaptic integration simulations. Two individual VecStim Pointprocess objects were used to simulate frontal and sensory input synapses, which were activated either alone (unimodal), or together with a 0 ms or 50 ms delay (multimodal). Antagonistic drug effects were simulated by setting target conductances to 0 S (simulated TTX, gNA = 0 S; simulated mibefradil, gT-Ca = 0 S, gSK = 0 S; simulated AP5, gNMDAR = 0 S). Multimodal enhancement index (MEI) of each simulated integration events was calculated exactly as was for physiology experiments (see below). In some model configurations, high excitatory conductance drove the model to spike. In these cases, the MEI was calculated from the action potential threshold, using first derivative method (dV/dt) where membrane potential reached ~10mV/ms. Membrane potential traces of individual simulations were extraced and spike thresholds measured using dV/dt method in the Clampfit Software. While this calculation likely underestimated the true supralinearity produced by the synaptic integration, it was judged to be the most physiologically relevant readout.

Experimental design and statistical analysis

In all figures, I present all recorded data points, the data mean and 95% confidence intervals. Up to three cells were recorded per animal for each experiment. Responses recorded from the same cell type within an animal were then averaged and treated as a single experimental replicate (n) for all statistical comparisons unless specifically stated otherwise. Cell type assignment was performed blind to experimental condition (see *Cell type classification* above). Assessment of drug effects were performed within cells (pre and post drug conditions) using paired t-test. In this case, no more than two replicates were recorded from a single animal. Feedforward inhibition to L5 cells was calculated from evoked EPSPs as the voltage difference before and after $GABA_A$ blockade (PTX, 6 μM) at the time of peak in PTX. Means, confidence intervals and t-statistics were calculated in Python 3.7. Where applicable, multiple comparisons were accounted for using Sidak's correction. Temporal dynamics of synaptic interaction were analyzed by comparing the recorded multimodal response amplitude to the arithmetic sum of unimodal EPSPs at the corresponding delay using a one-sample t-test. Integration profiles across groups were compared using a mixed model two-way ANOVA in Prism 8 (GraphPad). Given that I found no effect of input order on subthreshold integration profiles, action potential firing data from each cell were pooled and averaged across input orders.

Quantification of multimodal interactions

To quantify the interaction of two distinct synaptic inputs, I calculated a Multimodal Enhancement Index (MEI) by dividing the recorded multimodal response by the arithmetic sum of unimodal responses. Subthreshold MEI was calculated using evoked EPSP amplitudes: $EPSP_{multimodal}$ / ($EPSP_{unimodal\text{-}1}$ + $EPSP_{unimodal\text{-}2}$), where the sum of unimodal responses was

determined by adding the voltage traces resulting from each unimodal stimulation. Suprathreshold MEI was calculated using the number of evoked action potentials (APs): $nAP_{multimodal}$ / ($nAP_{unimodal\text{-}1}$ + $nAP_{unimodal\text{-}2}$).

2.3 Results

Monosynaptic dual innervation of layer 5 PPC neurons by feedforward and feedback afferents

To understand how layer 5 pyramidal neurons in the PPC integrate feedforward inputs with feedback signals, I first set out to determine whether these information streams converge onto individual cells. I expressed the red-shifted channelrhodopsin variant Chrimson in the auditory cortex (AUD, feedforward) and the blue light sensitive ChR2(H134R) (hereinafter, "ChR2") in the anterior cingulate cortex (ACC, feedback) (Figure 6A). Opsin expressing long-range afferents from ACC and AUD were readily observed in the PPC (Figure 6B). I made whole-cell patch clamp recordings from layer 5 pyramidal neurons in acute PPC slices and used brief pulses of 630nm or 440nm light to activate AUD or ACC axons, respectively (Figure 6C). A caveat of this dual color optogenetic approach is the limited but appreciable sensitivity of

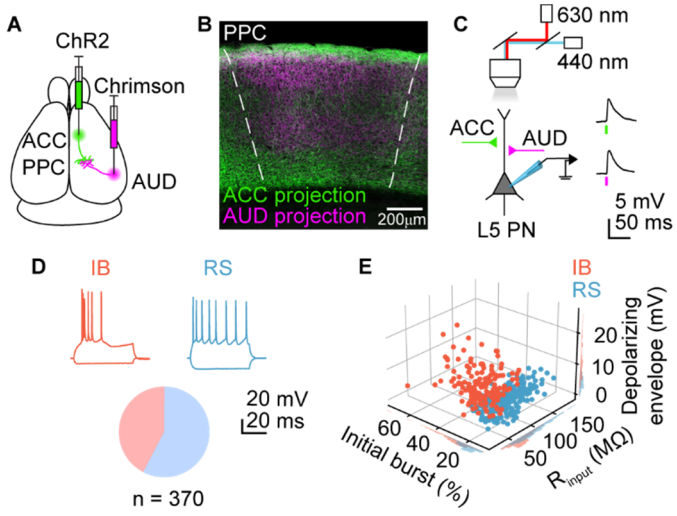

Figure 6. Dual-color optogenetic approach for selective activation of feedforward-feedback pathways to L5 cells. (**A**) Schematic illustrating the transduction of ACC and AUD with ChR2 and Chrimson constructs, respectively. (**B**) Example image of ACC and AUD afferents in the PPC. Scale bar, 200 µm. (**C**) Schematic of dual optogenetic experiments. Brief pulses of 630 nm or 440 nm light resulted in excitatory postsynaptic responses detected by whole cell patch clamp recording in acute PPC slices. (**D**) Representative firing patterns of IB and RS neurons. Pie chart displays the proportion of IB and RS cells in layer 5 of the PPC. (**E**) Intrinsic response metrics used to classify layer 5 pyramidal cells.

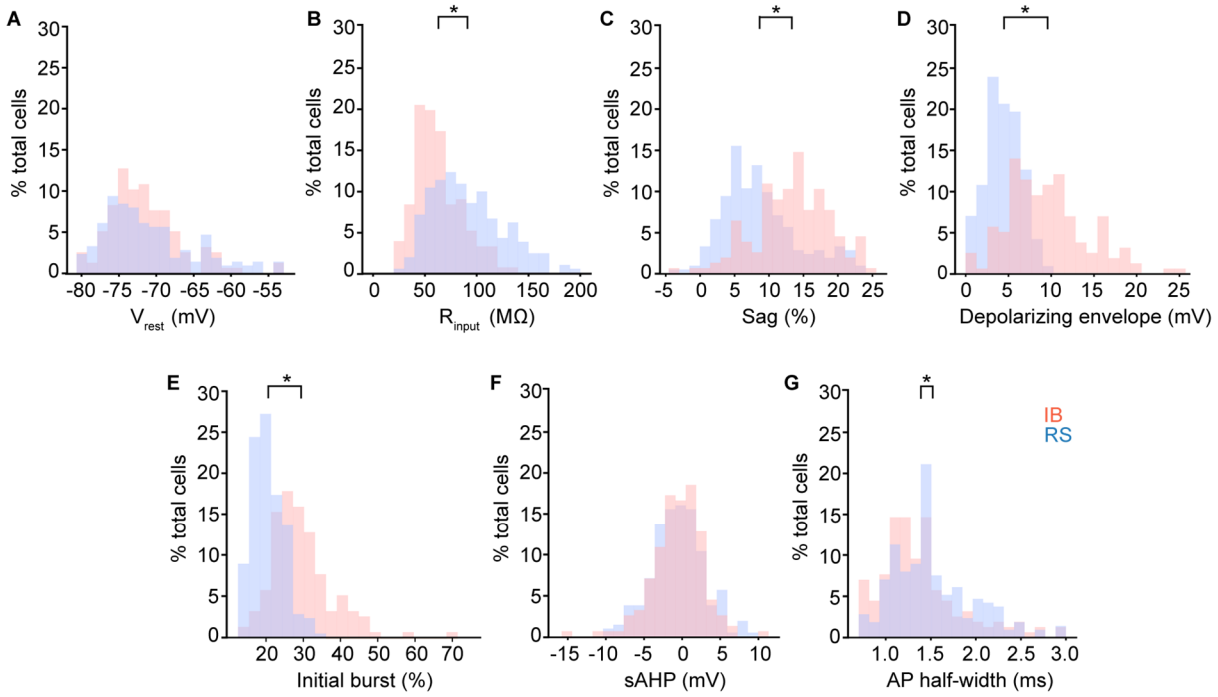

Figure 7. Intrinsic membrane properties in IB and RS cells. Distributions of IB (red) and RS (blue) cell (**A**) resting membrane potential (Vrest), (**B**) input resistance (Rinput), (**C**) sag, (**D**) magnitude of the depolarizing envelope, (**E**) initial action potential burst, (**F**) slow afterhyperpolarization (sAHP), and (**G**) action potential half-width. *: $p < 0.05$, two-sample t-test.

Chrimson to blue light (Klapoetke et al., 2014), leading to potential coactivation of afferents by 440nm excitation. To address this issue and ensure input selectivity, I limited blue light pulses under a maximal duration and power for 440nm excitation that averts opsin cross-activation (see Chapter 1). In layer 5 of the PPC, I observed similar proportions of intrinsic bursting (IB) and regular spiking (RS) pyramidal neurons (IB 42.4%, RS 57.6%, n = 369, Figure 6D). The two cell types were identified by differences in action potential firing pattern, input resistance, and the magnitude of the depolarizing envelope (initial AP firing: IB 29.4 ± 0.7%, RS 20.6 ± 0.3%, $p < 0.001$; input resistance: IB 61.8 ± 2.1 MΩ, RS 91.1 ± 2.4 MΩ, $p < 0.001$; depolarizing envelope: IB 9.6 ± 0.4 mV, RS 4.4 ± 0.1 mV, $p < 0.001$; IB n = 156, RS n = 213; mean ± SEM; independent samples t-test; Figure 6E and 7). IB and RS neurons also differed in voltage sag

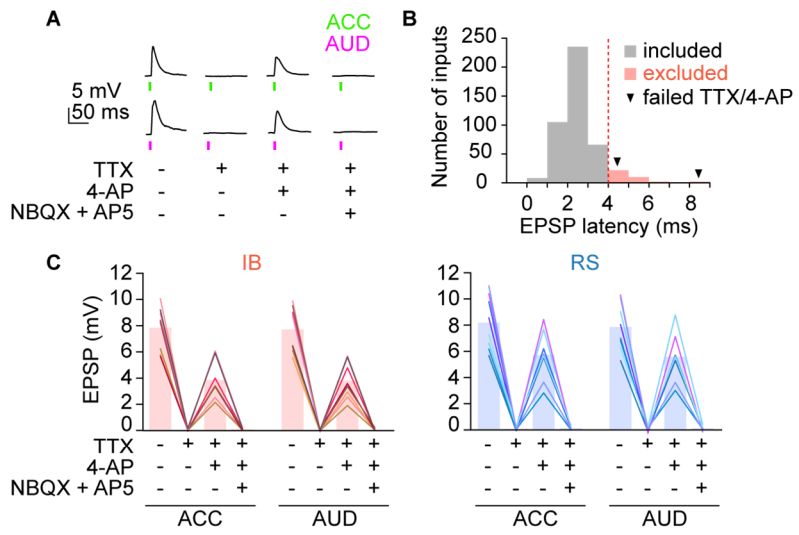

Figure 8. Pharmacological approach for testing dual monosynaptic connections. (**A**) Example traces showcasing the TTX/4-AP approach for determining dual monosynaptic connections. TTX (1 μM) abolishes all optogenetic-evoked postsynaptic responses. Addition of 4-AP recovers responses from afferents with monosynaptic but not polysynaptic innervation. Dual response recovery from both afferents indicates converging monosynaptic connections. Blocking glutamatergic transmission abolishes all responses. Colored bars under voltage traces indicate timing of light stimuli used to activate ACC (green) or AUD (magenta) afferents.(**B**) Distribution of evoked EPSP latencies of all recorded cells. Latencies of cells which failed the TTX/4-AP pharmacological test are indicated by black arrowheads. Dashed red line represents latency cutoff used to determine monosynaptic inputs. (**C**) Response amplitudes of IB (red, n = 8) and RS (blue, n = 8) neurons in the TTX/4-AP experiment. Individual cells are represented by distinct shades of color.

ratio and action potential half-width (voltage sag ratio: IB 13.29 ± 0.43 %, RS 8.63 ± 0.38 %, $p < 0.001$; action potential half-width: IB 1.39 ± 0.04 ms, RS 1.52 ± 0.03 ms, $p = 0.008$, Figure 7C and G), while no differences in resting membrane potential or slow afterhyperpolarization were observed (resting membrane potential: IB -71.5 ± 0.44 mV, RS -70.5 ± 0.56 mV, $p =$ 0.175; slow afterhyperpolarization: IB -0.55 ± 0.27 mV, RS -0.55 ± 0.24 mV, $p = 0.993$; IB n = 156, RS n = 213; mean ± SEM; see *Methods*, Figure 7A and F). To determine whether inputs were mono- or polysynaptic, I used the TTX/4-AP pharmacological method (Petreanu et al., 2009) (Figure 8A and B). I found that the application of 4-AP (100-500 mM) after TTX (1 mM) restored glutamatergic synaptic responses to both ACC and AUD afferent activation in the majority of layer 5 cells (Figure 8C), indicating monosynaptic dual innervation. These experiments suggested that synaptic latencies for verified monosynaptic inputs were no longer than 4 ms (Figure 8B). I furthermore tested whether layer 5 pyramidal neurons received direct input from frontal-visual and auditory-visual afferent combinations (Figure 9A and B). To

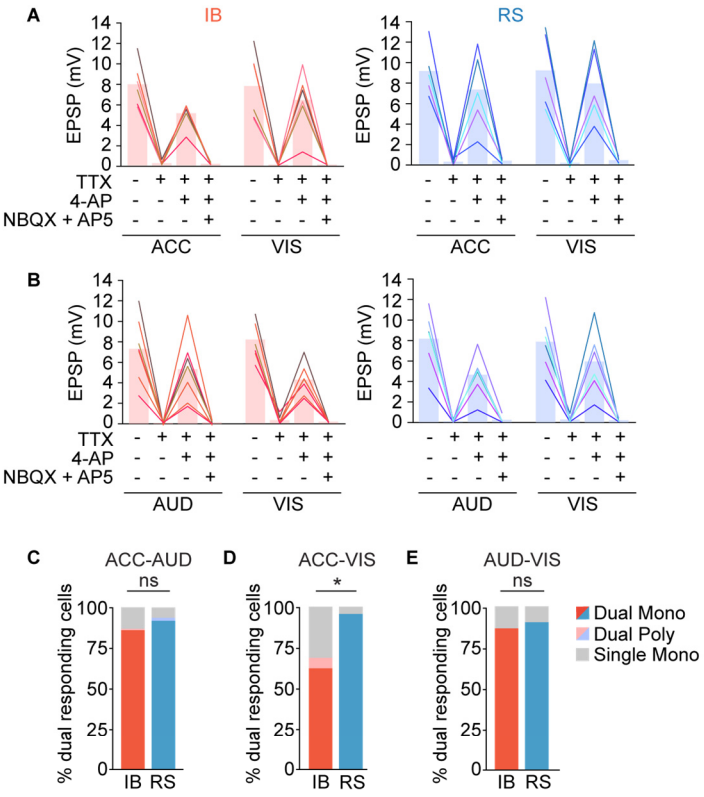

Figure 9. Dual monosynaptic innervation of layer 5 PPC neurons by feedforward and feedback afferents. (**A**) Bath application of TTX (1 μM) abolishes IB (red) and RS (blue) evoked postsynaptic responses to ACC and VIS afferent stimulation. Responses are recovered by the addition of 4-AP (indicating a monosynaptic connection). Addition of NBQX and AP5 eliminates all responses, confirming they are from glutamatergic synapses. Both inputs were tested within the same cells. Bars represent average EPSP amplitudes. Colored lines indicate individual cells (IB, n = 6; RS, n=5). (**B**) Pharmacological test of monosynaptic AUD / VIS dual innervation in IB (red) and RS (blue) cells (IB, n = 7; RS, n = 6). (**C**) Bars represent the proportion of IB and RS neurons receiving converging ACC and AUD inputs. (**D**) Proportion of IB and RS neurons receiving converging ACC and VIS inputs. (**E**) Proportion of IB and RS neurons receiving converging AUD and VIS inputs. *: p < 0.05, two-sided Fisher's exact test.

distinguish between mono- and polysynaptic inputs and estimate the proportion of dual innervated cells, I applied the above 4 ms latency cutoff to evoked responses in all recorded cells (see *Methods*). I found that IB and RS neurons were equally likely to receive monosynaptic dual innervation from ACC and AUD afferents (IB 91/107, RS 92/101 cells, p = 0.205, two-sided Fisher's exact test, Figure 9C). IB cells were significantly less likely to receive monosynaptic dual input from ACC and the visual cortex (VIS) than RS neurons (IB 10/16, RS 22/23 cells, p = 0.013, Figure 9D), and were equally likely to receive dual innervation from AUD and VIS (IB 13/15, RS 19/21 cells, p > 0.999, Figure 9E). Only cells receiving monosynaptic dual input (based on passing the TTX/4AP test or displaying less than 4 ms synaptic latency for both inputs) were included in further analysis. Together, these data suggest that a large proportion of IB and RS neurons in PPC layer 5 receive direct, converging excitation from feedforward and feedback sources.

Temporal profiles of feedforward-feedback integration are cell-type specific

I next sought to determine the temporal dynamics of the interaction between converging feedforward and feedback inputs in IB and RS cells (Figure 10A). I recorded light evoked unimodal EPSPs in response to independent activation of ACC or AUD afferents (Figure 10B and C). Unimodal recordings were then interleaved with multimodal trials where the two afferents were co-activated with 0, 50, 100, or 250 ms delay between the light pulses (Figure 10D and E). To quantify synaptic interactions, I calculated a Multimodal Enhancement Index (MEI) by dividing the amplitude of the recorded multimodal response by the summed amplitude of unimodal responses (see *Methods*). An MEI of 1 would thus indicate a linear interaction. By plotting MEI values against the respective synaptic delay, I

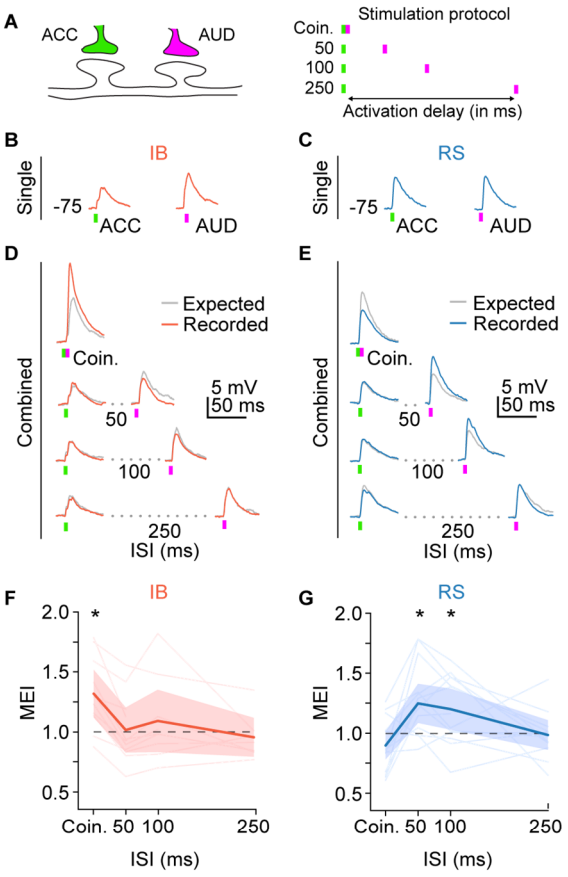

Figure 10. Cell type-specific nonlinear integration of feedforward and feedback synaptic inputs. (**A**) Illustration of dual, monosynaptic innervation (left) and the stimulation protocol (right). (**B**) IB cell response to unimodal stimulation of ACC or AUD afferents. (**C**) RS cell response to unimodal stimulation of ACC or AUD afferents. (**D**) Representative IB cell responses to combined stimulation of ACC and AUD afferents activated with 0 (coincident), 50, 100, or 250ms delay between inputs. Recorded traces (red) are overlaid on the calculated linear response (grey). (**E**) Representative RS cell responses to combined stimulation of ACC and AUD afferents (blue) and the predicted linear response (grey). (**F**) Temporal dynamics of ACC-AUD integration in IB neurons (light red lines). Dark red line represents population mean; shaded area represents 95% CI. (**G**) Temporal dynamics of ACC-AUD integration in RS cells (light blue lines). Dark blue line represents population mean; shaded area represents 95% CI. Dashed black line in (F) and (G) indicates linear integration. *: $p < 0.05$, t-test.

captured temporal integration profiles for IB and RS cells (Figure 10F and G). In IB cells, coincident activation of ACC and AUD inputs resulted in an evoked response amplitude 34% greater than the linear sum (MEI = 1.34, p = 0.002, n = 11, t-test, Figure 10F). This enhancement was absent when AUD afferents were activated following ACC inputs with any delay (50 ms: MEI = 1.02, p = 0.740; 100 ms: MEI = 1.09, p = 0.652; 250 ms: MEI = 0.95, p = 0.425; Figure 10F). Conversely, in RS cells, coincident activation of ACC and AUD inputs resulted in linear integration (MEI = 0.90, p = 0.085, n = 15, t-test, Figure 10G). However, when ACC and AUD inputs arrived at RS cells with a 50-100 ms delay, evoked EPSPs were significantly larger than what linear summation predicted (50 ms: MEI = 1.25, p = 0.005; 100 ms: MEI = 1.20, p = 0.025; 250 ms: MEI = 0.99, p = 0.839; Figure 10G). Two-way ANOVA revealed that IB and RS cells integrate ACC and AUD inputs with distinct temporal dynamics (cell type × synaptic delay

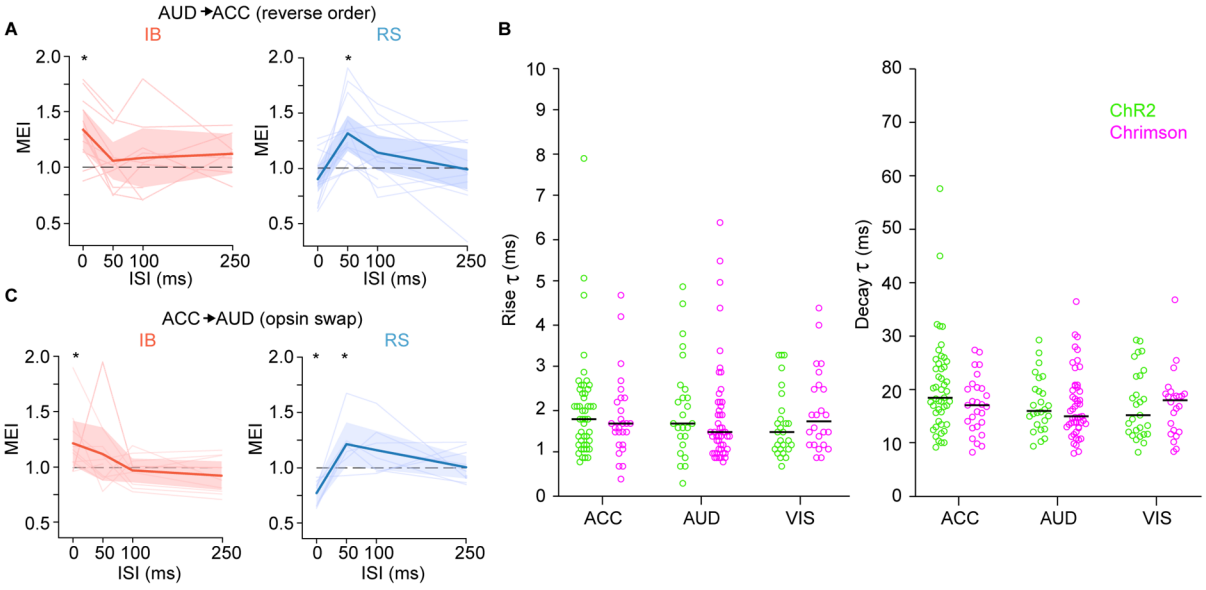

Figure 11. Temporal dynamics of synaptic integration are independent of stimulus order and opsin indentity. (**A**) Integration profiles of IB (red) and RS (blue) cells in response to stimulating ACC and AUD afferents in reverse order compared to Figure 9F and G. Light lines represent independent observations (mouse averaged), dark lines and shaded regions indicate mean ± 95% CI. Due to interleaved sampling in these experiments, n-numbers throughout this figure match the sample size in Figure 9. *: $p < 0.05$, t-test. (**B**) Rise time constants (τ) of evoked EPSPs when expressing either ChR2 (green) or Chrimson (magenta) in ACC (nChR2 = 47, nChrimson = 27), AUD (nChR2 = 26, nChrimson = 49), or VIS (nChR2 = 27, nChrimson = 24). Horizontal lines indicate mean rise τ. (B) Decay time constants (⊠) of ChR2 (green) or Chrimson (magenta) stimulus evoked EPSPs in ACC, AUD, or VIS. Horizontal lines indicate mean decay τ. Individual cells are plotted, IB and RS cells were pooled in this dataset. *: $p < 0.05$, one-way ANOVA with Sidak's correction for multiple comparisons, no significant differences observed. (**C**) Integration profile of IB (red, n = 10) and RS (blue, n = 8) neurons with opsin expression swapped between input afferents. Here, ChR2 was expressed in AUD, while Chrimson was expressed in ACC. Dark lines and shaded regions indicate mean ± 95% confidence interval. Light lines represent individual animals. *: $p < 0.05$, t-test.

interaction $F_{3, 60} = 11.9$, $p < 0.0001$).

To test whether the sequence of inputs influenced feedforward-feedback interactions, I activated afferents in reverse order, with ACC inputs following AUD afferent activation (Figure 11A). I found that changing the order of inputs had no effect on the temporal dynamics of synaptic integration in either cell type (input order × synaptic delay interaction in IB cells $F_{3, 48} = 0.65$, $p = 0.588$; in RS cells $F_{3, 73} = 0.21$, $p = 0.887$; two-way ANOVA). Furthermore, activating ACC and AUD afferents in reverse order preserved the cell-type specificity of integration profiles (cell type × synaptic delay interaction in reversed input order: $F_{3, 61} = 11.23$, $p < 0.0001$, two-way ANOVA).

A potential caveat of all above experiments is that ChR2 and Chrimson have distinct channel kinetics (Klapoetke et al., 2014), thus rigid opsin-afferent pairings may bias integration dynamics. To address this issue, I measured EPSP rise, and decay time constants evoked by either ChR2 or Chrimson activation. I found no difference in ChR2 and Chrimson EPSP kinetics in any of the tested afferents (ChR2 vs. Chrimson: ACC, rise: $p = 0.823$, decay: $p = 0.106$; AUD, rise: $p = 0.889$, decay: $p > 0.999$; VIS rise: $p = 0.677$, decay: $p > 0.999$; one-way ANOVA with Sidak's correction for multiple comparisons, Figure 11B). Furthermore, temporal dynamics of ACC-AUD integration were not affected by reversing the opsin expression between afferents, i.e., ACC transduced with Chrimson and AUD with ChR2 (opsin target × synaptic delay interaction in IB cells: $F_{3, 49} = 1.56$, $p = 0.211$; in RS cells: $F_{3, 55} = 0.48$, $p = 0.697$; two-way ANOVA; Figure 11C). The observed cell-type specificity of feedforward-feedback synaptic interactions remained robust against changing upstream opsin identities (cell type × synaptic delay interaction $F_{3, 44} = 7.52$, $p = 0.0004$, two-way ANOVA in reverse opsin experiments).

These results demonstrate nonlinear subthreshold interactions between frontal and auditory inputs in layer 5 pyramidal neurons of the PPC and indicate that IB and RS cells integrate feedback signals with feedforward inputs with distinct temporal dynamics.

Distinct combination of ionic mechanisms underpins coincident and delayed supralinearity

I next sought to identify the mechanisms underlying the temporal dynamics of nonlinear synaptic integration. Neuronal dendrites are rich in channels that allow for a diverse range of nonlinear computations (Stuart and Spruston, 2015). Among the most well-studied are dendritic spikes caused by regenerative currents through Na^+ channels (Ariav et al., 2003; Golding and Spruston, 1998; Kim and Connors, 1993), Ca^{2+} channels (Golding et al., 1999; Kim and Connors, 1993; Larkum and Zhu, 2002; Losonczy and Magee, 2006; Schiller et al., 1997), or N-methyl-D-aspartate (NMDA) receptors (Polsky et al., 2004; Schiller et al., 2000, 1997). To explore the interaction of these conductances and determine their contribution to nonlinear synaptic events, I collaborated with Dr.

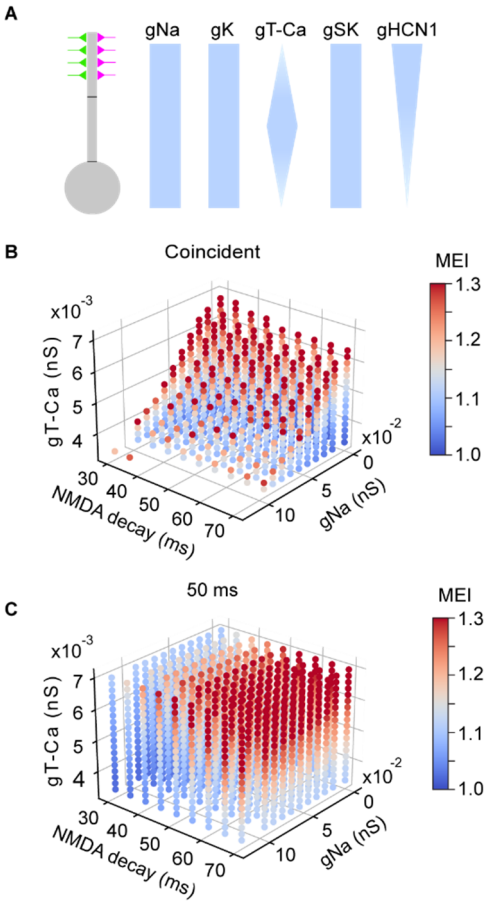

Figure 12. Differential involvement of ionic conductances to coincident and delayed integration. (**A**) Schematic illustrating the distribution of channel conductances along the model compartments (distal dendrite, proximal dendrite, and soma). gNa, Hodgkin-Huxley-type sodium conductance; gK, Hodgkin-Huxley-type potassium conductance; gT-Ca, T-type calcium conductance; gSK, calcium-dependent small potassium conductance; gHCN1, hyperpolarization-activated cyclic nucleotide-gated nonspecific cationic channel 1 conductance. (**B**) Computational model exploring coincident (0 ms delay) integration MEI values across a parameter space with varying sodium and calcium channel conductance and NMDA receptor decay constant. Missing points represent parameter combinations where coincident inputs drove the model past action potential threshold. (**C**) MEI values for delayed (50 ms) synaptic integration across the same parameter space as in (B).

Archana Proddutur in Dr. Gyorgy Lur's lab, who built a computational model (see *Methods*) of a theoretical L5 neuron (Figure 12A). All computational modelling described throughout this dissertation was performed by Dr. Proddutur. To determine the role of sodium-, and calcium channels, and NMDA receptors in synaptic integration, Dr. Proddutur independently varied channel conductance or NMDA receptor decay kinetics, while keeping all other parameters fixed. In the resulting 1881 variations of the model, Dr. Proddutur calculated MEI values for simulated EPSPs evoked by stimulating modelled glutamatergic synapses (see *Methods*) simultaneously or with 50ms delay. Increasing sodium conductance resulted in the enhancement of coincident inputs (Figure 12B) but had no effect on synaptic integration when synaptic events were delayed by 50 ms (Figure 12C). In contrast, higher calcium channel conductance led to enhanced integration of both coincident and delayed inputs (Figure 12B and C). Varying NMDA receptor decay kinetics had minimal effect on coincident integration but had a marked influence on synaptic interactions at 50 ms delay (Figure 12B and C).

These results suggest that sodium and calcium conductances drive supralinear multimodal integration when inputs coincide while the interaction of calcium conductance and NMDA receptor decay kinetics determines integration at longer synaptic delays.

Temporal dynamics of synaptic integration are shaped by cell-type specific inhibition

I next asked whether the above mechanisms explained the distinct integration profiles of IB and RS cells. Out of our initial 1881 models (black dots in Figure 13A), 201 variations (10.6%) captured the observed integration profile of IB cells with a 99% confidence interval (red crosshair). However, no combination of these ionic mechanisms approximated our results from RS cells (blue crosshair, Figure 13A). We thus considered that a non-cell autonomous

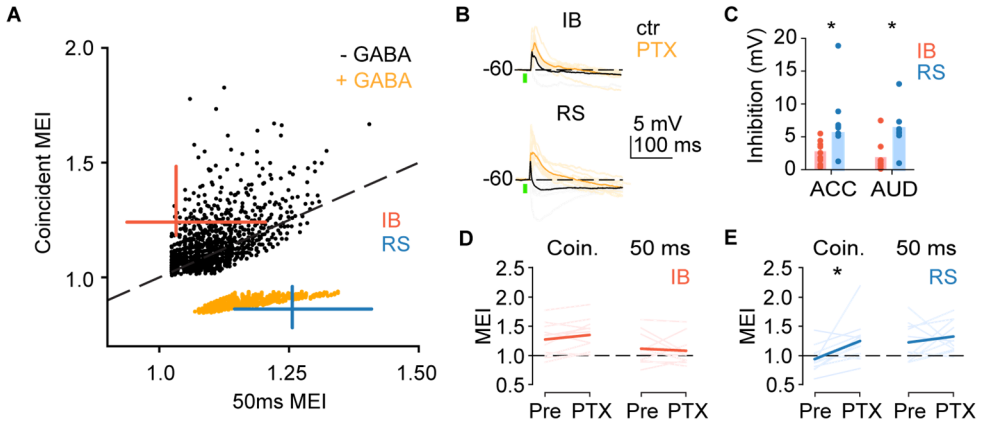

Figure 13. Coincident integration in RS cells is linearized by a feedforward inhibitory circuit.
(**A**) Relationship of coincident and delayed MEI values in all model variations without inhibition (black dots) and with the inclusion of feedforward inhibition (orange dots). Crosshairs represent ranges of all in vitro recorded IB (red) and RS (blue) neurons. Error bars show 99% CI and cross at the data median. (**B**) ACC stimulation evoked EPSPs in IB (top) and RS (bottom) cells before (black) and after (orange) GABAA receptor block with picrotoxin (PTX). (**C**) Comparison of GABAA-mediated inhibition in IB (red) and RS (blue) cells. Bars represent means. *: $p < 0.05$, unpaired t-test. (**D**) $GABA_A$ block (PTX) has no effect on coincident and delayed ACC-AUD integration in IB cells (red). (**E**) $GABA_A$ block (PTX) unmasks supralinear integration of coincident inputs in RS neurons (blue). *: $p < 0.05$, paired t-test.

mechanism may shape the integration profile of these cells. RS neurons have been reported to receive higher inhibitory drive than their IB counterparts (Hefti and Smith, 2000; Sun et al., 2013). Consistent with these findings, I observed stronger feedforward inhibition in RS cells compared to IB neurons (ACC $p = 0.019$; AUD $p = 0.006$; IB $n = 8$, RS $n = 9$; unpaired t-test, Figure 13B and C). The strength of inhibition recruited by ACC and AUD afferents was indistinguishable (IB cells: $p = 0.159$, $n = 9$; RS cells: $p = 0.401$, $n = 8$; paired t-test; Figure 13C). To test the hypothesis that feedforward inhibition shapes the integration profile of RS, but not IB cells, I measured coincident and delayed integration in the presence of the $GABA_A$ receptor antagonist picrotoxin (PTX, 6 μM). I found that PTX had no effect on coincident or delayed ACC-AUD interaction in IB cells (coincident: $p = 0.112$, $n = 8$; 50 ms delay: $p = 0.947$, $n = 10$; Figure 13D). Conversely, in RS neurons, bath application of PTX enhanced coincident integration by 32% (to MEI = 1.24, $p = 0.023$, $n = 10$, paired t-test, Figure 13E) leading to supralinear summation ($p = 0.048$, t-test). Similarly, including the non-membrane permeable

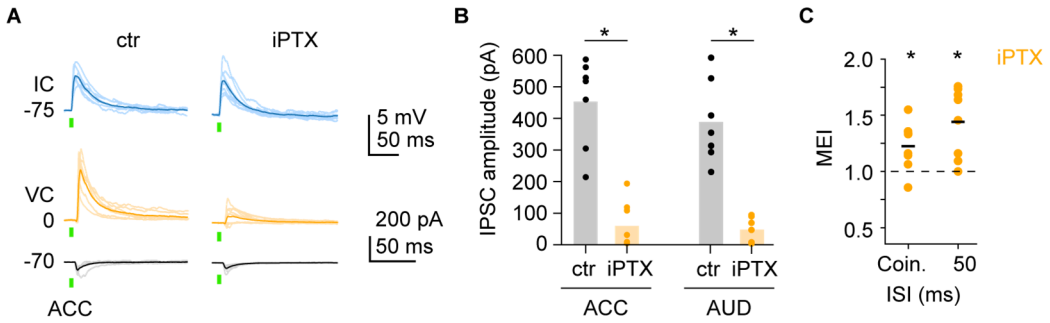

Figure 14. Internal block of $GABA_A$ receptors uncovers coincident supralinear integration (**A**) Excitatory postsynaptic currents (EPSCs, black), inhibitory postsynaptic currents (IPSCs, orange) and excitatory postsynaptic potentials (EPSPs, blue) recorded from RS cells. Thin lines are individual recordings, thick lines are means. Inlcusionof picrotoxin (10 μM) in the intracellular recording pipette (iPTX) lowers IPSC amplitude. (**B**) Comparison of IPSC amplitude between control and internal $GABA_A$ block. *: $p < 0.001$, n = 7 control, 8 internal PTX, t-test. (**C**) MEI values measured in RS neurons with internal $GABA_A$ block. *: $p < 0.05$, one sample t-test.

PTX in the internal solution (10 mM) which is effective at selectively reducing inhibitory currents in patched cells (Figure 14A and B) (Akaike et al., 1985; Atherton et al., 2016; Inomata et al., 1988; Metherate and Ashe, 1993), enhanced coincident integration in RS neurons (coincident MEI_{iPTX} = 1.23, p = 0.02, 50 ms delay MEI_{iPTX} = 1.44, p = 0.005, n = 8, one-sample t-test., Figure 14C). These data suggested that integration of coincident inputs in RS cells was shaped by feedforward inhibition.

To test whether the relative kinetics of excitation and inhibition are permissive to this interaction, I next compared EPSP, EPSC, and IPSC kinetics recorded from the same RS cells (Figure 15A–C). EPSP peaks were reached later than the rise time constant of the IPSC (pACC = 0.006, pAUD = 0.005, n = 7, paired t-test) but earlier than the decay constant (pACC = 0.0006, pAUD < 0.0001, n = 7, paired t-test), suggesting that ACC and AUD induced EPSPs peak during the strongest inhibitory effect (Figure 15D and E). Supralinear delayed (50 ms) integration in RS cells was unaffected by bath applied PTX (p = 0.42, n = 11, paired t-test; Figure 13E), or by PTX in the pipette solution (MEI_{50ms} = 1.44, p = 0.005, n = 8, one-sample t-test; Figure 14C). This indicated that inhibition may be reduced when inputs were delayed. Indeed, recording inhibitory

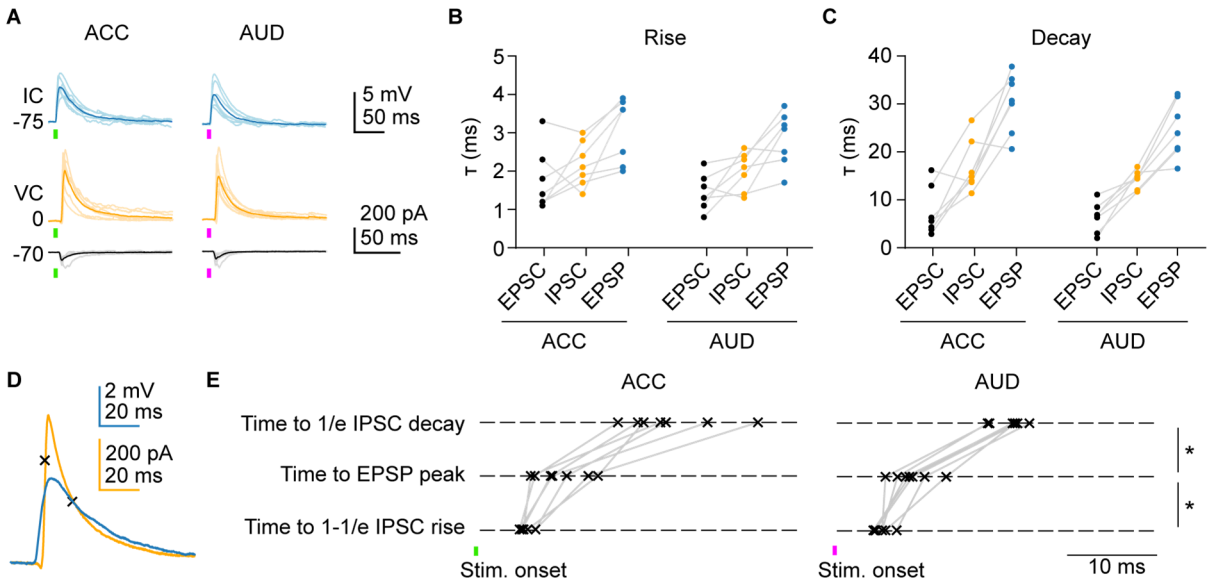

Figure 15. Relative kinetics of excitatory and inhibitory currents in RS cells. (**A**) Excitatory postsynaptic currents (EPSCs, black), inhibitory postsynaptic currents (IPSCs, orange) and excitatory postsynaptic potentials (EPSPs, blue) recorded from RS cells. Thin lines are individual recordings, thick lines are means. Traces from ACC activation are identical to those in Figure 14A. (**B**) Relative rise constants of EPSCs, IPSCs and EPSPs recorded following the activation of ACC and AUD inputs to RS cells. (**C**) Relative decay constants for the same recordings as in B. in B and C, data points connected by grey lines represent individual recordings. (**D**) Example EPSP (blue) and IPSC (orange) to showcase relative kinetics. 1/e points of IPSC rise and decay are marked by x. (**E**) Relative timing of IPSC rise (bottom), EPSP peak (middle) and IPSC decay (top). EPSP peak is reached later than the 1/e rise point of the IPSC (pACC = 0.006, pAUD = 0.005, n = 7, paired t-test) but earlier than the 1/e decay point (pACC = 0.0006, pAUD < 0.0001, n = 7, paired t-test), suggesting that EPSP peaks during the strongest inhibitory effect. Points connected by grey lines represent individual recordings.

postsynaptic currents (IPSCs) evoked by sequential activation of ACC and AUD afferents revealed depressing short-term synaptic dynamics (approximately 39% depression at 50 ms, Figure 16A and B). Thus, Dr. Proddutur incorporated feedforward inhibition in the above detailed computational model (Figure 16C) and calculated the MEI of EPSPs simulated with varying sodium, calcium and NMDA decay parameters. Now

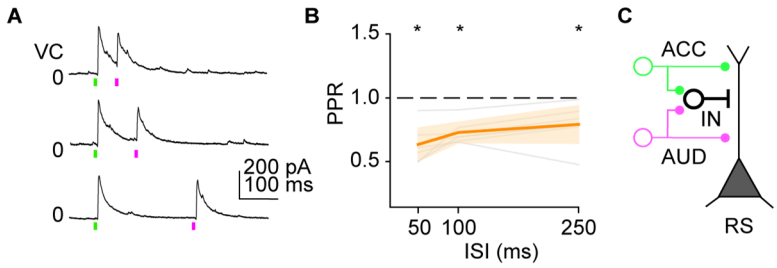

Figure 16. Depressing short-term dynamics of feedforward inhibition to RS cells. (**A**) Example IPSCs evoked by combined activation of ACC (green) and AUD (magenta) afferents with 50, 100 and 250 ms delays. (**B**) Paired pulse ratio (PPR) of IPSCs evoked by sequential stimulation of ACC and AUD inputs. Dark orange line and shaded region indicates mean ± 95% confidence interval, grey lines show individual recordings (n = 8). Light lines represent individual cells. *: p < 0.05, t-test. (**C**) Schematic model incorporating feedforward inhibition.

including a depressing GABAergic synapse, Dr. Proddutur generated and additional 1881 model variations, allowing us to capture the integration characteristics of RS neurons (Figure 13A).

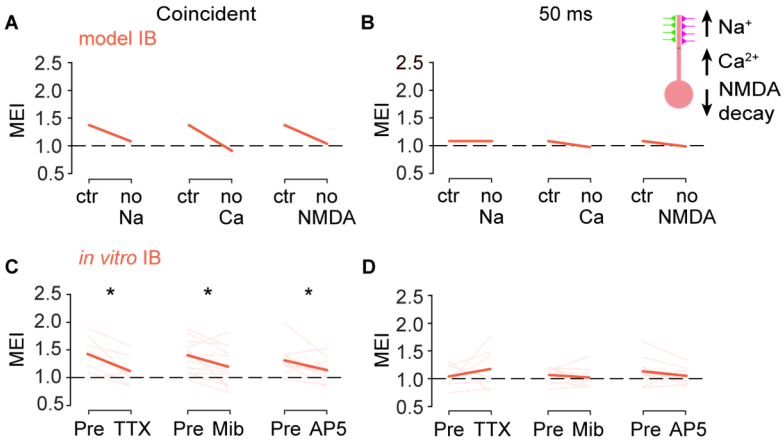

Figure 17. Pharmacological testing of IB model predictions. (**A**) Simulating the effect of blocking sodium channels, calcium channels, or NMDA receptors on coincident integration in a model IB neuron. (**B**) Simulating the effect of channel blockers on delayed (50 ms) integration in a model IB neuron. Inset: schematic of channel and synapse distribution in model IB neurons. (**C**) The effect of pharmacological inhibition of sodium (low concentration (100 nM) of TTX), T-type calcium (Mib) and NMDA receptors (AP5) on coincident integration of ACC and AUD afferents in IB neurons in vitro. (**D**) The effect of the above pharmacological manipulations on delayed (50 ms) integration of ACC and AUD afferents in IB neurons in vitro. *: $p < 0.05$, paired t-test.

In vitro *pharmacology confirms model predictions*

The above models predict that specific ionic conductances support the enhancement of coincident inputs to IB cells and delayed inputs to RS neurons. To test these predictions, Dr. Proddutur first created a model cell with medium-high sodium (0.065 nS) and calcium (0.0048 nS at the proximal dendrite) conductance and fast NMDA decay kinetics (t = 30 ms) to approximate IB neurons. This model produced supralinear integration of coincident inputs (MEI = 1.38) but linear addition at 50ms delay (MEI = 1.04, Figure 17A and B). Blocking sodium, calcium, or NDMA conductances in the model, resulted in near linear coincident integration ($MEI_{Na\text{-}block}$: 1.08, $MEI_{Ca\text{-}block}$

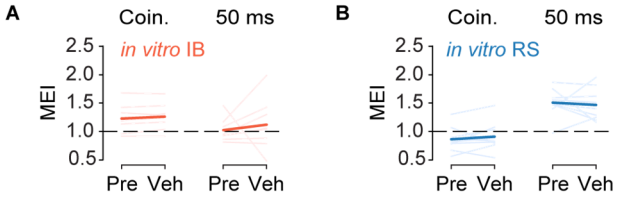

Figure 18. Integration profiles are stable over extended whole cell recordings. (**A**) Multimodal enhancement index (MEI) values of coincident and delayed (50 ms) ACC-AUD integration in IB cells prior to (Pre) and after (Veh) addition of drug vehicle to the perfusate for the same time period as used in pharmacology experiments. IB comparison between Pre and Veh: pcoin = 0.14, p50ms = 0.61, n = 8, paired t-test. IB nonlinearity: pcoin-Pre = 0.036, pcoin-Veh = 0.016, p50ms-Pre = 0.76, p50ms-Veh = 0.48, one-sample t-test. (**B**) MEI values of coincident and delayed (50 ms) ACC-AUD integration in RS cells prior to (Pre) and after (Veh) addition of drug vehicle. RS comparison between Pre and Veh: pcoin = 0.45, p50ms = 0.71, n = 9, paired t-test. RS nonlinearity: pcoin-Pre = 0.088, pcoin-Veh = 0.31, p50ms-Pre < 0.001, p50ms-Veh = 0.001, one-sample t-test.

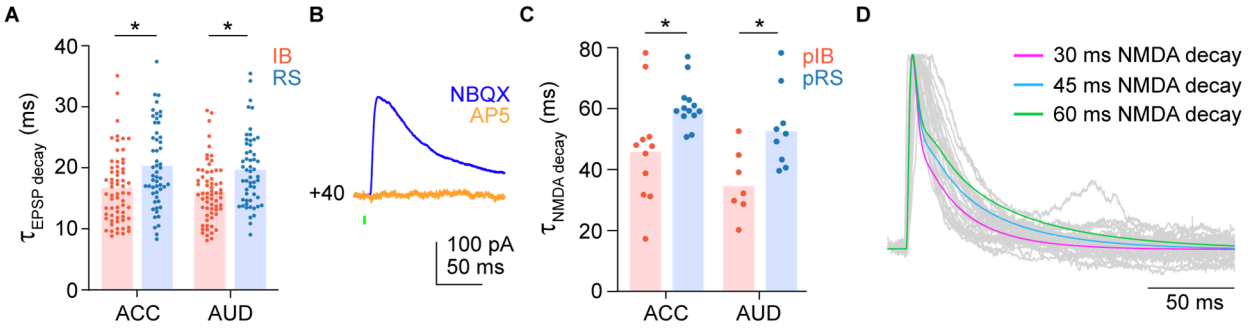

Figure 19. Cell-type-specific EPSP and NMDA receptor decay kinetics. (**A**) Comparison of ACC and AUD inactivation evoked EPSP decay kinetics between IB (red) and RS (blue) neurons. *: $p < 0.05$, nIB = 63, nRS = 54, t-test. (**B**) Representative voltage clamp recording of NMDA receptor current in the presence of NBQX (blue) and NMDA receptor current after the addition of AP5 (yellow). (**C**) Comparison of ACC and AUD fiber activation evoked NMDA receptor current decay kinetics between putative IB and putative RS cells. *: $p < 0.05$, ACC: nIB = 11, nRS = 13, AUD: nIB = 7, nRS = 9, t-test. (**D**) Simulated EPSPs with varied NMDA decay kinetics (30 ms: magenta, 45 ms: blue, 60 ms: green) overlayed on *in vitro* recorded EPSPs (grey).

= 0.909, $MEI_{NMDA\text{-}block}$ = 1.04 Figure 17A). I then conducted the same experiments *in vitro*, recording ACC-AUD integration in IB neurons while bath applying pharmacological blockers. Supralinear integration of coincident inputs was diminished by bath application of a low-concentration (100 nM) of the Na^+ channel blocker tetrodotoxin (TTX, MEI reduction of 0.31, p = 0.030, n = 7 cells; paired t-test, Figure 17C). Coincident supralinearity was also reduced by the T-type Ca^{2+} channel blocker mibefradil (Mib, 20 µM, 0.26 reduction in MEI, p = 0.016, n = 8; Figure 17C) and to a lesser extent by the NMDA receptor antagonist D-2-amino-5-phosphonovalerate (AP5, 50 µM, 0.18 reduction in MEI, p = 0.034, n = 11; Figure 17C). In IB cells, linear integration at 50 ms synaptic delay was unaffected by any of the tested agents (TTX: p = 0.457, n = 7; Mib: p = 0.070, n = 8; AP5: p = 0.155, n = 11; Figure 17D). Vehicle flow-in for equivalent time periods resulted in no change in synaptic integration in IB cells ($p_{coincident}$ = 0.14, p_{50ms} = 0.61, paired t-test, n = 7, Figure 18A).

To simulate coincident and delayed integration in RS cells, Dr. Proddutur next generated a model neuron with low sodium conductance (0.015 nS), high calcium conductance (0.0062 nS at the proximal dendrite) and slow NMDA receptor decay kinetics (t = 60 ms). This model RS

neuron also included feedforward inhibition targeting the excitatory recipient dendritic segment. The use of longer NMDA receptor decay kinetics in this model was supported by longer decay time constants observed both in EPSPs (Figure 19A) and NMDA currents (Figure 19B and C) of RS and putative RS (identified via retrograde labelling, see *Methods,* Figure 20) neurons *in vitro*. Model RS cell EPSP kinetics fell within the range of recorded EPSPs (Figure 19D). Our RS neuron model, now including inhibition, produced near-linear coincident integration (MEI = 0.90) that was unaffected by blocking sodium, calcium or NMDA conductances (shown in orange in Figure 21A). Similarly to my observations of RS neurons *in vitro*, simulations produced supralinear synaptic interaction when the inputs were delayed by 50 ms (50 ms MEI = 1.22, Figure 21B). Delayed supralinearity persisted in the absence of sodium conductance (50 ms $MEI_{Na\text{-}block}$ = 1.22), however, it was abolished by removal

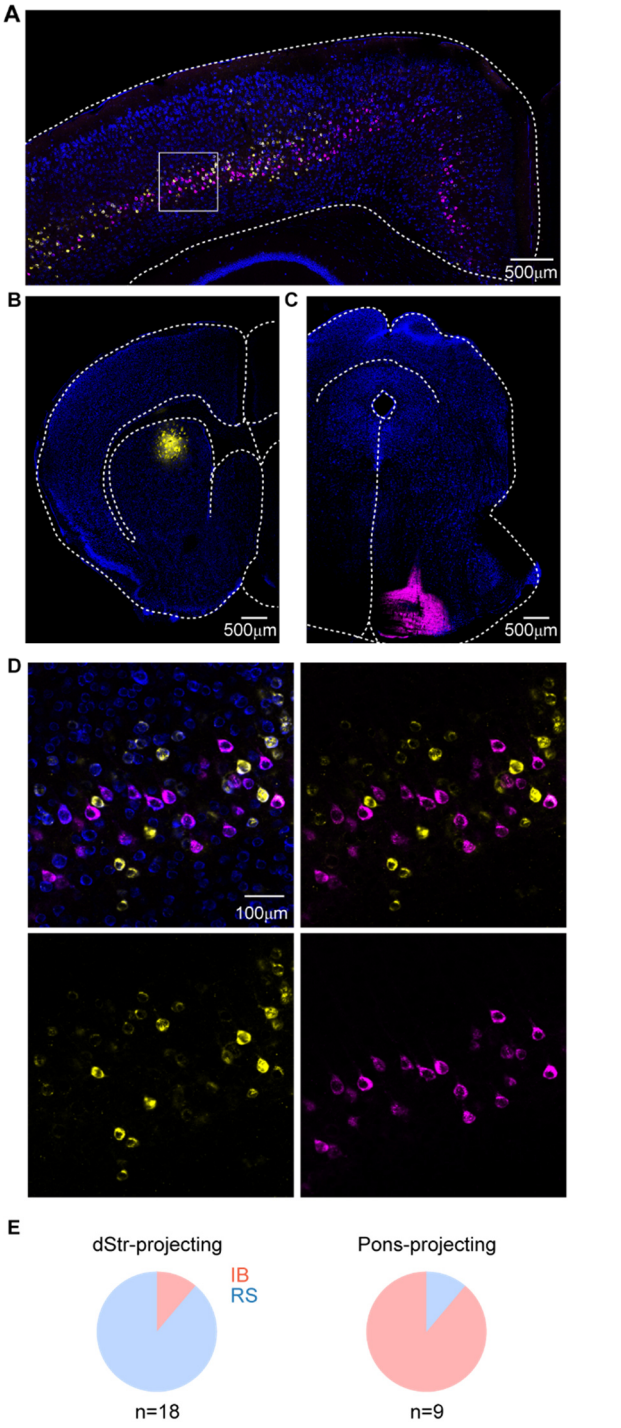

Figure 20. Projection-specific labelling of IB and RS cells. (**A**) Example fluorescence image showing the distribution of dorsal striatum (yellow) and pons (magenta) projecting neurons in the PPC (n = 8). Scale bar is 500 µm. (**B**) representative image of the dorsal striatum injection site (yellow). (**C**) Representative image of the pons injection site (magenta). Scale bar in B and C are 500 µm.(**D**) High magnification images of striatal (yellow) and pons (magenta) projection cells in the PPC region highlighted by a white rectangle in A. Scale Bar is 100 µm. (**E**) Proportion of dStr (left) and pons (right)-projecting PPC neurons that are categorized as IB or RS cells.

of calcium or NMDA conductances (50 ms $MEI_{Ca\text{-}block}$ = 0.98, 50 ms $MEI_{NMDA\text{-}block}$ = 1.07, Figure 21A and B). I then reproduced these experiments *in vitro*, recording AUD-ACC integration in RS neurons while bath applying pharmacological blockers. Coincident integration in RS cells was unaffected by drug treatment (TTX (100 nM): p = 0.687, n = 6; Mib: p = 0.154, n = 6; AP5: p = 0.185, n = 10; paired t-test, Figure 21C). At 50 ms synaptic delay, TTX had no effect on integration (p = 0.511, n = 7; Figure 21D). However, application of both Mib and AP5 significantly reduced multimodal enhancement of delayed inputs (Mib: 0.41 reduction in MEI, p = 0.020, n = 6; AP5: 0.28 reduction in MEI, p = 0.005, n = 11; paired t-test, Figure 21D). Vehicle flow-in did not alter integration in RS cells ($p_{coincident}$ = 0.45, p_{50ms} = 0.71, paired t-test, n = 8, Figure 18B).

These data indicate that the expression of high sodium and calcium conductances combined with fast NMDA receptor decay cause IB neurons to act as coincidence detectors of feedforward and feedback inputs. Conversely the temporal dynamics of synaptic integration in RS neurons is determined by two factors: an interaction of high Ca^{2+} conductance and slow NMDA receptor decay kinetics drive supralinear addition of delayed inputs while $GABA_A$ mediated feedforward inhibition linearizes coincident integration.

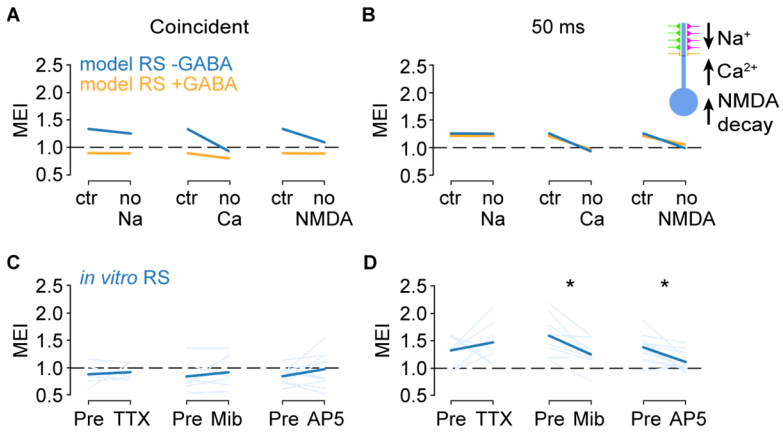

Figure 21. Pharmacological testing of RS model predictions. (**A**) Simulating the effect of sodium, calcium or NMDA block on 0 ms (coincident) integration in a model RS neuron with (orange) or without (blue) feedforward inhibition. (**B**) Simulating the effect of sodium, calcium or NMDA block on delayed (50 ms) integration in a model RS neuron with (orange) or without (blue) feedforward inhibition. Inset: schematic of channel and synapse distribution in model RS neurons. (**C**) The effect of pharmacological inhibition of sodium (low concentration (100 nM) of TTX), T-type calcium (Mib) and NMDA receptors (AP5) on coincident integration of ACC and AUD afferents in RS neurons in vitro. (**D**) The effect of the above pharmacological manipulations on delayed (50 ms) integration of ACC and AUD afferents in RS neurons in vitro. *: p < 0.05, paired t-test.

Subthreshold feedforward-feedback interactions translate to nonlinear action potential firing

I next asked whether the action potential output of IB and RS cells reflects the observed cell type-specific synaptic integration dynamics. To answer this question, I adjusted stimulus strength to elicit action potentials in unimodal trials with approximately 50% probability (Figure 22A and B). In interleaved trials, I activated ACC and AUD afferents either coincidentally, or with a 50, 100, or 250 ms delay, as described in our previous, subthreshold experiments (Figure 10D, E). I calculated a suprathreshold MEI by dividing the number of action potentials fired in response to the combined stimulation by the sum of unimodal action potentials. IB cells exhibited supra-additive action potential firing in response to coincident activation of ACC and AUD inputs (MEI = 1.56, p = 0.007, n = 11; t-test; Figure 22E). However, multimodal action potential firing in IB cells was indistinguishable from linear summation when the two inputs were delayed (50 ms: MEI = 1.19, p = 0.308; 100 ms: MEI = 1.11, p = 0.347; 250 ms: MEI = 1.10, p = 0.417; Figure 22E). In contrast, RS cell action potential

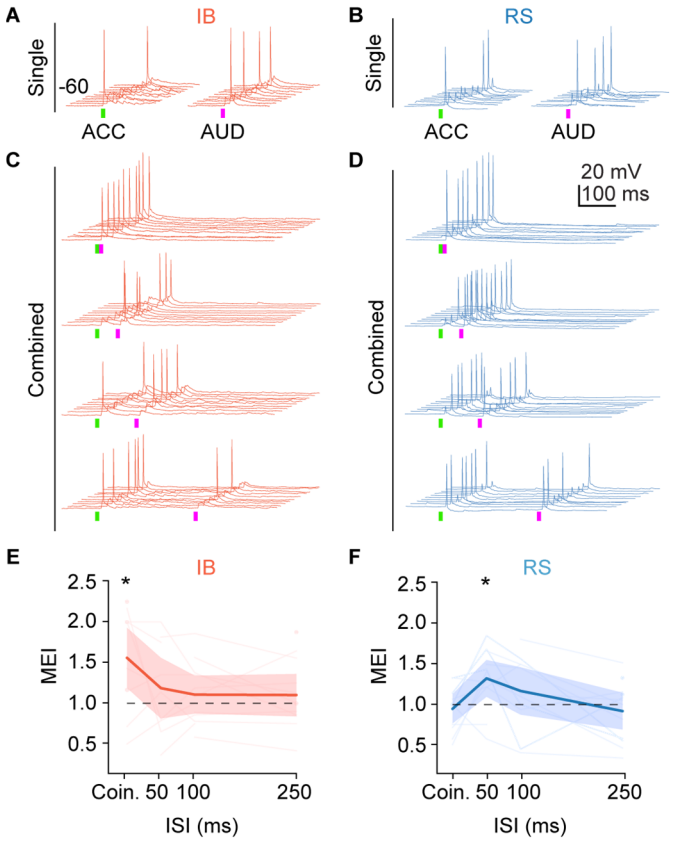

Figure 22. Temporal dynamics of action potential output mimic subthreshold feedforward-feedback integration dynamics. (**A**) Action potential firing of a IB cell (red) in response to unimodal (ACC or AUD) stimulation. (**B**) Unimodal firing responses in an RS cell (blue). (**C**) IB neuron (red) action potential firing in response to combined stimulation of ACC and AUD fibers with different delays. Same cell as in (A). (**D**) RS cell (blue) action potential firing in response to combined stimulation of ACC and AUD fibers with different delays. Same cell as in (B). (**E**) Temporal dynamics of suprathreshold ACC-AUD integration in IB neurons (light red lines). Dark red line represents population mean; shaded area represents 95% CI. (**F**) Temporal dynamics of suprathreshold ACC-AUD integration in RS cells (light blue lines). Dark blue line represents population mean; shaded area represents 95% CI. Dashed black line in (E) and (F) indicates linear integration. *: $p < 0.05$, t-test.

firing in response to coincident activation of ACC and AUD afferents was linear (MEI = 0.95, p = 0.539, n = 11; t-test, Figure 22F). Multimodal stimulation with 50 ms delay between inputs resulted in supra-additive action potential firing in RS neurons (MEI = 1.33, p = 0.011, n = 11; Figure 22F), while longer delays yielded linear integration (100 ms: MEI = 1.17, p = 0.248; 250 ms: MEI = 0.92, p = 0.457; Figure 22F). Multimodal integration profiles were significantly different between RS and IB neurons (cell type × synaptic delay interaction: $F_{3, 58} = 4.18$, p = 0.0096, two-way ANOVA). Thus, nonlinear enhancement of action potential firing in response to multimodal stimulation closely mirrored subthreshold synaptic integration in both IB and RS cells (compare Figure 10F and G to Figure 22E, F). These data suggests that the cell-type specific temporal dynamics of subthreshold integration shape the firing output of layer 5 pyramidal neurons in the PPC.

Nonlinear synaptic interactions are input-, synapse location-, and cell-type dependent

Finally, I sought to determine whether nonlinear multimodal enhancement in layer 5 pyramidal neurons of the PPC is a general feature of long-range afferent interactions or specific to the integration of ACC and AUD inputs. To answer this question, I first expressed ChR2 in the ACC and Chrimson in the visual cortex (VIS, Figure 23A), and measured ACC-VIS synaptic interaction as described above. In IB cells, coincident activation of ACC and VIS inputs resulted in a supralinear enhancement of EPSP amplitude (MEI = 1.30, p = 0.008, n = 7, t-test; Figure 23B), while delayed activation of the two afferents resulted in linear integration (50 ms: MEI = 0.96, p = 0.689; 100 ms: MEI = 1.08, p = 0.259; 250 ms: MEI = 0.95, p = 0.659; Figure 23B). In RS cells, ACC and VIS inputs summed linearly when activated coincidentally (MEI = 1.01, p = 0.841, n = 9; Figure 23C), while 50 and 100 ms delayed activation induced supralinear responses

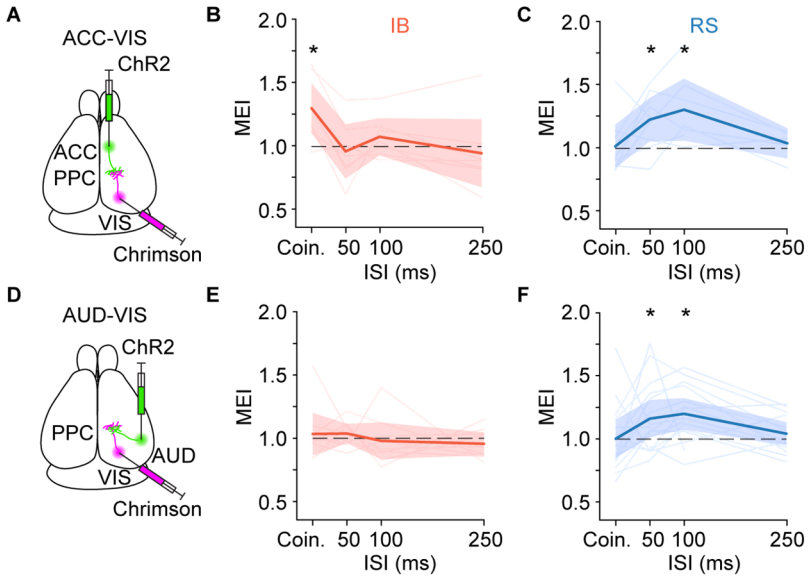

Figure 23. Input specificity of nonlinear synaptic interactions differs between IB and RS cells. (**A**) Schematic illustrating the transduction of ACC and VIS with ChR2 and Chrimson constructs, respectively. (**B**) Temporal dynamics of ACC-VIS integration in IB neurons (light red lines). Dark red line represents population mean; shaded area represents 95% CI. (**C**) Temporal dynamics of ACC-VIS integration in RS neurons (light blue lines). Dark red line represents population mean; shaded area represents 95% CI. (**D**) Schematic illustrating the transduction of AUD and VIS with opsin constructs. (**E**) Temporal dynamics of AUD-VIS integration in IB neurons (light red lines). Dark red line represents population mean; shaded area represents 95% CI. (**F**) Temporal dynamics of AUD-VIS integration in RS neurons (light blue lines). Dark red line represents population mean; shaded area represents 95% CI. Dashed black line in panels (B), (C), (E), and (F) indicates linear integration. *: $p < 0.05$, t-test

(50 ms: MEI = 1.23, p = 0.016; 100 ms: MEI = 1.31 p = 0.028; 250 ms: MEI = 1.04 p = 0.485; Figure 23C). Two-way ANOVA revealed that IB and RS cells have distinct temporal characteristics for ACC-VIS integration (cell type × synaptic delay interaction $F_{3, 36} = 9.72$, $p < 0.0001$). Comparison of ACC-AUD and ACC-VIS integration profiles indicated that frontal-sensory interaction dynamics are insensitive to the identity of the sensory input (input combination in IB cells: $F_{3, 42} = 0.076$, p = 0.97; in RS cells: $F_{3, 54} = 0.6173$, p = 0.61; two-way ANOVA). These results suggest that the cell-type specificity of nonlinear synaptic interactions may be a general feature of frontal-sensory integration in the PPC.

Next, I asked whether layer 5 pyramidal neurons in the PPC exhibit nonlinear integration of two sensory inputs. I expressed ChR2 in AUD and Chrimson in VIS afferents (Figure 23D) and measured their interaction as described above. In IB cells, activation of AUD and VIS inputs resulted in linear summation of both coincident (MEI = 1.04, p = 0.647, n = 9; t-test, Figure 23E)

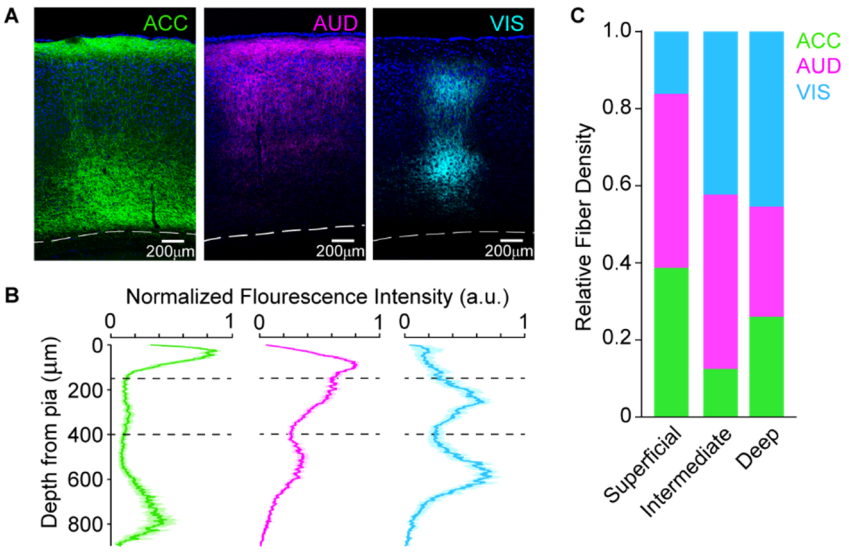

Figure 24. Distribution of feedforward and feedback afferents in PPC. (**A**) Example confocal images of ACC (green), AUD (magenta) and VIS (cyan) projections to the PPC. Blue: DAPI staining, scale bars are 200 µm. (**B**) Histograms showing the distribution (mean ± SEM) of ACC (green, n = 9), AUD (magenta, n = 16) and VIS (cyan, n = 7) fibers. (**C**) Relative density of ACC (green), AUD (magenta) and VIS (cyan) fibers in superficial (0-150 µm from the pial surface), intermediate (150-400 µm) and deep (400-800 µm) sections of the PPC cortical column.

and delayed inputs (50 ms: MEI = 1.04, p = 0.290; 100 ms: MEI = 0.98, p = 0.760; 250 ms: MEI = 0.96, p=0.302; Figure 23E). Comparing the temporal dynamics of frontal-sensory and sensory-sensory interactions indicated that in IB cells, nonlinear synaptic integration is specific to frontal-sensory input combinations (ACC-AUD$_{IB}$ vs. AUD-VIS$_{IB}$ × synaptic delay interaction $F_{3, 48} = 3.58$, p = 0.02; ACC-VIS$_{IB}$ vs. AUD-VIS$_{IB}$ × synaptic delay interaction $F_{3, 42} = 3.23$, p = 0.031, two-way ANOVA). In RS cells, coincident AUD and VIS inputs summed linearly (MEI = 1.00, p = 0.973, n = 15, t-test; Figure 23F) while inputs delayed by 50-100 ms showed enhancement (50 ms: MEI = 1.17, p = 0.034; 100 ms: MEI = 1.21, p = 0.004; 250 ms: MEI = 1.06, p = 0.339; Figure 23F). In contrast to IB cells, frontal-sensory integration profiles in RS neurons were indistinguishable from the sensory-sensory input combination (ACC-AUD$_{RS}$ vs. AUD-VIS$_{RS}$ × synaptic delay interaction $F_{3, 72} = 1.1$, p = 0.35; ACC-VIS$_{RS}$ vs. AUD-VIS$_{RS}$ × synaptic delay interaction $F_{3, 54} = 0.29$, p = 0.84, two-way ANOVA). These data suggest that RS cells integrate long-range inputs with a similar nonlinear profile while supralinear integration of coincident inputs by IB neurons is specific to feedforward-feedback input combinations.

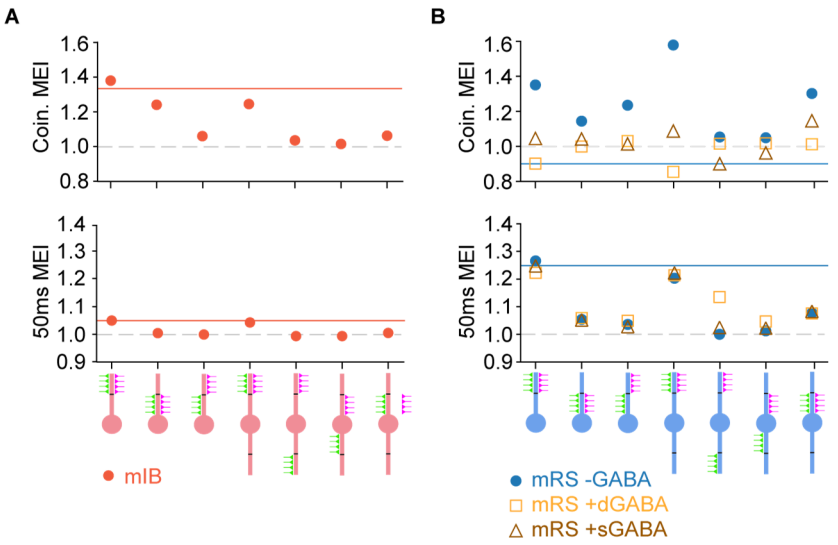

Figure 25. Synapse location plays a key role in nonlinear interactions. (**A**) Simulated synaptic integration performance of IB neuron models (red) across various anatomical configurations. (**B**) Simulated synaptic integration in RS neuron models without inhibition (-GABA, blue), with inhibition arriving at the same dendritic segment as excitation (+dGABA, yellow squares), or with somatic inhibition (+sGABA, brown triangles) across anatomical configurations. In panels (A) and (B), multimodal enhancement index (MEI) was measured for coincident (top) and delayed (50 ms, bottom) activation of excitatory inputs. Unimodal EPSP magnitudes were matched across model configurations.

These data indicated potential differences in how various feedforward and feedback inputs target distinct classes of PPC neurons. To examine this, I first determined the relative location of ACC, AUD and VIS axonal fibers in the PPC as a coarse measure of synapse distribution. I found that in general, all afferents were present throughout the cortical column, although their density varied greatly across the layers. Superficial layers of the PPC (0-150 mm from the pial surface) were enriched in fibers originating from the ACC and AUD (Figure 24). Intermediate layers (150-400 mm) showed high densities of AUD and VIS axons (Figure 24), while all three projections were present in deeper layers (400-800 mm, Figure 24).

To gain a more detailed insight into how synapse distribution may influence integration in IB and RS cells, Dr. Proddutur tested seven distinct model configurations for their permissiveness of multimodal enhancement. Synapse clustering was necessary for multimodal enhancement in both IB (Figure 25A) and RS (Figure 25B) models. When unimodal EPSPs, measured at the soma, were matched for amplitude, clustered synapses consistently produced larger MEI values then distributed synapses on otherwise identical model neurons. Furthermore, Dr. Proddutur observed larger nonlinearities, both coincident and delayed, when synapses

clustered on distal, rather than proximal dendrites (Figure 25). The location of inhibition had a minimal effect on multimodal enhancement in our models. In model RS cells, inhibition targeting either the soma or the excitatory recipient dendritic segment effectively suppressed coincident enhancement, with dendrite targeting inhibition exerting a slightly stronger effect in the majority of model configurations (Figure 25B).

Together, these data suggest that multimodal synaptic interactions are both cell type and input specific, and reinforce previous suggestions that clustering of afferent excitatory inputs is the most prominent driver of enhanced multimodal integration.

2.4 Discussion

In this Chapter I demonstrate that individual PPC neurons integrate feedforward and feedback synaptic inputs with cell-type specific, nonlinear temporal dynamics. I found that afferents originating from sensory and frontal cortical regions converged onto layer 5 pyramidal cells. Synaptic inputs from these two pathways summed supralinearly, with cell-type specific short-term dynamics. Subthreshold integration profiles translated to supralinear action potential firing in both neuronal populations. Mechanistically, my physiology data combined with computational modelling data collected by Dr. Archana Produttur suggest that an interaction of Na^{+}, Ca^{2+} and NMDA conductances support cell type specific integration profiles that is further shaped by differential inhibitory innervation.

Individual neurons integrate converging long-range afferent pathways

Multimodal interactions have been well documented in cortical circuits (Fritz et al., 2003; Li et al., 2004; McAdams and Maunsell, 1999; Moran and Desimone, 1985; Spitzer et al., 1988; Treue

and Trujillo, 1999), including between frontal-sensory (Zhang et al., 2014) and sensory-sensory (Meredith et al., 1987; Meredith and Stein, 1983; Olcese et al., 2013) neuronal pathways. Transsynaptic tracing experiments using rabies virus (Wall et al., 2010; Wickersham et al., 2007) suggested that long-range inputs conveying these modalities may co-terminate on individual cortical neurons (Kim et al., 2015; Vélez-Fort et al., 2014; Wall et al., 2016). Functional assessment of such synapses however, remained technically challenging. The strict anatomical structure of the hippocampus enabled the characterization of how single cells integrated multiple, identified input pathways at the synaptic level (Remy and Spruston, 2007; Takahashi and Magee, 2009). However, in the neocortex, only specialized preparations allowed for direct stimulation of long-range (e.g. thalamic) inputs (Agmon and Connors, 1991; Cruikshank et al., 2002). While electrical stimulation efforts facilitated the mapping of feedforward and feedback circuits in the visual system (Shao and Burkhalter, 1996), the inherent structural complexity of the neocortex (e.g. axons of passage) complicates the interpretation of such experiments. Focal stimulation methods, in combination with optogenetics, allowed the specific and independent activation identified afferents (Cruikshank et al., 2010; Petreanu et al., 2009; Yang et al., 2013) but until recently, this was restricted to a single pathway. Here, I circumvented these issues by using a dual color optogenetic approach (Klapoetke et al., 2014) to selectively manipulate multiple input pathways to the PPC. I show that a high proportion (~80%) of layer 5 pyramidal neurons receive monosynaptic dual innervation from frontal-sensory (ACC-AUD and ACC-VIS) and sensory-sensory (AUD-VIS) input combinations. This is in line with previous results indicating a high proportion of layer 5 PPC neurons producing multimodal responses (Olcese et al., 2013). Our data suggests that individual cortical neurons, at least in the PPC, are poised to integrate synaptic information from a diversity of long-range sources.

Multimodal enhancement of feedforward-feedback interactions

Two congruent sensory stimuli can produce action potential firing greater than predicted from the linear sum of unimodal responses. This has been shown in the superior colliculus as well as in cortical regions, including the PPC (Meredith et al., 1987; Meredith and Stein, 1983; Olcese et al., 2013). However, the synaptic events underlying multisensory enhancement and whether its principles could be extended to the interaction of non-sensory pathways remained unknown. I took advantage of the above detailed pathway convergence onto layer 5 pyramidal cells in the PPC, to determine how synaptic inputs from two distinct neuronal pathways interact. In our experiments, the majority of layer 5 pyramidal cells displayed supralinear integration of sensory and frontal inputs. However, I found marked differences between distinct neuronal populations: intrinsic burst firing (IB) neurons boosted coincident (0 ms synaptic delay) inputs while regular spiking (RS) cells preferentially enhanced synaptic events delayed by 50-100 ms. Action potential firing in response to multimodal stimuli followed the same cell-type specific nonlinear temporal dynamics as subthreshold inputs. These data suggest that nonlinear synaptic interactions at the single neuron level underlie the enhanced multimodal action potential firing observed by others *in vivo*. Furthermore, my findings indicate that principles of multisensory integration may be relevant to the interaction of afferent pathways other than sensory modalities.

An interaction of ionic and circuit mechanisms underlies synaptic integration profiles

The dendritic processes likely underlying nonlinear integration of synaptic inputs have been studied for decades (Magee, 2000; Stuart and Spruston, 2015). Multiple ionic mechanisms have been identified, including regenerative Na^{+}, Ca^{2+}, and NMDA currents (Ariav et al., 2003;

Golding et al., 1999, p. 199; Golding and Spruston, 1998; Kim and Connors, 1993; Larkum and Zhu, 2002; Losonczy and Magee, 2006; Polsky et al., 2004; Schiller et al., 2000, 1997). To determine what conductances drove supralinear synaptic integration at different time scales, we utilized a computational approach. Dr. Proddutur simulated multimodal integration at variable conductances, essentially producing 1881 distinct models, to explore a large parameter space (Marder and Taylor, 2011). Our model predicted that supralinear summation of coincident inputs was predominantly driven by Na^+ and Ca^{2+} conductances. The effect of NMDA receptor block on coincident inputs was likely due to an overall reduction of EPSP size and consequently diminished driving force, rather than a direct effect on synaptic summation. Conversely, the model revealed that supralinear integration of inputs delayed by 50 ms was co-dependent on Ca^{2+} channel conductance and NMDA receptor decay kinetics. The differential involvement of Na^+ and NMDA conductances in faster and slower integration, respectively, makes intuitive sense given the differences in channel kinetics (Almog et al., 2018; Milescu et al., 2010). However, it is important to note that efficient generation of supralinear integration relied on the interaction of multiple ionic mechanisms. These data urge caution in interpreting results from manipulating individual channels: nonlinear events may be diminished by disrupting such interactions, rather than by the specific removal of individual conductances.

While the initial group of models captured the integration characteristics of IB neurons, no combination of parameters reproduced the physiology of RS cells. This suggested that synaptic integration in RS neurons was influenced by an additional, non-cell autonomous mechanism. Previous work indicated that feedforward inhibition may control the temporal window for synaptic integration (Häusser and Clark, 1997; Naka and Adesnik, 2016) and consequently modulate multisensory interactions (Olcese et al., 2013). I found that inhibition

played a key role in suppressing coincident supralinear integration in RS cells. In an effort to isolate effects of feedforward inhibition, in a subset of experiments I included PTX in the patch pipette (Akaike et al., 1985; Atherton et al., 2016; Inomata et al., 1988; Metherate and Ashe, 1993). This method leaves other inhibitory signaling in the slice largely intact, although PTX leaking during microelectrode approach may still influence activity in the vicinity of the patched cell. Feedforward inhibition was markedly stronger in RS cells, corroborating recent findings by other groups (Hefti and Smith, 2000; Sun et al., 2013). Incorporating cell-type specific inhibition enabled computational models to capture RS cell integration characteristics. A likely candidate to mediate this feedforward inhibition are Parvalbumin expressing interneurons, which have been shown to receive strong input from long-range afferents (Anastasiades et al., 2018; Gibson et al., 1999; Li et al., 2014). However, the majority of our computational models favored dendrite targeting over perisomatic inhibition. Thus, the specific contribution of various interneuron species to multimodal integration remains a question for future work.

Cell type specific feedforward-feedback integration

Subclasses of layer 5 output neurons have been described in great detail in the past, with differences in anatomical, genetic, electrophysiological, and functional properties (Dembrow et al., 2010; Groh et al., 2010; Jacob et al., 2012; Kim et al., 2015; Lur et al., 2016; Oswald et al., 2013; Takahashi et al., 2020; Tang and Higley, 2020). Differential integration of long-range afferents adds a new aspect to the list of characteristics distinguishing layer 5 cortical neurons. I found two key differences with regards to multimodal integration.

First, IB and RS cells enhanced the interaction of feedforward and feedback inputs at different synaptic delays. Studies in human subjects and non-human primates found that

contextual modulation of sensory processing can occur immediately at response onset or following a 30-200 ms delay (Gilbert and Sigman, 2007; Lamme, 1995; Martínez et al., 1999; Vidyasagar, 1998). Our results offer a potential insight into the circuit mechanisms underlying early and late modulation: temporal differences may be reflecting the time scales at which distinct neuronal populations integrate the sensory stream with feedback inputs. How cell type-specific nonlinear integration influences multimodal cognitive processes like prediction error monitoring or multisensory binding is a question for future research.

Second, nonlinear integration in IB cells was selectively engaged by frontal-sensory and not sensory-sensory input combinations. In contrast, RS neurons displayed similar integration profiles regardless of input combination. Nonlinear interactions are thought to be most powerful when synaptic inputs are arranged within a dendritic branch and not separated by a bifurcation point (Polsky et al., 2004). One possibility is that auditory and visual afferents target distinct dendritic branches in IB cells, preventing cross-modal interactions of these inputs. Our modeling and anatomical data enables such configurations, although I remain agnostic about precise synaptic targeting, including a definitive distinction between basal or apical dendrites as long-range recipients. Differential layer-specific distribution of auditory and visual afferents was also observed, with AUD afferents primarily targeting layers 1 and 2/3, and VIS axons targeting layers 2/3, 4 and 5, consistent with publicly available datasets published by the Allen Institute for Brain Science ("Projection :: Allen Brain Atlas: Mouse Connectivity," n.d.). While the distribution of axons from VIS to PPC mirrors the canonical distribution of feedforward input observed in thalamocortical pathways to VIS and AUD, the AUD to PPC projection pattern more closely resembles that of primary projecting to secondary visual cortical regions (Galloni et al., 2022). These findings are consistent with the idea that PPC functions in lower-level capacity in

visual circuits but has a higher-level role in auditory processing. Layer distribution differences may also reflect precise anterior-posterior or medial-lateral positions sampled in this study, however this dimension of functional specialization was not examined here. Localization of synapses tuned to specific sensory features has been examined in the primary auditory (Chen et al., 2011) and primary visual cortices (Jia et al., 2010). However, how multimodal synapses are organized on the dendrites of cortical neurons remains an important future question (Larkum and Nevian, 2008).

CHAPTER 3

Differential persistent firing is a cell-autonomous property of projection-specific layer 5 pyramidal neuron types in the posterior parietal cortex

3.1 Introduction

Many core cognitive functions including attention, decision making, and working memory are characterized by sustained activity in the brain. In working memory tasks, delay periods are accompanied by persistent activity, most often observed in medial temporal lobe structures including hippocampus and entorhinal cortex (Nauer et al., 2015; Olsen et al., 2009; Schon et al., 2004), frontal cortex (Constantinidis et al., 2018; Funahashi et al., 1989; Guo et al., 2014; Inagaki et al., 2019; Yarkoni et al., 2005), and parietal cortex (Constantinidis and Steinmetz, 1996; Esmaeili et al., 2021; Machens et al., 2005; Todd and Marois, 2004; Yarkoni et al., 2005). This activity has been found to encode sensory variables (Goard et al., 2016; Musall et al., 2023; Rainer et al., 1998; Shadlen and Newsome, 2001), decision outcomes (Goard et al., 2016; Musall et al., 2023), and motor intent (Guo et al., 2014; Shadlen and Newsome, 2001). In preliminary experiments, I used dual-color optogenetics (Chapter 1) to stimulate feedback afferents from the anterior cingulate cortex (ACC), together with feedforward afferents from auditory cortex (AUD), in the mouse posterior parietal cortex (PPC) in acute brain slices. Using an extracellular multi-unit electrode to record neural spiking activity from large populations of PPC neurons in layer 5 (L5) (Figure 26A), these preliminary experiments revealed that the co-activation ACC and AUD synaptic inputs triggered long-lasting persistent activity in the PPC (Figure 26B–D). Repeating this experiment by recording single cell responses while stimulating ACC afferents

together with visual cortex (VIS) axons (Figure 26E), I found that underlying this sustained local circuit activity is persistent firing in individual L5 neurons. These data hint at a potential mechanism that facilitates context-dependent short storage of sensory information in PPC microcircuits. Nevertheless, a large range of *in vivo* spiking behaviors have been reported during task delay periods. Cells active only during delay periods are often found, which become quiescent after a behavioral response is made (Goard et al., 2016; Guo et al., 2014). Others appear to ramp their activity during the delay, and peak after the response (Goard et al., 2016; Guo et al., 2014). In addition, a separate population of cells are selectively suppressed during the delay phase (Goard et al., 2016). This diversity of delay period activity patterns suggests the existence of unique neuronal populations with distinct roles in working memory.

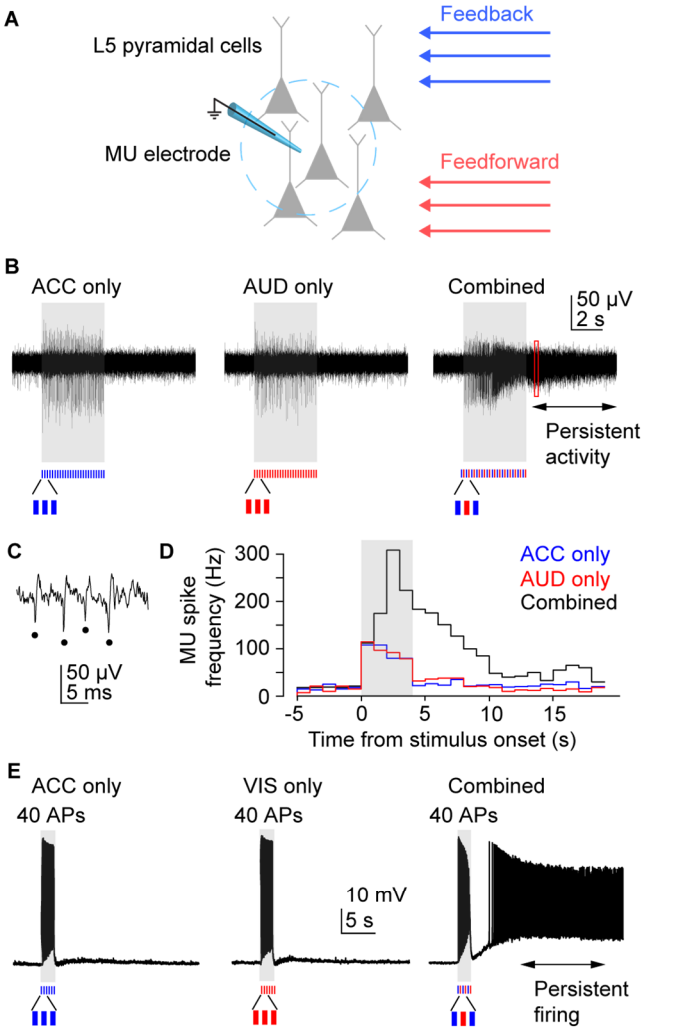

Figure 26. Feedforward-feedback integration triggers persistent firing in the PPC. (**A**) Schematic of multiunit recording of neural activity. (**B**) Multiunit activity (MUA) recorded in PPC layer 5 in response to unimodal AUD, ACC, and combined AUD-ACC stimulation. (**C**) Zoomed in MUA from red boxed region in (C). Dots indicate spikes identified via in-house spike sorting algorithm. (**D**) Histogram of MU spike frequencies. Shaded region indicates stimulus period. Combined stimulation leads to activity which persists beyond stimulus offset. (**E**) Single cell response to ACC, VIS, and interleaved ACC-VIS inputs at 20 Hz for 2 s. Stimulation induces precisely 40 action potentials (APs) in each, yet triggers persistent firing when inputs are combined.

Cortical L5 neurons are considered the primary "output" neurons of cortex, which project to either other cortical areas and striatum (intratelencephalic, or "IT" subtype) or primarily to brainstem structures outside of the telencephalon (pyramidal tract, or "PT" subtype, also known as extratelencephalic, or "ET" cells) (Dembrow et al., 2015, 2010; Hattox and Nelson, 2007; Kim et al., 2015). In addition to established differences in function of IT and PT neurons for triggering behavior (Garcia et al., 2021; Tang and Higley, 2020), recent evidence suggests that these cortical cell types may also play distinct roles in working memory (Bae et al., 2021; Musall et al., 2023). In a remarkable study, Musall et al. 2023 used widefield calcium imaging in mice with genetically labelled IT and PT neurons, in theory sampling activity of these cell types across the entire cortical surface (Musall et al., 2023). Training mice in an auditory delayed decision task, authors show that PT, rather than IT, neurons are preferentially active during delays in both frontal cortex and the PPC. Selective optogenetic inhibition furthermore revealed important contributions of each cell type to task performance. Inhibition of frontal areas showed marked behavioral impairment when targeting IT and PT cells during delay periods (however, note opposite results were obtained in (Bae et al., 2021)). In contrast, in the PPC, inhibiting PT, but not IT, neurons during delay periods negatively impacted the animal's ability to perform the task (Musall et al., 2023). While limited, these findings suggest that PT neurons, at least in PPC, may have a specialized role in storing behaviorally-relevant information in their spiking activity during working memory delays.

Two competing hypotheses exist for the precise mechanism underlying persistent firing – reverberatory activity in recurrent neural circuits and activation of intrinsic ionic conductances. Computational models of persistent firing in cortex repeatedly demonstrate that even small numbers (<10) of interconnected neuron-like nodes can recapitulate dynamic delay-period

spiking activity recorded *in vivo* (Compte et al., 2000; Papoutsi et al., 2013; Wang, 1999). However, the importance of recurrently-connected excitatory cells for persistent activity in cortex has been difficult to address experimentally. In theory, such a claim would require correctly inferring the directional flow of excitation through the circuit from binary measures of spike activity, often from individual or small groups of cells. Furthermore, results from *in vivo* attempts (Vugt et al., 2020) to manipulate glutamatergic synaptic transmission during working memory are difficult to interpret since manipulations will block local reverberatory circuit dynamics in addition to long-range input presumed to drive persistent firing. Nevertheless, many differences in IT and PT local connectivity may explain functional differences observed in working memory paradigms. IT and PT cells are highly connected to cells within their own subtype, however only IT cells cross-innervate PT (Brown and Hestrin, 2009; Kiritani et al., 2012; Lefort et al., 2009), suggesting unidirectional information flow in L5 circuits. PT neurons also appear to have a higher likelihood of receiving same-subtype reciprocal input than IT (Morishima et al., 2011). Furthermore, resting state noise correlations in V1 revealed that while PT activity is as correlated with other PT as non-PT cells, IT neuron calcium activity is more strongly correlated with activity of other IT than non-IT cells (Lur et al., 2016), results which were since reproduced by other groups (Musall et al., 2023). These data indicate the presence of distinct subnetworks within L5, which may influence the behavior of each cell type during periods of sustained activity.

In tandem, several cell-autonomous mechanisms of persistent firing have been described in acute brain slices. Since early demonstrations of persistent firing in entorhinal cortex slices (Egorov et al., 2002), persistent firing has also been shown in prefrontal (Thuault et al., 2013), perirhinal (Navaroli et al., 2012), and somatosensory cortex (Rahman and Berger, 2011), and

non-cortical regions including the olfactory bulb (Shpak et al., 2012). Many of these studies include glutamatergic receptor antagonists to block excitatory synaptic transmission, yet still report the presence of persistent firing, indicating that cells are also capable of maintaining their own firing after brief periods of excitation. Underlying persistent firing in slices is a slow afterdepolarization (sADP), proposed to result from either activation of a slow-inactivating calcium-activated nonspecific cation (CAN) current (Haj-Dahmane and Andrade, 1998; Pressler and Strowbridge, 2006; Rahman and Berger, 2011) or a transient rise in input resistance caused by suppression of a leak potassium conductance (Constanti et al., 1993; Constanti and Bagetta, 1991; Cui et al., 2022; Cui and Strowbridge, 2018), both mechanisms which initially rely on the accumulation of intracellular calcium. Indeed, persistent firing *in vivo* likely results from a dynamic interplay between synaptic weight changes, reverberating network activity, and intrinsic membrane currents (Marder et al., 1996), which may all influence the behavior of IT and PT neurons during working memory.

My preliminary data suggests that L5 persistent firing is strongly driven by the integration of feedforward and feedback synaptic input (Figure 26). However, whether the combined synaptic stimulus is triggering self-sustained firing across large populations of cells, or network-dependent excitatory reverberations is unclear. Furthermore, the role of distinct subtypes of PPC neurons in sustaining this activity is unknown. I took a reductionist approach to this question and chose to first test persistent firing mechanisms in single cells via whole-cell patch clamp. I mimicked synaptic stimuli used in Figure 26 by directly injecting short trains of depolarizing current steps at the same frequency as used in preliminary optogenetic experiments. This stimulus paradigm selectively activates only the patched cell, and thus allows disambiguating cell-autonomous and network-dependent mechanisms of persistent firing. In line

with previous reports on persistent firing in other brain regions in slice (Egorov et al., 2002; Navaroli et al., 2012; Rahman and Berger, 2011; Shpak et al., 2012; Thuault et al., 2013), persistent firing could be induced via single cell activation in PPC preparations. Interestingly, persistent firing evoked in PT neurons was significantly longer, and exhibited higher spike frequencies, than in IT. Pharmacological inhibition of ionotropic glutamate receptors had no effect on persistent firing durations in either cell type. Furthermore, the frequency of spontaneous EPSCs did not change after stimulation, indicating the absence (or at minimum, non-activation) of a recurrent excitatory circuit. Persistent firing was also accompanied by long-lasting increase in intracellular calcium levels, which were notably absent in nearby cells. Lastly, I found differences in L5 subtype intrinsic properties which may explain differences in PT and IT persistent firing. These data suggest that persistent firing driven by feedforward-feedback integration in PPC is largely maintained by cell-autonomous mechanisms which favor long-lasting firing in PT over IT subtypes.

3.2 Methods

Animals

All animal experiments were approved by the Institutional Animal Care and Use Committee and performed in accordance with the NIH guidelines on the care and use of laboratory animals. C57BL/6J mice were group-housed in a quiet, uncrowded facility on a 12 h light/dark cycle, with *ad libitum* access to lab chow and water. No differences were detected between sexes thus data were pooled.

Retrograde labelling of IT and PT neuron subtypes

Transcranial injections were performed as described in Chapter 1. To label IT and PT neurons for use in physiology experiments, as in Chapter 2 I injected 555 nm Alexa Fluor-conjugated cholera toxin subunit B (CTB, ThermoFisher) into the ipsilateral dorsal Striatum (dStr, 350 nl, AP: 0.85, ML: 1.5, DV: 2.0 in mm from Bregma) or into the ipsilateral Pons (500 nl, AP: -4.1, ML: 0.8, DV: 5.5 in mm from Bregma) in separate animals. A minimum of 1 week was allowed for retrograde transport before physiology experiments.

Electrophysiology

Brain slices containing PPC were prepared as described in Chapter 1, however were sectioned at 400 μm to preserve a maximum portion of local synaptic connections. Animals were P51-71. Recordings were performed at close to physiological temperature (32-34 °C) from fluorescently labelled cells identified using an X-Cite mercury lamp (Excelitas Technologies). Intracellular recording solutions were identical to that in Chapters 1 and 2. The extracellular bath solution used for recording persistent firing was a modified low-calcium ACSF solution comprised of (in mM): 126 NaCl, 25 $NaHCO_3$, 10 Glucose, 3.5 KCl, 1.2 $CaCl_2$, 1.25 NaH_2PO_4, and 1 $MgSO_4$. The cholinergic receptor agonist carbamoylcholine chloride (carbachol, Tocris, 10 μM) was included in the bath solution in all persistent firing experiments. In select experiments, glutamatergic receptor antagonists 2-amino-5-phosphonopentanoic acid (AP5, Tocris, 50 μM) and 2,3-dioxo-6-nitro-7-sulfamoyl-benzo[f]quinoxaline (NBQX, Tocris, 10 μM) were added. Slices were allowed to incubate in ACSF containing agonists or antagonists for a minimum of 15 minutes before all recordings. Persistent firing was triggered from a pre-stimulus potential of -60 mV, using a 20 Hz train of 10 ms +350 pA pulses of variable duration (0.5 – 4 s). EPSC

recordings were recorded in voltage clamp with a holding potential of -70mV. Following 30 seconds of baseline recording, a second recording instance was initiated in current clamp, and the membrane potential gradually brought to -60 mV, after which a 0.5 or 2.0 s train stimulus (as above) was applied. Immediately following cessation of the stimuli, the amplifier was manually set back to voltage clamp mode to record post-stimulus EPSCs. Extracellular multiunit recordings used in collecting preliminary data in Figure 3 were performed with a broken glass electrode filled with ACSF which yielded pipette resistances 0.3–0.8 MΩ. 3–5 minutes were left between persistent firing trials to allow intracellular processes and network dynamics to recover during which cells were held at -70 mV. Signals were amplified using a MultiClamp 700B amplifier (Molecular Devices). Data were sampled at 10 kHz, filtered at 4 kHz, and digitized on National Instruments DAQ boards. WaveSurfer software written in Matlab (HHMI Janelia Research Campus) was used for data acquisition. Offline analysis was performed using custom routines in Python 3.7

Calcium imaging

To induce jGCaMP8m expression, I injected the PPC (300 nl, AP: 2.5, ML: 1.7, DV: 0.5 in mm from Bregma) of mice in the same surgical session as injection of retrograde tracers. Adeno-associated viral vectors containing jGCaMP8m were purchased from Addgene, AAV9-hSyn-jGCaMP8m-WPRE (Addgene #162375) and injected at 2.0 x 10^{12} dilution. Slices were collected as described in *Electrophysiology* above. A blue (440 nm) LED (Sutter Instruments) mounted directly to the microscope was used to deliver light through a 20x water immersion objective (Olympus, Japan) to excite jGCaMP8m. A minimal light intensity was used to avoid photobleaching. Images were captured using a QIClick CCD camera (Q Imaging) synced to

electrophysiological measurements via a 5V trigger signal of 10 ms generated by National Instruments DAQ boards at 14 Hz. Fluorescence intensity was measured using ImageJ.

Statistical analysis

All statistical analysis was performed in Prism 9 (GraphPad, La Jolla CA). EPSC detection was performed on an in-house event detection program ("MiniAnalysis") written in MATLAB (MathWorks). The 30 second period immediately post-stimulus was used to compare average EPSC frequencies and amplitudes with baseline.

3.3 Results

Cell-type-specific induction of persistent firing

I first sought to test the propensity of PPC layer 5 neurons to enter a persistent firing regime following direct activation of individual cells. PT and IT subtypes were retrogradely labelled by injecting cholera toxin B-subunit (CTB) conjugated with a red fluorophore in ipsilateral dorsal striatum (dStr) or pons, respectively, in separate animals. Retrogradely labelled PT and IT cells largely map on IB and RS cell types recorded in Chapter 2 (Figure 20). I used whole-cell patch clamp to record firing responses of labelled cells in acute brain slices following direct activation via a 40 Hz depolarizing train of 10 ms current steps delivered through the recording pipette (see *Methods*). This stimulus triggered a precise and equal frequency of action potentials in PT and IT neurons, resulting only rarely in spike doublets. To facilitate persistent firing, the cholinergic agonist carbachol (CCh, 10 μM) was included in all bath solutions. In 52.7% (48/91) of all recorded cells, depolarizing current trains (0.5s–4s) triggered persistent firing outlasting the stimulus (Figure 27A). The proportion of neurons which displayed persistent firing did not differ

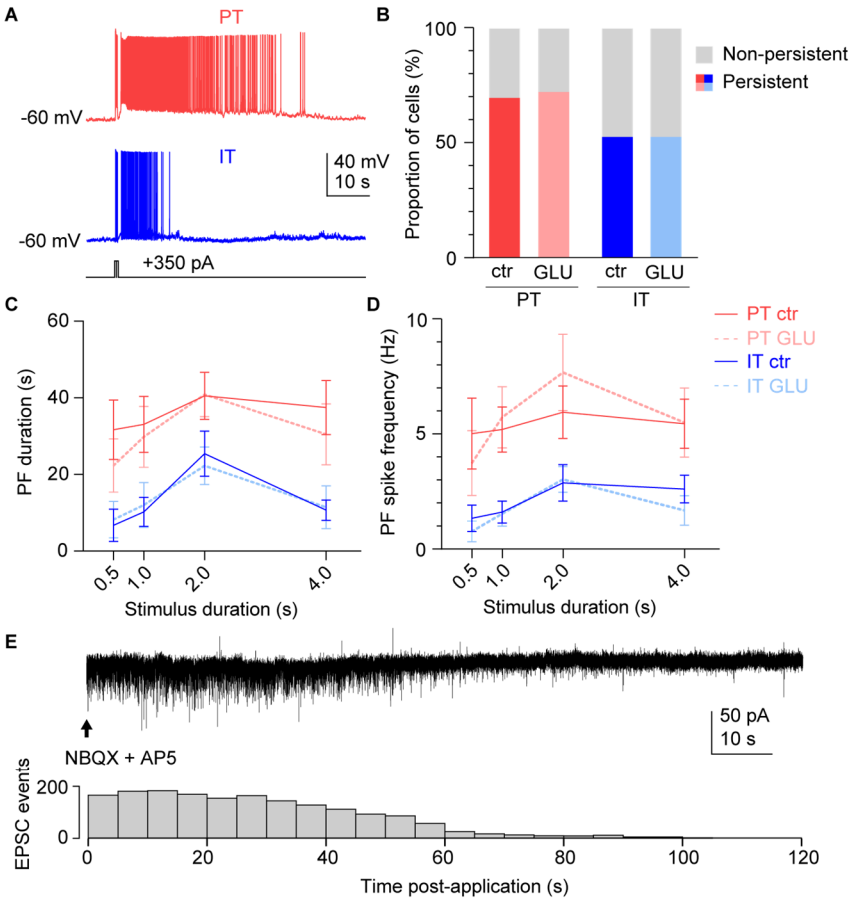

Figure 27. Differential persistent firing in PT and IT neurons in PPC. (**A**) Representative traces of persistent firing induced in PT (red) or IT (blue) neurons. (**B**) Proportion of all recorded neurons that displayed either non-persistent or persistent firing phenotypes. (**C**) Persistent firing (PF) duration as a function of triggering stimulus duration. $n_{PT\ ctr}$ = 12 mice, $n_{IT\ ctr}$ = 13, $n_{PT\ GLU}$ = 10 mice, $n_{IT\ GLU}$ = 10. (**D**) Average spike frequency during persistent firing as a function of stimulus duration. Data used in are same as in (C), and thus n numbers are same. In (C) and (D), solid lines represent recordings in control ACSF. Dotted lines represent recordings in ACSF with glutamate (GLU) receptor antagonists NBQX and AP5. Error bars represent s.e.m.. (**E**) EPSCs recorded from a PT neuron immediately following spiking ACSF solutions with NBQX and AP5 (top). Histogram of detected EPSC events (bottom).

between PT and IT cells (PT 30/43, IT 29/55 cells, $p = 0.100$, Fisher's test; Figure 27B). By varying the stimulus duration, I established dose-response curves of the length (Figure 27C) and spike frequency (Figure 27D) of persistent firing. Interestingly, PT neurons had overall larger persistent firing responses than IT across the range of stimuli tested (duration, cell type effect: $F_{1, 75} = 28.87$, $p < 0.001$; frequency, cell type effect: $F_{1, 23} = 12.41$, $p = 0.002$, two-way ANOVA; Figure 27C and D).

Persistent firing in PT and IT neurons driven by non-network-dependent mechanisms

To test the possible involvement of recurrent synaptic connections for sustained neural firing, I next repeated persistent firing induction protocols in the presence of bath glutamatergic receptor antagonists, NBQX (10 μM) and AP5 (50 μM) (GLU). Blocking glutamatergic synaptic

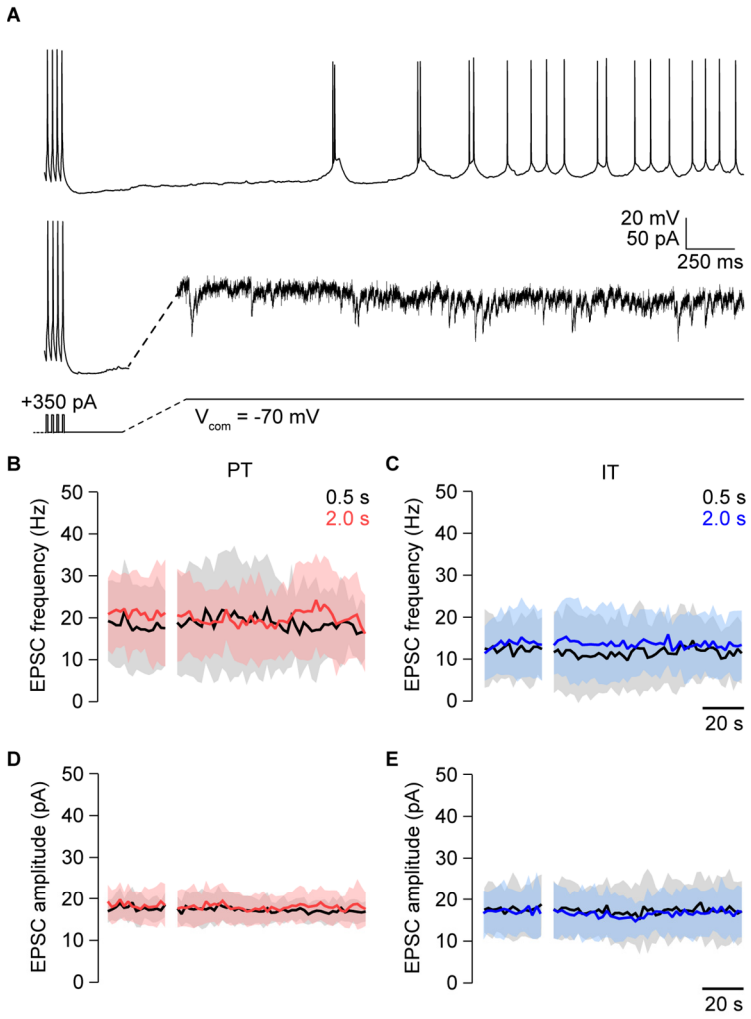

Figure 28. PT and IT neurons do not engage local excitatory recurrent circuits. (**A**) Example traces from the same cell showing persistent firing (top), and manual transition between current and voltage clamp modes (bottom) during tests of cell-triggered changes in network activity. (**B**) EPSC frequency during baseline and following single PT neuron stimulation for 0.5 (black, n = 8 cells) or 2.0 s (red, n = 7). Empty interval depicts stimulus period where amplifer was in current clamp. (**C**) EPSC freqency during baseline and following single IT neuron stimulation for 0.5 (black, n = 8) or 2.0 s (blue, n = 7). (**D**) EPSC amplitude during baseline and following single PT neuron stimulation. Data is taken from samerecordings as used in (B) and (C), thus n numbers are same. (**E**) EPSC amplitude during baseline and following single IT neuron stimulation. In (B-E), dark lines represent means. Shaded regions display s.e.m.

transmission had no effect on persistent firing in PT (duration, GLU effect: $F_{1, 20} = 0.674$, p = 0.421; frequency, drug effect: $F_{1, 20} = 0.015$, p = 0.903, two-way ANOVA; Figure 27C and D) or IT (duration, GLU effect: $F_{1, 21}$ =0.045, p = 0.834; frequency, GLU effect: $F_{1, 21} = 0.436$, p = 0.401, two-way ANOVA; Figure 27C and D) cells. The differential sensitivity of IT and PT neurons to triggering stimuli also remained intact in the presence of NBQX and AP5 (duration, cell type effect: $F_{1, 18} = 6.174$, p < 0.023; frequency, cell type effect: $F_{1, 18} = 9.432$, p = 0.007, two-way ANOVA; Figure 27C and D). The proportion of cells which triggered persistent firing was not different in ctr or GLU (PT, 30/43 vs. 21/29, p > 0.999; IT 29/55 vs. 19/36 cells, p > 0.999; ctr vs. GLU; Fisher's test; Figure 27B). One possibility is that our NBQX and AP5 drug cocktail is ineffective at suppressing synaptic responses. However, the frequency of spontaneous EPSCs decreased substantially within 2

minutes of spiking bath solutions, indicating that our drug manipulation is successfully blocking glutamatergic synaptic transmission (Figure 27E). To directly test whether activity of PT or IT cells triggers recurrent excitatory response, I next recorded EPSCs during a 30 second baseline shortly prior to stimulation and immediately following a 0.5 or 2.0 s stimulus (Figure 28A, see *Methods*). All cells where EPSCs were recorded were first tested to confirm they trigger persistent firing (Figure 28A). I observed equal frequency of EPSCs before and after stimulation in both PT (0.5 s, $p = 0.548$, $n = 7$; 2 s, $p = 0.570$; $n = 8$ cells; paired t test; see *Methods*; Figure 28B) and IT (0.5 s, $p = 0.235$, $n = 7$; 2 s, $p = 0.678$; $n = 8$ cells; Figure 28C) cells. EPSC amplitudes were also unaffected by PT (0.5 s, $p = 0.975$, $n = 7$; 2 s, $p = 0.693$; $n = 8$ cells; paired t test; Figure 28D) or IT (0.5 s, $p = 0.410$, $n = 7$; 2 s, $p = 0.275$; $n = 8$; Figure 28E) stimulation. Together, these results suggest that recurrent synaptic excitation does not contribute to persistent firing in IT or PT neurons, and that differences in firing responses between neuron subpopulations are driven by cell-autonomous mechanisms intrinsic to each projection cell-type.

Cell-autonomous mechanisms of persistent firing

Pharmacological studies blocking voltage gated calcium channels (VGCCs) or increasing intracellular calcium buffering have repeatedly shown that persistent firing is highly dependent on intracellular calcium signaling (Egorov et al., 2002; Fransén et al., 2006; Haj-Dahmane and Andrade, 1998; Hofmann and Frazier, 2010; Navaroli et al., 2012; Rahman and Berger, 2011). I thus next examined calcium dynamics in L5 neurons following persistent activity generation. Data from one animal is shown in Figure 29. I expressed the genetically encoded calcium sensor jGCaMP8m (Zhang et al., 2023) in PPC via an adeno-associated viral vector (Figure 29A, see *Methods*). In the same animal, PT neurons were labelled via CTB injection in pons as in previous

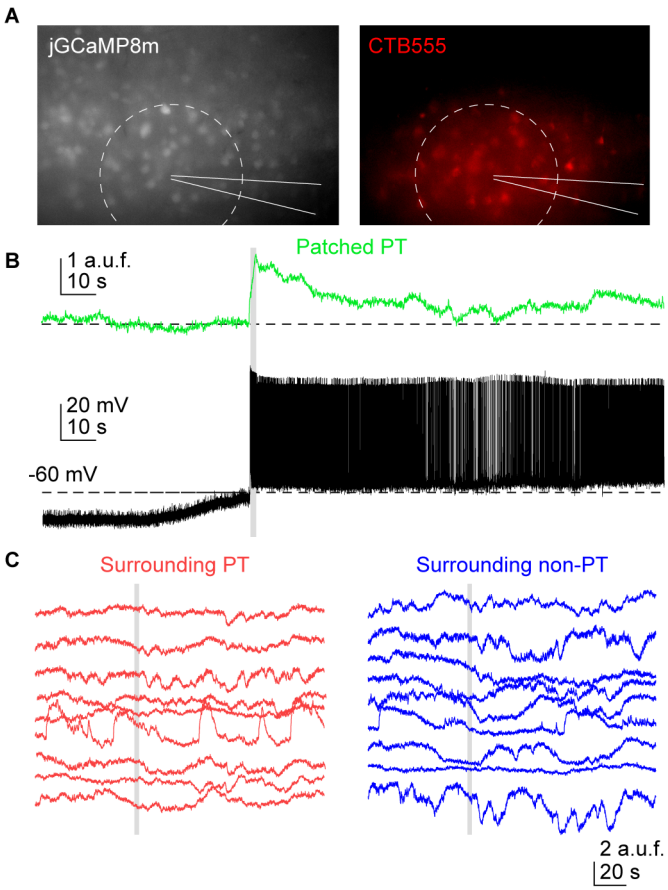

Figure 29. Persistent activity is associated with long-lasting increases in intracellular calcium. (**A**) Example image of layer 5 neurons in PPC actue slices expressing the intracellular calcium sensor jGCaMP8m (left), and CTB555 retrogradely labelled PT neurons (right). Solid lines indicate the position of the intracellular recording electrode. Dashed line indicates boundary used to constrain neurons being displayed in (C). (**B**) jGCaMP8m fluorescence signal (top, green) of a patched PT neuron during induction of persistent activity, with simultaneously recorded voltage trace (below, black). a.u.f., arbitrary unit of fluorescence. Dotted line in fluorescence trace represents a baseline level. Dotted line in voltage trace indicates -60 mV. Grey shaded region is stimulus period. Voltage trace is contaminated by approximately 5 mV step noise at 14 Hz, contributed by the fluorescence camera trigger. (**C**) jGCaMP8m fluorescence signals from 9 PT (red) and 9 non-PT (blue) neurons adjacent to the stimulated PT cell in (B). Each trace was collected from a single neuron during the same imaging session as (B).Grey shaded region represents the stimulus period.

experiments. I then prepared jGCaMP8m-expressing PPC acute slices, and simultaneously recorded both calcium signals from local neurons (see *Methods*) and the membrane potential of a single PT cell using whole-cell patch clamp. Persistent firing was induced using the same 40 Hz step stimulus as in Figure 27. Calcium-related fluorescence in the patched neuron was largely stable during pre-stimulus periods when the membrane potential was forcibly held under -60 mV (Figure 29B). However, the triggering stimulus induced a rapid increase in calcium signal which remained above baseline levels throughout the persistent firing period (Figure 29B). Visual examination of fluorescence traces from PT, and non-PT neurons in the vicinity of the patched cell indicate that this rise in intracellular calcium is restricted to the cell being electrically stimulated (Figure 29C), providing further evidence that single neuron-induced persistent firing is independent of activity in the local network. These data suggest that persistent

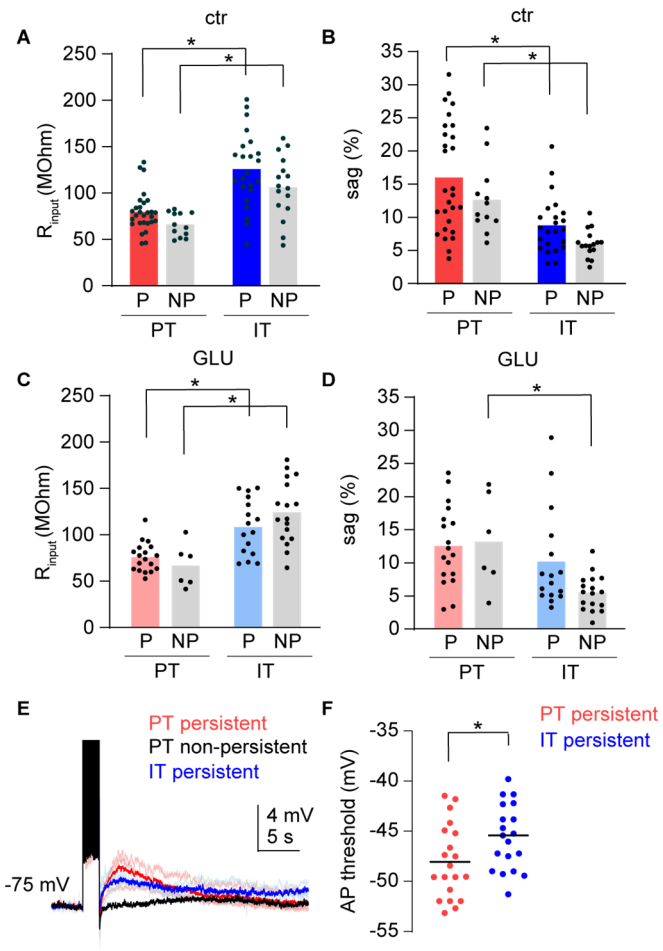

Figure 30. Potential mechanisms for cell-type-secific persistent firing. (**A**) Input resistance of PT and IT neurons which were either persistently firing (P, red and blue) or non-persistently firing (NP, grey) in control ACSF. Bars represent means, each dot is a single experimental replicate (PT: P, n = 28 cells, NP, n = 12; IT: P, n = 23, NP, n = 16). *: $p < 0.05$, one-way ANOVA with Sidak's correction for multiple comparisons. (**B**) Percent sag of PT and IT neurons in control ACSF. Recordings are same as (A), thus cell numbers are equal. (**C**) Input resistance of PT and IT neurons in ACSF containing glutamate blockers NBQX and AP5 (GLU) (PT: P, n = 18 cells, NP, n = 6; IT: P, n = 16, NP, n = 17). (**D**) Sag of PT and IT neurons in GLU block conditions. Recordings are same as (C), thus cell numbers are equal. (**E**) Persistent firing train stimuli applied from -75 mV to avoid post-stimulus spiking revealed a slow afterdepolarization (sADP). Stimulus period action potentials truncated. Traces from individual neurons in light shaded colors (PT, light red: n = 3; PT, grey: n = 1; IT, light blue: n = 3). Dark lines represent means. (**F**) Action potential threshold in persistently firing PT and IT neurons, recorded from spikes fired during persistent firing periods (PT, n = 20 cells; IT, n = 19; p = 0.033; t-test).

firing is associated with long-lasting increases in intracellular calcium which may drive sustained responses to short, depolarizing stimuli.

While a majority of L5 neurons are capable of persistently firing, a large fraction appears not (Figure 27B). I thus next sought to examine cell-intrinsic properties of L5 neurons which may explain the difference in these response properties. The input resistance of L5 neurons differed between PT and IT subtypes, however no differences were observed between cells within a subtype either capable (persistently firing, "P") or incapable (non-persistently firing, "NP") of firing persistently (PT vs. IT: P $p = 0.003$, NP $p < 0.001$; P vs. NP: PT $p = 0.556$, IT $p = 0.175$; PT_P n = 28 cells, PT_{NP} n = 12, IT_P n = 23, IT_{NP} n = 16; one-way ANOVA with Sidak's correction for multiple comparisons; Figure 30A). Similarly, the sag potential percentage of L5 neurons differed between PT and IT neurons, however sag between persistently and non-persistently firing cells within a subpopulation was identical (PT vs.

IT: P $p < 0.001$, NP $p < 0.017$; P vs. NP: PT $p = 0.329$, IT $p = 0.481$; one-way ANOVA with Sidak's correction for multiple comparisons; Figure 30B). To rule out the possibility of compensatory changes in intrinsic properties developing during incubation periods which mask effects of blocking excitatory synaptic transmission, I also examined input resistance and sag properties in the presence of glutamate blockers. The addition of NBQX and AP5 did not change input resistance relationships (PT vs. IT: P $p = 0.003$, NP $p < 0.001$; P vs. NP: PT $p = 0.936$, IT $p = 0.346$; PT_P n = 18 cells, PT_{NP} n = 6, IT_P n = 16, IT_{NP} n = 17; Figure 30C), and only minimally affected sag (PT vs. IT: P $p = 0.003$, NP $p < 0.001$; P vs. NP: PT $p = 0.556$, IT $p = 0.175$; Figure 30D), thereby excluding this possibility. Underlying persistent firing is a slow afterdepolarization potential (sADP), which can be revealed from lower resting membrane potentials. Holding cells at -75 mV, I next observed the amplitude of the sADP which develops after 2 second stimulation in persistently firing PT, IT and non-persistently firing PT cells (Figure 30E). While cell numbers are limited (PT_P, n = 3; IT_P n = 3; PT_{NP}, n = 1), persistently firing PT neurons appear to have larger sADPs than IT neurons, consistent with previous findings in the PFC (Dembrow et al., 2010). Notably, the sADP was largely absent in the non-persistently firing PT cell (Figure 30E). These data suggest that currents underlying the sADP play a causal role in determining the propensity of L5 cells to engage in sustained activity. Lastly, I measured the action potential (AP) threshold of spikes fired during persistent firing. Interestingly, PT neuron spike thresholds were also significantly lower than IT (PT, -45.58 ± 0.75 mV, n = 20, IT, -48.05 ± 0.82 mV, n = 19; $p = 0.033$; t-test; Figure 30F). Together, these data suggest that the combination of large sADP and hyperpolarized spike thresholds position PT neurons to be preferentially engaged during periods of persistent firing.

3.4 Discussion

Persistent firing in cortical circuits is presumed to reflect online storage of behaviorally relevant information during working memory. Integration of feedforward and feedback information is crucial for this process, yet evidence of interactions between these pathways generating persistent activity in cortex is limited. In a series of preliminary experiments, I demonstrated that co-activation of feedforward (AUD) and feedback (ACC) afferents was necessary to trigger persistent firing in L5 of the PPC (Figure 26). This result was in line with findings I describe in Chapter 2 that L5 neurons nonlinearly integrate synaptic input from ACC and AUD pathways. However, whether nonlinear integration in L5 cells triggers persistent firing by activating a local recurrent network or rather by engaging a cell-autonomous process is unclear. In this Chapter, I demonstrate that persistent firing of PT and IT neurons in PPC slices is independent of local network activity, through inhibition of glutamatergic synaptic transmission and direct observation of recurrent excitation. Thus, my working model of integration-induced increases in persistent firing is as follows. Nonlinear integration of synaptic input from feedforward and feedback pathways leads to increased spiking in L5 neurons (Figure 22, Chapter 2). This increase in firing more effectively engages a so far undescribed cell-autonomous trigger mechanism, leading to longer-lasting persistent firing (Egorov et al., 2002). This model implies that input timing is critical to persistent firing, given known differences in the selectivity of PT and IT cells to specific input frequencies (Rindner et al., 2022) (Chapter 2). Follow-up experiments may test this model by repeating initial integration experiments (Figure 26) while directly recording PT or IT cell activity. Optogenetic activation of ACC and AUD pathways at different timings is expected to trigger persistent firing more effectively in PT if stimuli are coincident, or IT if stimuli are delayed.

What are the ionic mechanisms of persistent firing? Cholinergic signaling is an essential aspect of attention and working memory (Anagnostaras et al., 2003; Granon et al., 1995; Spencer et al., 1985). During periods of heightened attention, acetylcholine released (Kametani and Kawamura, 1990; Marrosu et al., 1995) in target regions binds to both nicotinic and muscarinic acetylcholine receptors (mAChRs), the latter of which triggers signaling cascades mediated by G_i and G_q (Haga et al., 1985; Kubo et al., 1986; Nakamura et al., 1995). One action of mAChR activation is to suppress the KCNQ family of low-threshold voltage-gated potassium channels (Brown and Adams, 1980), ultimately increasing cell excitability. In addition, cholinergic activation uncovers a slow afterdepolarization (sADP) response which emerges after short periods of spiking activity, thought to trigger persistent firing if exceeding threshold levels (Egorov et al., 2002; Haj-Dahmane and Andrade, 1998; Navaroli et al., 2012; Rahman and Berger, 2011). Underlying the sADP are primarily calcium-activated nonspecific cationic (CAN) currents (Egorov et al., 2002; Hofmann and Frazier, 2010; Navaroli et al., 2012; Pressler and Strowbridge, 2006), although the molecular identity of channel species mediating this current is only recently becoming resolved (Lei et al., 2014; Zhang et al., 2011). Notably, these currents are dependent on the rise in intracellular calcium levels caused by opening of voltage-gated calcium channels (VGCCs) during persistent firing-triggering stimuli (Egorov et al., 2002; Pressler and Strowbridge, 2006; Rahman and Berger, 2011). Directly measuring calcium levels via jGCaMP8m, I also observed robust increase in intracellular calcium during stimulus periods. Whether the sustained calcium response is a driving mechanism, or rather a downstream consequence of persistent firing is yet unclear. Alternative mechanisms of sADP generation involve calcium-dependent suppression of leak potassium currents (Constanti et al., 1993; Constanti and Bagetta, 1991), notably through ERG channels (Cui and Strowbridge, 2018).

While both mechanisms may be involved in generating persistent firing in PPC neurons, the involvement of calcium in this process is nearly guaranteed.

There is early evidence that PT and IT subtypes of layer 5 neurons have distinct roles in working memory, representing parallel channels of information flow to cortical and subcortical regions (Bae et al., 2021; Musall et al., 2023). One key finding from this work is that PT neurons have longer-lasting, higher-frequency persistent firing than IT neurons in the PPC. This result is consistent with a previous report in the PFC (Dembrow et al., 2010). Given that cell type differences in sustained firing persist even in the absence of glutamatergic synaptic transmission, differences in cell-autonomous mechanisms likely favor persistent firing in PT over IT cells. One possibility is that triggering mechanisms differ between the cell types. Indeed, the sADP driving persistent firing (Haj-Dahmane and Andrade, 1998; Rahman and Berger, 2011) appears larger in PT than IT neurons in PPC, a result which was previously shown in PFC (Dembrow et al., 2010). Whether upstream VGCCs or downstream CAN and ERG channel effectors mediates cell-type-specific differences in persistent firing is an exciting possibility.

Other physiological differences may also explain the differential propensity of PT and IT neurons to trigger persistent firing. The threshold for action potential firing has been shown to be lower in PT than IT cells (Dembrow et al., 2010). My data also indicates that PT neuron spike thresholds during persistent firing are significantly more hyperpolarized than IT, suggesting that strong sustained activity in PT may simply reflect the proximity of these cells to threshold. Furthermore, IT neurons show pronounced spike frequency adaptation during suprathreshold step current injections (Dembrow et al., 2010; Hattox and Nelson, 2007), which could contribute to the early termination of firing in this cell type. In contrast, in PT neurons, strong “funny” current through hyperpolarization-activated cyclic-nucleotide-gated (HCN) channels which can

be approximated via sag potentials likely promotes sustained action potential firing by counteracting the adaptation response (Banks et al., 1993; Hattox and Nelson, 2007). Interestingly, while IT neurons are largely non-resonant, PT neurons have subthreshold resonance frequencies ranging from 2 to 5 Hz (Dembrow et al., 2010). This preferred input frequency was abolished when HCN channels were blocked (Dembrow et al., 2010). Notably, the persistent firing spike frequency of PT neurons I recorded also falls close to this resonance range (Figure 27D). In addition, PT/IB but not IT/RS neurons are capable of generating low-threshold calcium spikes, which are mediated by low-threshold (T-type) VGCCs (Yang et al., 1996), hinting at intrinsic differences in VGCC density which may underly heightened persistent firing in PT cells.

Alternatively, mechanisms that shut off persistent firing may differ between cell types. I previously demonstrated that IT neurons in PPC receive stronger feedforward inhibitory input than PT (Rindner et al., 2022). The synaptic transmission block I used here omitted blockers for GABAergic synapses. Strong feedback inhibition during persistent firing periods may also therefore dampen activity in IT. While I observed no indication that circuit mechanisms contribute to persistent firing in PPC, I do not exclude the possibility that *in vivo* persistent firing is network-dependent. Key signaling molecules in addition to acetylcholine, including epinephrine, norepinephrine, and dopamine are critical elements in modulating brain activity, and are absent in brain slice recordings. In addition, many local connections are likely severed in the slice preparation process. Furthermore, mechanisms for maintaining persistent firing may differ more than anticipated between direct single-cell and optogenetic afferent stimulation. Of course, the ideal experiment for testing the role of recurrent connections in persistent firing is the use precise targeting strategies to specifically inactivate local but not long-range synapse, effectively

decoupling cells. However, adequate methods for achieving this specificity in synapse silencing are currently lacking.

SUMMARY

Integration of feedforward and feedback information is a critical component of nearly all cognitive processes. However, how these pathways interact at the cellular level is poorly understood. My dissertation aims to uncover previously unknown mechanisms of feedforward-feedback signal integration, focusing on neurons in layer 5 of the posterior parietal cortex. In Chapter 1, I describe procedural improvements to a dual-color optogenetic technique for manipulating synaptic pathways. My "lookup table" approach allows up to two-fold increase in the dynamic range of opsin responses, which accelerates the throughput of highly challenging dual-color experiments. In Chapter 2, I use this optogenetic strategy to demonstrate that populations of layer 5 cells (PT/IB and IT/RS subtypes) selectively enhance feedforward-feedback synaptic input with distinct temporal dynamics. By combining data from electrophysiological, pharmacological, and computational modeling experiments, I then reveal ionic and circuit mechanisms that underly this cell-type-specific behavior. Lastly in Chapter 3, I expand on these findings to additionally show differences in the ability of PT and IT cell types to generate persistent firing, a neural signature of working memory. Through a series of experiments, I provide evidence that underlying this difference is a cell-intrinsic, rather than network-dependent mechanism. Taken together, my dissertation provides a possible cellular-level explanation for how feedforward-feedback synaptic interactions promote persistent firing in the cortex, and a potential role of cell types in mediating this response.

Where do we go from here? The sensitivity of L5 cell types to distinct feedforward and feedback input timings suggests a possible coding scheme used by the brain to communicate with certain cell populations but not others. If the same long-range axon synapses on both PT/IB

and IT/RS neurons, the relative timing of their input with that of other brain regions may "gate" the selective processing of that input by one or another cell type. While beyond the scope of the current dissertation, it would be informative to directly record the timing of input to PPC from higher (such as ACC) and lower (such as AUD, VIS) regions during complex behavioral tasks. Issues of crosstalk I address in Chapter 1 affect also optogenetic reporters, which are available with a range of peak spectral sensitivities. Combining a green- with a red-sensitive indicator, such as jGCaMP8m (Zhang et al., 2023) and jRGECO1a (Dana et al., 2016), may allow dual-color imaging of feedforward and feedback axon activity in PPC. Combining this imaging approach with direct electrical recording of PPC activity during a working memory task would be an extraordinary feat. Furthermore, computational decoding strategies often used to infer information stored in neural activity patterns can be extended to axon activity measurements and used to uncover the information content of input transmitted PPC.

In addition to passive measurements of feedforward and feedback axon activity, it would be insightful to manipulate, and particularly suppress, synaptic input to PPC during working memory tasks. A suite of inhibitory optogenetic proteins have been developed (Babl et al., 2019; Li et al., 2019), which can be used to silence synapses at distinct behavioral periods. For example, does silencing feedforward input to PPC affect behavior only during stimulus evaluation periods? Is feedback input to PPC necessary for delay period activity in working memory tasks? The use of inhibitory opsins may allow us to disambiguate the roles of distinct input sources, and directly test hypotheses of what information is being transmitted to PPC during cognitive tasks. It would furthermore be interesting to test synaptic input encoding and decoding in PPC in mouse models of human conditions characterized by acute cognitive deficits, such as Fragile X Syndrome (Melancia and Trezza, 2018), Alzheimer's Disease (Forner et al., 2021),

Schizophrenia (Jones et al., 2011), and sensorineural hearing loss (Ohlemiller et al., 2016). Repeating experiments described in Chapters 2 and 3 in such models may provide mechanistic insight to the role of feedforward-feedback integration, cell types, and persistent firing for the behavioral impairments observed in humans.

REFERENCES

Abrahamsson, T., Cathala, L., Matsui, K., Shigemoto, R., Digregorio, D.A., 2012. Thin dendrites of cerebellar interneurons confer sublinear synaptic integration and a gradient of short-term plasticity. Neuron 73, 1159–1172. https://doi.org/10.1016/j.neuron.2012.01.027

Adler, L.E., Pachtman, E., Franks, R.D., Pecevich, M., Waldo, M.C., Freedman, R., 1982. Neurophysiological evidence for a defect in neuronal mechanisms involved in sensory gating in schizophrenia. Biol Psychiatry 17, 639–654.

Agmon, A., Connors, B.W., 1991. Thalamocortical responses of mouse somatosensory (barrel) cortex in vitro. Neuroscience 41, 365–379. https://doi.org/10.1016/0306-4522(91)90333-j

Akaike, N., Hattori, K., Oomura, Y., Carpenter, D.O., 1985. Bicuculline and picrotoxin block γ-aminobutryic acid-gated Cl− conductance by different mechanisms. Experientia 41, 70–71. https://doi.org/10.1007/BF02005880

Akerboom, J., Carreras Calderón, N., Tian, L., Wabnig, S., Prigge, M., Tolö, J., Gordus, A., Orger, M.B., Severi, K.E., Macklin, J.J., Patel, R., Pulver, S.R., Wardill, T.J., Fischer, E., Schüler, C., Chen, T.-W., Sarkisyan, K.S., Marvin, J.S., Bargmann, C.I., Kim, D.S., Kügler, S., Lagnado, L., Hegemann, P., Gottschalk, A., Schreiter, E.R., Looger, L.L., 2013. Genetically encoded calcium indicators for multi-color neural activity imaging and combination with optogenetics. Front Mol Neurosci 6, 2. https://doi.org/10.3389/fnmol.2013.00002

Almog, M., Barkai, T., Lampert, A., Korngreen, A., 2018. Voltage-Gated Sodium Channels in Neocortical Pyramidal Neurons Display Cole-Moore Activation Kinetics. Frontiers in Cellular Neuroscience 12.

Anagnostaras, S.G., Murphy, G.G., Hamilton, S.E., Mitchell, S.L., Rahnama, N.P., Nathanson, N.M., Silva, A.J., 2003. Selective cognitive dysfunction in acetylcholine M1 muscarinic receptor mutant mice. Nat Neurosci 6, 51–58. https://doi.org/10.1038/nn992

Anastasiades, P.G., Marlin, J.J., Carter, A.G., 2018. Cell-Type Specificity of Callosally Evoked Excitation and Feedforward Inhibition in the Prefrontal Cortex. Cell Reports 22, 679–692. https://doi.org/10.1016/j.celrep.2017.12.073

Anderson, C.T., Sheets, P.L., Kiritani, T., Shepherd, G.M.G., 2010. Sublayer-specific microcircuits of corticospinal and corticostriatal neurons in motor cortex. Nat Neurosci 13, 739–744. https://doi.org/10.1038/nn.2538

Anisimova, M., van Bommel, B., Wang, R., Mikhaylova, M., Wiegert, J.S., Oertner, T.G., Gee, C.E., 2023. Spike-timing-dependent plasticity rewards synchrony rather than causality. Cerebral Cortex 33, 23–34. https://doi.org/10.1093/cercor/bhac050

Ardevol, A., Hummer, G., 2018. Retinal isomerization and water-pore formation in channelrhodopsin-2. Proceedings of the National Academy of Sciences 115, 3557–3562. https://doi.org/10.1073/pnas.1700091115

Ariav, G., Polsky, A., Schiller, J., 2003. Submillisecond Precision of the Input-Output Transformation Function Mediated by Fast Sodium Dendritic Spikes in Basal Dendrites of CA1 Pyramidal Neurons. J. Neurosci. 23, 7750–7758. https://doi.org/10.1523/JNEUROSCI.23-21-07750.2003

Ascoli, G.A., Alonso-Nanclares, L., Anderson, S.A., Barrionuevo, G., Benavides-Piccione, R., Burkhalter, A., Buzsáki, G., Cauli, B., DeFelipe, J., Fairén, A., Feldmeyer, D., Fishell, G., Fregnac, Y., Freund, T.F., Gardner, D., Gardner, E.P., Goldberg, J.H., Helmstaedter, M., Hestrin, S., Karube, F., Kisvárday, Z.F., Lambolez, B., Lewis, D.A., Marin, O., Markram, H., Muñoz, A., Packer, A., Petersen, C.C.H., Rockland, K.S., Rossier, J., Rudy, B., Somogyi, P., Staiger, J.F., Tamas, G., Thomson, A.M., Toledo-Rodriguez, M., Wang, Y., West, D.C., Yuste, R., The Petilla Interneuron Nomenclature Group (PING), 2008. Petilla terminology: nomenclature of features of GABAergic interneurons of the cerebral cortex. Nat Rev Neurosci 9, 557–568. https://doi.org/10.1038/nrn2402

Atallah, B.V., Bruns, W., Carandini, M., Scanziani, M., 2012. Parvalbumin-Expressing Interneurons Linearly Transform Cortical Responses to Visual Stimuli. Neuron 73, 159–170. https://doi.org/10.1016/j.neuron.2011.12.013

Atherton, L.A., Burnell, E.S., Mellor, J.R., 2016. Assessment of Methods for the Intracellular Blockade of GABAA Receptors. PLoS ONE 11. https://doi.org/10.1371/journal.pone.0160900

Azouz, R., Jensen, M.S., Yaari, Y., 1996. Ionic basis of spike after-depolarization and burst generation in adult rat hippocampal CA1 pyramidal cells. The Journal of Physiology 492, 211–223. https://doi.org/10.1113/jphysiol.1996.sp021302

Babl, S.S., Rummell, B.P., Sigurdsson, T., 2019. The Spatial Extent of Optogenetic Silencing in Transgenic Mice Expressing Channelrhodopsin in Inhibitory Interneurons. Cell Reports 29, 1381-1395.e4. https://doi.org/10.1016/j.celrep.2019.09.049

Bae, J.W., Jeong, H., Yoon, Y.J., Bae, C.M., Lee, H., Paik, S.-B., Jung, M.W., 2021. Parallel processing of working memory and temporal information by distinct types of cortical projection neurons. Nat Commun 12, 4352. https://doi.org/10.1038/s41467-021-24565-z

Baker, A., Kalmbach, B., Morishima, M., Kim, J., Juavinett, A., Li, N., Dembrow, N., 2018. Specialized Subpopulations of Deep-Layer Pyramidal Neurons in the Neocortex: Bridging Cellular Properties to Functional Consequences. J Neurosci 38, 5441–5455. https://doi.org/10.1523/JNEUROSCI.0150-18.2018

Banks, M.I., Pearce, R.A., Smith, P.H., 1993. Hyperpolarization-activated cation current (Ih) in neurons of the medial nucleus of the trapezoid body: voltage-clamp analysis and enhancement by norepinephrine and cAMP suggest a modulatory mechanism in the auditory brain stem. J Neurophysiol 70, 1420–1432. https://doi.org/10.1152/jn.1993.70.4.1420

Bauer, J., Weiler, S., Fernholz, M.H.P., Laubender, D., Scheuss, V., Hübener, M., Bonhoeffer, T., Rose, T., 2021. Limited functional convergence of eye-specific inputs in the retinogeniculate pathway of the mouse. Neuron 109, 2457-2468.e12. https://doi.org/10.1016/j.neuron.2021.05.036

Becker-Baldus, J., Bamann, C., Saxena, K., Gustmann, H., Brown, L.J., Brown, R.C.D., Reiter, C., Bamberg, E., Wachtveitl, J., Schwalbe, H., Glaubitz, C., 2015. Enlightening the photoactive site of channelrhodopsin-2 by DNP-enhanced solid-state NMR spectroscopy. Proc Natl Acad Sci U S A 112, 9896–9901. https://doi.org/10.1073/pnas.1507713112

Bedbrook, C.N., Yang, K.K., Robinson, J.E., Mackey, E.D., Gradinaru, V., Arnold, F.H., 2019. Machine learning-guided channelrhodopsin engineering enables minimally invasive optogenetics. Nat Methods 16, 1176–1184. https://doi.org/10.1038/s41592-019-0583-8

Bell, A.H., Meredith, M.A., Van Opstal, A.J., Munoz, D.P., 2005. Crossmodal Integration in the Primate Superior Colliculus Underlying the Preparation and Initiation of Saccadic Eye Movements. Journal of Neurophysiology 93, 3659–3673. https://doi.org/10.1152/jn.01214.2004

Berndt, A., Lee, S.Y., Wietek, J., Ramakrishnan, C., Steinberg, E.E., Rashid, A.J., Kim, H., Park, S., Santoro, A., Frankland, P.W., Iyer, S.M., Pak, S., Ährlund-Richter, S., Delp, S.L., Malenka, R.C., Josselyn, S.A., Carlén, M., Hegemann, P., Deisseroth, K., 2016. Structural foundations of optogenetics: Determinants of channelrhodopsin ion selectivity. Proceedings of the National Academy of Sciences 113, 822–829. https://doi.org/10.1073/pnas.1523341113

Berndt, A., Schoenenberger, P., Mattis, J., Tye, K.M., Deisseroth, K., Hegemann, P., Oertner, T.G., 2011. High-efficiency channelrhodopsins for fast neuronal stimulation at low light levels. Proceedings of the National Academy of Sciences 108, 7595–7600. https://doi.org/10.1073/pnas.1017210108

Berndt, A., Yizhar, O., Gunaydin, L.A., Hegemann, P., Deisseroth, K., 2009. Bi-stable neural state switches. Nat Neurosci 12, 229–234. https://doi.org/10.1038/nn.2247

Berti, A., Rizzolatti, G., 1992. Visual Processing without Awareness: Evidence from Unilateral Neglect. J Cogn Neurosci 4, 345–351. https://doi.org/10.1162/jocn.1992.4.4.345

Birdsong, W.T., Jongbloets, B.C., Engeln, K.A., Wang, D., Scherrer, G., Mao, T., 2019. Synapse-specific opioid modulation of thalamo-cortico-striatal circuits. eLife 8, e45146. https://doi.org/10.7554/eLife.45146

Bisiach, E., Luzzatti, C., 1978. Unilateral Neglect of Representational Space. Cortex 14, 129–133. https://doi.org/10.1016/S0010-9452(78)80016-1

Borchers, S., Himmelbach, M., Logothetis, N., Karnath, H.-O., 2012. Direct electrical stimulation of human cortex — the gold standard for mapping brain functions? Nat Rev Neurosci 13, 63–70. https://doi.org/10.1038/nrn3140

Boyden, E.S., Zhang, F., Bamberg, E., Nagel, G., Deisseroth, K., 2005. Millisecond-timescale, genetically targeted optical control of neural activity. Nat Neurosci 8, 1263–1268. https://doi.org/10.1038/nn1525

Braver, T.S., Reynolds, J.R., Donaldson, D.I., 2003. Neural mechanisms of transient and sustained cognitive control during task switching. Neuron 39, 713–726. https://doi.org/10.1016/s0896-6273(03)00466-5

Brown, D.A., Adams, P.R., 1980. Muscarinic suppression of a novel voltage-sensitive K+ current in a vertebrate neurone. Nature 283, 673–676. https://doi.org/10.1038/283673a0

Brown, S.P., Hestrin, S., 2009. Intracortical circuits of pyramidal neurons reflect their long-range axonal targets. Nature 457, 1133–1136. https://doi.org/10.1038/nature07658

Brumberg, J.C., Nowak, L.G., McCormick, D.A., 2000. Ionic Mechanisms Underlying Repetitive High-Frequency Burst Firing in Supragranular Cortical Neurons. J. Neurosci. 20, 4829–4843. https://doi.org/10.1523/JNEUROSCI.20-13-04829.2000

Bugelski, B.R., Alampay, D.A., 1961. The role of frequency in developing perceptual sets. Canadian Journal of Psychology / Revue canadienne de psychologie 15, 205–211. https://doi.org/10.1037/h0083443

Bunge, S.A., Kahn, I., Wallis, J.D., Miller, E.K., Wagner, A.D., 2003. Neural circuits subserving the retrieval and maintenance of abstract rules. J Neurophysiol 90, 3419–3428. https://doi.org/10.1152/jn.00910.2002

Buschman, T.J., Miller, E.K., 2007. Top-down versus bottom-up control of attention in the prefrontal and posterior parietal cortices. Science 315, 1860–1862. https://doi.org/10.1126/science.1138071

Cappe, C., Morel, A., Barone, P., Rouiller, E.M., 2009. The Thalamocortical Projection Systems in Primate: An Anatomical Support for Multisensory and Sensorimotor Interplay. Cereb Cortex 19, 2025–2037. https://doi.org/10.1093/cercor/bhn228

Carrillo-Reid, L., Yang, W., Bando, Y., Peterka, D.S., Yuste, R., 2016. Imprinting and recalling cortical ensembles. Science 353, 691–694. https://doi.org/10.1126/science.aaf7560

Cash, S., Yuste, R., 1999. Linear summation of excitatory inputs by CA1 pyramidal neurons. Neuron 22, 383–394. https://doi.org/10.1016/s0896-6273(00)81098-3

Cauller, L.J., Connors, B.W., 1994. Synaptic physiology of horizontal afferents to layer I in slices of rat SI neocortex. J. Neurosci. 14, 751–762. https://doi.org/10.1523/JNEUROSCI.14-02-00751.1994

Chagnac-Amitai, Y., Luhmann, H.J., Prince, D.A., 1990. Burst generating and regular spiking layer 5 pyramidal neurons of rat neocortex have different morphological features. Journal of Comparative Neurology 296, 598–613. https://doi.org/10.1002/cne.902960407

Chandler, H.C., King, V., Corwin, J.V., Reep, R.L., 1992. Thalamocortical connections of rat posterior parietal cortex. Neuroscience Letters 143, 237–242. https://doi.org/10.1016/0304-3940(92)90273-A

Chen, X., Leischner, U., Rochefort, N.L., Nelken, I., Konnerth, A., 2011. Functional mapping of single spines in cortical neurons in vivo. Nature 475, 501–505. https://doi.org/10.1038/nature10193

Chiu, C.Q., Martenson, J.S., Yamazaki, M., Natsume, R., Sakimura, K., Tomita, S., Tavalin, S.J., Higley, M.J., 2018. Input-Specific NMDAR-Dependent Potentiation of Dendritic GABAergic Inhibition. Neuron 97, 368-377.e3. https://doi.org/10.1016/j.neuron.2017.12.032

Chivukula, S., Zhang, C.Y., Aflalo, T., Jafari, M., Pejsa, K., Pouratian, N., Andersen, R.A., 2021. Neural encoding of actual and imagined touch within human posterior parietal cortex. eLife 10, e61646. https://doi.org/10.7554/eLife.61646

Christoffel, D.J., Walsh, J.J., Heifets, B.D., Hoerbelt, P., Neuner, S., Sun, G., Ravikumar, V.K., Wu, H., Halpern, C.H., Malenka, R.C., 2021. Input-specific modulation of murine nucleus accumbens differentially regulates hedonic feeding. Nat Commun 12, 2135. https://doi.org/10.1038/s41467-021-22430-7

Churchland, M.M., Shenoy, K.V., 2007. Delay of Movement Caused by Disruption of Cortical Preparatory Activity. Journal of Neurophysiology 97, 348–359. https://doi.org/10.1152/jn.00808.2006

Ciaramelli, E., Rosenbaum, R.S., Solcz, S., Levine, B., Moscovitch, M., 2010. Mental space travel: Damage to posterior parietal cortex prevents egocentric navigation and reexperiencing

of remote spatial memories. Journal of Experimental Psychology: Learning, Memory, and Cognition 36, 619–634. https://doi.org/10.1037/a0019181
Cisler, J.M., Wolitzky-Taylor, K.B., Adams, T.G., Babson, K.A., Badour, C.L., Willems, J.L., 2011. The emotional Stroop task and posttraumatic stress disorder: A meta-analysis. Clinical Psychology Review 31, 817–828. https://doi.org/10.1016/j.cpr.2011.03.007
Compte, A., Brunel, N., Goldman-Rakic, P.S., Wang, X.-J., 2000. Synaptic Mechanisms and Network Dynamics Underlying Spatial Working Memory in a Cortical Network Model. Cerebral Cortex 10, 910–923. https://doi.org/10.1093/cercor/10.9.910
Connors, B.W., Gutnick, M.J., Prince, D.A., 1982. Electrophysiological properties of neocortical neurons in vitro. J Neurophysiol 48, 1302–1320. https://doi.org/10.1152/jn.1982.48.6.1302
Constanti, A., Bagetta, G., 1991. Muscarinic receptor activation induces a prolonged post-stimulus afterdepolarization with a conductance decrease in guinea-pig olfactory cortex neurones in vitro. Neuroscience Letters 131, 27–32. https://doi.org/10.1016/0304-3940(91)90329-R
Constanti, A., Bagetta, G., Libri, V., 1993. Persistent muscarinic excitation in guinea-pig olfactory cortex neurons: Involvement of a slow post-stimulus afterdepolarizing current. Neuroscience 56, 887–904. https://doi.org/10.1016/0306-4522(93)90135-3
Constantinidis, C., Funahashi, S., Lee, D., Murray, J.D., Qi, X.-L., Wang, M., Arnsten, A.F.T., 2018. Persistent Spiking Activity Underlies Working Memory. J Neurosci 38, 7020–7028. https://doi.org/10.1523/JNEUROSCI.2486-17.2018
Constantinidis, C., Steinmetz, M.A., 1996. Neuronal activity in posterior parietal area 7a during the delay periods of a spatial memory task. J Neurophysiol 76, 1352–1355. https://doi.org/10.1152/jn.1996.76.2.1352
Conte, W.L., Kamishina, H., Reep, R.L., 2009. Multiple neuroanatomical tract-tracing using fluorescent Alexa Fluor conjugates of cholera toxin subunit B in rats. Nat Protoc 4, 1157–1166. https://doi.org/10.1038/nprot.2009.93
Cruikshank, S.J., Rose, H.J., Metherate, R., 2002. Auditory thalamocortical synaptic transmission in vitro. J Neurophysiol 87, 361–384. https://doi.org/10.1152/jn.00549.2001
Cruikshank, S.J., Urabe, H., Nurmikko, A.V., Connors, B.W., 2010. Pathway-Specific Feedforward Circuits between Thalamus and Neocortex Revealed by Selective Optical Stimulation of Axons. Neuron 65, 230–245. https://doi.org/10.1016/j.neuron.2009.12.025
Cui, E.D., Estright, A.W., Pressler, R.T., Strowbridge, B.W., 2022. Spike Afterhyperpolarizations Govern Persistent Firing Dynamics in Rat Neocortical and Hippocampal Pyramidal Cells. J Neurosci 42, 7690–7706. https://doi.org/10.1523/JNEUROSCI.0570-22.2022
Cui, E.D., Strowbridge, B.W., 2018. Modulation of Ether-à-Go-Go Related Gene (ERG) Current Governs Intrinsic Persistent Activity in Rodent Neocortical Pyramidal Cells. J Neurosci 38, 423–440. https://doi.org/10.1523/JNEUROSCI.1774-17.2017
Dana, H., Mohar, B., Sun, Y., Narayan, S., Gordus, A., Hasseman, J.P., Tsegaye, G., Holt, G.T., Hu, A., Walpita, D., Patel, R., Macklin, J.J., Bargmann, C.I., Ahrens, M.B., Schreiter, E.R., Jayaraman, V., Looger, L.L., Svoboda, K., Kim, D.S., 2016. Sensitive red protein calcium indicators for imaging neural activity. eLife 5, e12727. https://doi.org/10.7554/eLife.12727

Dantzker, J.L., Callaway, E.M., 2000. Laminar sources of synaptic input to cortical inhibitory interneurons and pyramidal neurons. Nat Neurosci 3, 701–707. https://doi.org/10.1038/76656

Dembrow, N.C., Chitwood, R.A., Johnston, D., 2010. Projection-Specific Neuromodulation of Medial Prefrontal Cortex Neurons. J. Neurosci. 30, 16922–16937. https://doi.org/10.1523/JNEUROSCI.3644-10.2010

Dembrow, N.C., Zemelman, B.V., Johnston, D., 2015. Temporal Dynamics of L5 Dendrites in Medial Prefrontal Cortex Regulate Integration Versus Coincidence Detection of Afferent Inputs. J. Neurosci. 35, 4501–4514. https://doi.org/10.1523/JNEUROSCI.4673-14.2015

Desmurget, M., Epstein, C.M., Turner, R.S., Prablanc, C., Alexander, G.E., Grafton, S.T., 1999. Role of the posterior parietal cortex in updating reaching movements to a visual target. Nat Neurosci 2, 563–567. https://doi.org/10.1038/9219

Desmurget, M., Reilly, K.T., Richard, N., Szathmari, A., Mottolese, C., Sirigu, A., 2009. Movement intention after parietal cortex stimulation in humans. Science 324, 811–813. https://doi.org/10.1126/science.1169896

Diederich, A., Colonius, H., 2004. Bimodal and trimodal multisensory enhancement: effects of stimulus onset and intensity on reaction time. Percept Psychophys 66, 1388–1404. https://doi.org/10.3758/bf03195006

Dosenbach, N.U.F., Fair, D.A., Miezin, F.M., Cohen, A.L., Wenger, K.K., Dosenbach, R.A.T., Fox, M.D., Snyder, A.Z., Vincent, J.L., Raichle, M.E., Schlaggar, B.L., Petersen, S.E., 2007. Distinct brain networks for adaptive and stable task control in humans. Proc Natl Acad Sci U S A 104, 11073–11078. https://doi.org/10.1073/pnas.0704320104

Dosenbach, N.U.F., Visscher, K.M., Palmer, E.D., Miezin, F.M., Wenger, K.K., Kang, H.C., Burgund, E.D., Grimes, A.L., Schlaggar, B.L., Petersen, S.E., 2006. A Core System for the Implementation of Task Sets. Neuron 50, 799–812. https://doi.org/10.1016/j.neuron.2006.04.031

Egger, R., Schmitt, A.C., Wallace, D.J., Sakmann, B., Oberlaender, M., Kerr, J.N.D., 2015. Robustness of sensory-evoked excitation is increased by inhibitory inputs to distal apical tuft dendrites. Proceedings of the National Academy of Sciences 112, 14072–14077. https://doi.org/10.1073/pnas.1518773112

Egorov, A.V., Hamam, B.N., Fransén, E., Hasselmo, M.E., Alonso, A.A., 2002. Graded persistent activity in entorhinal cortex neurons. Nature 420, 173–178. https://doi.org/10.1038/nature01171

Emiliani, V., Entcheva, E., Hedrich, R., Hegemann, P., Konrad, K.R., Lüscher, C., Mahn, M., Pan, Z.-H., Sims, R.R., Vierock, J., Yizhar, O., 2022. Optogenetics for light control of biological systems. Nat Rev Methods Primers 2, 1–25. https://doi.org/10.1038/s43586-022-00136-4

Esmaeili, V., Tamura, K., Muscinelli, S.P., Modirshanechi, A., Boscaglia, M., Lee, A.B., Oryshchuk, A., Foustoukos, G., Liu, Y., Crochet, S., Gerstner, W., Petersen, C.C.H., 2021. Rapid suppression and sustained activation of distinct cortical regions for a delayed sensory-triggered motor response. Neuron 109, 2183-2201.e9. https://doi.org/10.1016/j.neuron.2021.05.005

Fanini, A., Assad, J.A., 2009. Direction selectivity of neurons in the macaque lateral intraparietal area. J Neurophysiol 101, 289–305. https://doi.org/10.1152/jn.00400.2007

Farhi, S.L., Parot, V.J., Grama, A., Yamagata, M., Abdelfattah, A.S., Adam, Y., Lou, S., Kim, J.J., Campbell, R.E., Cox, D.D., Cohen, A.E., 2019. Wide-Area All-Optical Neurophysiology in Acute Brain Slices. J Neurosci 39, 4889–4908. https://doi.org/10.1523/JNEUROSCI.0168-19.2019

Flevaris, A.V., Murray, S.O., 2015. Attention Determines Contextual Enhancement versus Suppression in Human Primary Visual Cortex. J. Neurosci. 35, 12273–12280. https://doi.org/10.1523/JNEUROSCI.1409-15.2015

Forner, S., Kawauchi, S., Balderrama-Gutierrez, G., Kramár, E.A., Matheos, D.P., Phan, J., Javonillo, D.I., Tran, K.M., Hingco, E., da Cunha, C., Rezaie, N., Alcantara, J.A., Baglietto-Vargas, D., Jansen, C., Neumann, J., Wood, M.A., MacGregor, G.R., Mortazavi, A., Tenner, A.J., LaFerla, F.M., Green, K.N., 2021. Systematic phenotyping and characterization of the 5xFAD mouse model of Alzheimer's disease. Sci Data 8, 270. https://doi.org/10.1038/s41597-021-01054-y

Fransén, E., Tahvildari, B., Egorov, A.V., Hasselmo, M.E., Alonso, A.A., 2006. Mechanism of Graded Persistent Cellular Activity of Entorhinal Cortex Layer V Neurons. Neuron 49, 735–746. https://doi.org/10.1016/j.neuron.2006.01.036

Frens, M.A., Van Opstal, A.J., Van Der Willigen, R.F., 1995. Spatial and temporal factors determine auditory-visual interactions in human saccadic eye movements. Perception & Psychophysics 57, 802–816. https://doi.org/10.3758/BF03206796

Fritz, J., Shamma, S., Elhilali, M., Klein, D., 2003. Rapid task-related plasticity of spectrotemporal receptive fields in primary auditory cortex. Nat Neurosci 6, 1216–1223. https://doi.org/10.1038/nn1141

Funahashi, S., Bruce, C.J., Goldman-Rakic, P.S., 1989. Mnemonic coding of visual space in the monkey's dorsolateral prefrontal cortex. J Neurophysiol 61, 331–349. https://doi.org/10.1152/jn.1989.61.2.331

Galloni, A.R., Ye, Z., Rancz, E., 2022. Dendritic Domain-Specific Sampling of Long-Range Axons Shapes Feedforward and Feedback Connectivity of L5 Neurons. J. Neurosci. 42, 3394–3405. https://doi.org/10.1523/JNEUROSCI.1620-21.2022

Gao, W.-J., Zheng, Z.-H., 2004. Target-specific differences in somatodendritic morphology of layer V pyramidal neurons in rat motor cortex. Journal of Comparative Neurology 476, 174–185. https://doi.org/10.1002/cne.20224

Garcia, A.F., Crummy, E.A., Webb, I.G., Nooney, M.N., Ferguson, S.M., 2021. Distinct populations of cortical pyramidal neurons mediate drug reward and aversion. Nat Commun 12, 182. https://doi.org/10.1038/s41467-020-20526-0

Gasparini, S., Migliore, M., Magee, J.C., 2004. On the initiation and propagation of dendritic spikes in CA1 pyramidal neurons. J Neurosci 24, 11046–11056. https://doi.org/10.1523/JNEUROSCI.2520-04.2004

Gates, G.A., Karzon, R.K., Garcia, P., Peterein, J., Storandt, M., Morris, J.C., Miller, J.P., 1995. Auditory Dysfunction in Aging and Senile Dementia of the Alzheimer's Type. Archives of Neurology 52, 626–634. https://doi.org/10.1001/archneur.1995.00540300108020

Gazzaley, A., Cooney, J.W., McEvoy, K., Knight, R.T., D'Esposito, M., 2005a. Top-down Enhancement and Suppression of the Magnitude and Speed of Neural Activity. Journal of Cognitive Neuroscience 17, 507–517. https://doi.org/10.1162/0898929053279522

Gazzaley, A., Cooney, J.W., Rissman, J., D'Esposito, M., 2005b. Top-down suppression deficit underlies working memory impairment in normal aging. Nat Neurosci 8, 1298–1300. https://doi.org/10.1038/nn1543

Gehring, W.J., Willoughby, A.R., 2002. The Medial Frontal Cortex and the Rapid Processing of Monetary Gains and Losses. Science 295, 2279–2282. https://doi.org/10.1126/science.1066893

Ghanizadeh, A., Bahrani, M., Miri, R., Sahraian, A., 2012. Smell Identification Function in Children with Attention Deficit Hyperactivity Disorder. Psychiatry Investig 9, 150–153. https://doi.org/10.4306/pi.2012.9.2.150

Gharbawie, O.A., Stepniewska, I., Burish, M.J., Kaas, J.H., 2010. Thalamocortical Connections of Functional Zones in Posterior Parietal Cortex and Frontal Cortex Motor Regions in New World Monkeys. Cerebral Cortex 20, 2391–2410. https://doi.org/10.1093/cercor/bhp308

Gibson, J.R., Beierlein, M., Connors, B.W., 1999. Two networks of electrically coupled inhibitory neurons in neocortex. Nature 402, 75–79. https://doi.org/10.1038/47035

Gilbert, C.D., Sigman, M., 2007. Brain States: Top-Down Influences in Sensory Processing. Neuron 54, 677–696. https://doi.org/10.1016/j.neuron.2007.05.019

Glickfeld, L.L., Andermann, M.L., Bonin, V., Reid, R.C., 2013. Cortico-cortical projections in mouse visual cortex are functionally target specific. Nat Neurosci 16, 219–226. https://doi.org/10.1038/nn.3300

Goard, M.J., Pho, G.N., Woodson, J., Sur, M., 2016. Distinct roles of visual, parietal, and frontal motor cortices in memory-guided sensorimotor decisions. Elife 5, e13764. https://doi.org/10.7554/eLife.13764

Golding, N.L., Jung, H., Mickus, T., Spruston, N., 1999. Dendritic Calcium Spike Initiation and Repolarization Are Controlled by Distinct Potassium Channel Subtypes in CA1 Pyramidal Neurons. J. Neurosci. 19, 8789–8798. https://doi.org/10.1523/JNEUROSCI.19-20-08789.1999

Golding, N.L., Spruston, N., 1998. Dendritic sodium spikes are variable triggers of axonal action potentials in hippocampal CA1 pyramidal neurons. Neuron 21, 1189–1200. https://doi.org/10.1016/s0896-6273(00)80635-2

Goldstein, S.S., Rall, W., 1974. Changes of Action Potential Shape and Velocity for Changing Core Conductor Geometry. Biophysical Journal 14, 731–757. https://doi.org/10.1016/S0006-3495(74)85947-3

Gong, X., Mendoza-Halliday, D., Ting, J.T., Kaiser, T., Sun, X., Bastos, A.M., Wimmer, R.D., Guo, B., Chen, Q., Zhou, Y., Pruner, M., Wu, C.W.-H., Park, D., Deisseroth, K., Barak, B., Boyden, E.S., Miller, E.K., Halassa, M.M., Fu, Z., Bi, G., Desimone, R., Feng, G., 2020. An Ultra-Sensitive Step-Function Opsin for Minimally Invasive Optogenetic Stimulation in Mice and Macaques. Neuron 107, 38-51.e8. https://doi.org/10.1016/j.neuron.2020.03.032

Granon, S., Poucet, B., Thinus-Blanc, C., Changeux, J.-P., Vidal, C., 1995. Nicotinic and muscarinic receptors in the rat prefrontal cortex: Differential roles in working memory, response selection and effortful processing. Psychopharmacology 119, 139–144. https://doi.org/10.1007/BF02246154

Greenberg, A.S., Esterman, M., Wilson, D., Serences, J.T., Yantis, S., 2010. Control of spatial and feature-based attention in frontoparietal cortex. J Neurosci 30, 14330–14339. https://doi.org/10.1523/JNEUROSCI.4248-09.2010

Groh, A., Meyer, H.S., Schmidt, E.F., Heintz, N., Sakmann, B., Krieger, P., 2010. Cell-Type Specific Properties of Pyramidal Neurons in Neocortex Underlying a Layout that Is Modifiable Depending on the Cortical Area. Cerebral Cortex 20, 826–836. https://doi.org/10.1093/cercor/bhp152

Gunaydin, L.A., Yizhar, O., Berndt, A., Sohal, V.S., Deisseroth, K., Hegemann, P., 2010. Ultrafast optogenetic control. Nat Neurosci 13, 387–392. https://doi.org/10.1038/nn.2495

Guo, Z.V., Li, N., Huber, D., Ophir, E., Gutnisky, D., Ting, J.T., Feng, G., Svoboda, K., 2014. Flow of Cortical Activity Underlying a Tactile Decision in Mice. Neuron 81, 179–194. https://doi.org/10.1016/j.neuron.2013.10.020

Habtegiorgis, S.W., Jarvers, C., Rifai, K., Neumann, H., Wahl, S., 2019. The Role of Bottom-Up and Top-Down Cortical Interactions in Adaptation to Natural Scene Statistics. Frontiers in Neural Circuits 13.

Haegens, S., Osipova, D., Oostenveld, R., Jensen, O., 2010. Somatosensory working memory performance in humans depends on both engagement and disengagement of regions in a distributed network. Hum Brain Mapp 31, 26–35. https://doi.org/10.1002/hbm.20842

Haga, K., Haga, T., Ichiyama, A., Katada, T., Kurose, H., Ui, M., 1985. Functional reconstitution of purified muscarinic receptors and inhibitory guanine nucleotide regulatory protein. Nature 316, 731–733. https://doi.org/10.1038/316731a0

Haj-Dahmane, S., Andrade, R., 1998. Ionic Mechanism of the Slow Afterdepolarization Induced by Muscarinic Receptor Activation in Rat Prefrontal Cortex. Journal of Neurophysiology 80, 1197–1210. https://doi.org/10.1152/jn.1998.80.3.1197

Han, S., Yang, W., Yuste, R., 2019. Two-Color Volumetric Imaging of Neuronal Activity of Cortical Columns. Cell Reports 27, 2229-2240.e4. https://doi.org/10.1016/j.celrep.2019.04.075

Han, X., Boyden, E.S., 2007. Multiple-Color Optical Activation, Silencing, and Desynchronization of Neural Activity, with Single-Spike Temporal Resolution. PLoS ONE 2, e299. https://doi.org/10.1371/journal.pone.0000299

Harnett, M.T., Magee, J.C., Williams, S.R., 2015. Distribution and Function of HCN Channels in the Apical Dendritic Tuft of Neocortical Pyramidal Neurons. J. Neurosci. 35, 1024–1037. https://doi.org/10.1523/JNEUROSCI.2813-14.2015

Harris, K.D., Shepherd, G.M.G., 2015. The neocortical circuit: themes and variations. Nat Neurosci 18, 170–181. https://doi.org/10.1038/nn.3917

Hattox, A.M., Nelson, S.B., 2007. Layer V neurons in mouse cortex projecting to different targets have distinct physiological properties. J Neurophysiol 98, 3330–3340. https://doi.org/10.1152/jn.00397.2007

Häusser, M., Clark, B.A., 1997. Tonic Synaptic Inhibition Modulates Neuronal Output Pattern and Spatiotemporal Synaptic Integration. Neuron 19, 665–678. https://doi.org/10.1016/S0896-6273(00)80379-7

Hefti, B.J., Smith, P.H., 2000. Anatomy, Physiology, and Synaptic Responses of Rat Layer V Auditory Cortical Cells and Effects of Intracellular GABAABlockade. Journal of Neurophysiology 83, 2626–2638. https://doi.org/10.1152/jn.2000.83.5.2626

Helmchen, F., Svoboda, K., Denk, W., Tank, D.W., 1999. In vivo dendritic calcium dynamics in deep-layer cortical pyramidal neurons. Nat Neurosci 2, 989–996. https://doi.org/10.1038/14788

Hines, M.L., Carnevale, N.T., 1997. The NEURON Simulation Environment. Neural Computation 9, 1179–1209. https://doi.org/10.1162/neco.1997.9.6.1179

Hjaltason, H., Tegnér, R., Tham, K., Levander, M., Ericson, K., 1996. Sustained attention and awareness of disability in chronic neglect. Neuropsychologia 34, 1229–1233. https://doi.org/10.1016/0028-3932(96)00044-9

Hochbaum, D.R., Zhao, Y., Farhi, S.L., Klapoetke, N., Werley, C.A., Kapoor, V., Zou, P., Kralj, J.M., Maclaurin, D., Smedemark-Margulies, N., Saulnier, J.L., Boulting, G.L., Straub, C., Cho, Y.K., Melkonian, M., Wong, G.K.-S., Harrison, D.J., Murthy, V.N., Sabatini, B.L., Boyden, E.S., Campbell, R.E., Cohen, A.E., 2014. All-optical electrophysiology in mammalian neurons using engineered microbial rhodopsins. Nat Methods 11, 825–833. https://doi.org/10.1038/nmeth.3000

Hodge, R.D., Bakken, T.E., Miller, J.A., Smith, K.A., Barkan, E.R., Graybuck, L.T., Close, J.L., Long, B., Johansen, N., Penn, O., Yao, Z., Eggermont, J., Höllt, T., Levi, B.P., Shehata, S.I., Aevermann, B., Beller, A., Bertagnolli, D., Brouner, K., Casper, T., Cobbs, C., Dalley, R., Dee, N., Ding, S.-L., Ellenbogen, R.G., Fong, O., Garren, E., Goldy, J., Gwinn, R.P., Hirschstein, D., Keene, C.D., Keshk, M., Ko, A.L., Lathia, K., Mahfouz, A., Maltzer, Z., McGraw, M., Nguyen, T.N., Nyhus, J., Ojemann, J.G., Oldre, A., Parry, S., Reynolds, S., Rimorin, C., Shapovalova, N.V., Somasundaram, S., Szafer, A., Thomsen, E.R., Tieu, M., Quon, G., Scheuermann, R.H., Yuste, R., Sunkin, S.M., Lelieveldt, B., Feng, D., Ng, L., Bernard, A., Hawrylycz, M., Phillips, J.W., Tasic, B., Zeng, H., Jones, A.R., Koch, C., Lein, E.S., 2019. Conserved cell types with divergent features in human versus mouse cortex. Nature 573, 61–68. https://doi.org/10.1038/s41586-019-1506-7

Hofmann, M.E., Frazier, C.J., 2010. Muscarinic receptor activation modulates the excitability of hilar mossy cells through the induction of an afterdepolarization. Brain Research 1318, 42–51. https://doi.org/10.1016/j.brainres.2010.01.011

Hooks, B.M., Lin, J.Y., Guo, C., Svoboda, K., 2015. Dual-Channel Circuit Mapping Reveals Sensorimotor Convergence in the Primary Motor Cortex. J. Neurosci. 35, 4418–4426. https://doi.org/10.1523/JNEUROSCI.3741-14.2015

Hooks, B.M., Papale, A.E., Paletzki, R.F., Feroze, M.W., Eastwood, B.S., Couey, J.J., Winnubst, J., Chandrashekar, J., Gerfen, C.R., 2018. Topographic precision in sensory and motor corticostriatal projections varies across cell type and cortical area. Nat Commun 9, 3549. https://doi.org/10.1038/s41467-018-05780-7

Huguenard, J.R., Prince, D.A., 1992. A novel T-type current underlies prolonged Ca(2+)-dependent burst firing in GABAergic neurons of rat thalamic reticular nucleus. J. Neurosci. 12, 3804–3817. https://doi.org/10.1523/JNEUROSCI.12-10-03804.1992

Ibos, G., Freedman, D.J., 2014. Dynamic integration of task-relevant visual features in posterior parietal cortex. Neuron 83, 1468–1480. https://doi.org/10.1016/j.neuron.2014.08.020

Inagaki, H.K., Fontolan, L., Romani, S., Svoboda, K., 2019. Discrete attractor dynamics underlies persistent activity in the frontal cortex. Nature 566, 212–217. https://doi.org/10.1038/s41586-019-0919-7

Inomata, N., Tokutomi, N., Oyama, Y., Akaike, N., 1988. Intracellular picrotoxin blocks pentobarbital-gated Cl− conductance. Neuroscience Research 6, 72–75. https://doi.org/10.1016/0168-0102(88)90007-7

Ito, M., Westheimer, G., Gilbert, C.D., 1998. Attention and Perceptual Learning Modulate Contextual Influences on Visual Perception. Neuron 20, 1191–1197. https://doi.org/10.1016/S0896-6273(00)80499-7

Jacob, V., Petreanu, L., Wright, N., Svoboda, K., Fox, K., 2012. Regular Spiking and Intrinsic Bursting Pyramidal Cells Show Orthogonal Forms of Experience-Dependent Plasticity in Layer V of Barrel Cortex. Neuron 73, 391–404. https://doi.org/10.1016/j.neuron.2011.11.034

Jarsky, T., Roxin, A., Kath, W.L., Spruston, N., 2005. Conditional dendritic spike propagation following distal synaptic activation of hippocampal CA1 pyramidal neurons. Nat Neurosci 8, 1667–1676. https://doi.org/10.1038/nn1599

Jedlicka, D., Zhen, L., 2023. PTSD is associated with self-perceived hearing handicap: An evaluation of comorbidities in Veterans with normal audiometric thresholds. J Am Acad Audiol. https://doi.org/10.1055/a-2015-8524

Jeon, Y.-W., Polich, J., 2003. Meta-analysis of P300 and schizophrenia: patients, paradigms, and practical implications. Psychophysiology 40, 684–701. https://doi.org/10.1111/1469-8986.00070

Jerde, T.A., Merriam, E.P., Riggall, A.C., Hedges, J.H., Curtis, C.E., 2012. Prioritized maps of space in human frontoparietal cortex. J Neurosci 32, 17382–17390. https://doi.org/10.1523/JNEUROSCI.3810-12.2012

Jia, H., Rochefort, N.L., Chen, X., Konnerth, A., 2010. Dendritic organization of sensory input to cortical neurons in vivo. Nature 464, 1307–1312. https://doi.org/10.1038/nature08947

Jiang, X., Shen, S., Cadwell, C.R., Berens, P., Sinz, F., Ecker, A.S., Patel, S., Tolias, A.S., 2015. Principles of connectivity among morphologically defined cell types in adult neocortex. Science 350, aac9462. https://doi.org/10.1126/science.aac9462

Joffe, M.E., Maksymetz, J., Luschinger, J.R., Dogra, S., Ferranti, A.S., Luessen, D.J., Gallinger, I.M., Xiang, Z., Branthwaite, H., Melugin, P.R., Williford, K.M., Centanni, S.W., Shields, B.C., Lindsley, C.W., Calipari, E.S., Siciliano, C.A., Niswender, C.M., Tadross, M.R., Winder, D.G., Conn, P.J., 2022. Acute restraint stress redirects prefrontal cortex circuit function through mGlu5 receptor plasticity on somatostatin-expressing interneurons. Neuron 110, 1068-1083.e5. https://doi.org/10.1016/j.neuron.2021.12.027

Jones, C., Watson, D., Fone, K., 2011. Animal models of schizophrenia. Br J Pharmacol 164, 1162–1194. https://doi.org/10.1111/j.1476-5381.2011.01386.x

Kaas, J.H., Lin, C.S., Wagor, E., 1977. Cortical projections of posterior parietal cortex in owl monkeys. Journal of Comparative Neurology 171, 387–407. https://doi.org/10.1002/cne.901710306

Kametani, H., Kawamura, H., 1990. Alterations in acetylcholine release in the rat hippocampus during sleep-wakefulness detected by intracerebral dialysis. Life Sciences 47, 421–426. https://doi.org/10.1016/0024-3205(90)90300-G

Kampasi, K., Stark, E., Seymour, J., Na, K., Winful, H.G., Buzsáki, G., Wise, K.D., Yoon, E., 2016. Fiberless multicolor neural optoelectrode for in vivo circuit analysis. Sci Rep 6, 30961. https://doi.org/10.1038/srep30961

Kasper, E.M., Larkman, A.U., Lübke, J., Blakemore, C., 1994. Pyramidal neurons in layer 5 of the rat visual cortex. I. Correlation among cell morphology, intrinsic electrophysiological

properties, and axon targets. Journal of Comparative Neurology 339, 459–474. https://doi.org/10.1002/cne.903390402
Kim, E.J., Juavinett, A.L., Kyubwa, E.M., Jacobs, M.W., Callaway, E.M., 2015. Three Types of Cortical Layer 5 Neurons That Differ in Brain-wide Connectivity and Function. Neuron 88, 1253–1267. https://doi.org/10.1016/j.neuron.2015.11.002
Kim, H.G., Beierlein, M., Connors, B.W., 1995. Inhibitory control of excitable dendrites in neocortex. J Neurophysiol 74, 1810–1814. https://doi.org/10.1152/jn.1995.74.4.1810
Kim, H.G., Connors, B.W., 1993. Apical dendrites of the neocortex: correlation between sodium- and calcium-dependent spiking and pyramidal cell morphology. J Neurosci 13, 5301–5311. https://doi.org/10.1523/JNEUROSCI.13-12-05301.1993
Kim, J., Wasserman, E.A., Castro, L., Freeman, J.H., 2016. Anterior cingulate cortex inactivation impairs rodent visual selective attention and prospective memory. Behav Neurosci 130, 75–90. https://doi.org/10.1037/bne0000117
Kiritani, T., Wickersham, I.R., Seung, H.S., Shepherd, G.M.G., 2012. Hierarchical Connectivity and Connection-Specific Dynamics in the Corticospinal–Corticostriatal Microcircuit in Mouse Motor Cortex. J Neurosci 32, 4992–5001. https://doi.org/10.1523/JNEUROSCI.4759-11.2012
Kishi, K.E., Kim, Y.S., Fukuda, M., Inoue, M., Kusakizako, T., Wang, P.Y., Ramakrishnan, C., Byrne, E.F.X., Thadhani, E., Paggi, J.M., Matsui, T.E., Yamashita, K., Nagata, T., Konno, M., Quirin, S., Lo, M., Benster, T., Uemura, T., Liu, K., Shibata, M., Nomura, N., Iwata, S., Nureki, O., Dror, R.O., Inoue, K., Deisseroth, K., Kato, H.E., 2022. Structural basis for channel conduction in the pump-like channelrhodopsin ChRmine. Cell 185, 672-689.e23. https://doi.org/10.1016/j.cell.2022.01.007
Klapoetke, N.C., Murata, Y., Kim, S.S., Pulver, S.R., Birdsey-Benson, A., Cho, Y.K., Morimoto, T.K., Chuong, A.S., Carpenter, E.J., Tian, Z., Wang, J., Xie, Y., Yan, Z., Zhang, Y., Chow, B.Y., Surek, B., Melkonian, M., Jayaraman, V., Constantine-Paton, M., Wong, G.K.-S., Boyden, E.S., 2014. Independent optical excitation of distinct neural populations. Nat Methods 11, 338–346. https://doi.org/10.1038/nmeth.2836
Koechlin, E., Basso, G., Pietrini, P., Panzer, S., Grafman, J., 1999. The role of the anterior prefrontal cortex in human cognition. Nature 399, 148–151. https://doi.org/10.1038/20178
Koenigs, M., Barbey, A.K., Postle, B.R., Grafman, J., 2009. Superior parietal cortex is critical for the manipulation of information in working memory. J Neurosci 29, 14980–14986. https://doi.org/10.1523/JNEUROSCI.3706-09.2009
Koike, H., Demars, M.P., Short, J.A., Nabel, E.M., Akbarian, S., Baxter, M.G., Morishita, H., 2016. Chemogenetic Inactivation of Dorsal Anterior Cingulate Cortex Neurons Disrupts Attentional Behavior in Mouse. Neuropsychopharmacol 41, 1014–1023. https://doi.org/10.1038/npp.2015.229
Kubo, T., Fukuda, K., Mikami, A., Maeda, A., Takahashi, H., Mishina, M., Haga, T., Haga, K., Ichiyama, A., Kangawa, K., Kojima, M., Matsuo, H., Hirose, T., Numa, S., 1986. Cloning, sequencing and expression of complementary DNA encoding the muscarinic acetylcholine receptor. Nature 323, 411–416. https://doi.org/10.1038/323411a0

Kwon, S.E., Yang, H., Minamisawa, G., O'Connor, D.H., 2016. Sensory and decision-related activity propagate in a cortical feedback loop during touch perception. Nat Neurosci 19, 1243–1249. https://doi.org/10.1038/nn.4356

Lachenmayer, M.L., Mürset, M., Antih, N., Debove, I., Muellner, J., Bompart, M., Schlaeppi, J.-A., Nowacki, A., You, H., Michelis, J.P., Dransart, A., Pollo, C., Deuschl, G., Krack, P., 2021. Subthalamic and pallidal deep brain stimulation for Parkinson's disease—meta-analysis of outcomes. npj Parkinsons Dis. 7, 1–10. https://doi.org/10.1038/s41531-021-00223-5

Lacquaniti, F., Guigon, E., Bianchi, L., Ferraina, S., Caminiti, R., 1995. Representing Spatial Information for Limb Movement: Role of Area 5 in the Monkey. Cereb Cortex 5, 391–409. https://doi.org/10.1093/cercor/5.5.391

Lafourcade, M., van der Goes, M.-S.H., Vardalaki, D., Brown, N.J., Voigts, J., Yun, D.H., Kim, M.E., Ku, T., Harnett, M.T., 2022. Differential dendritic integration of long-range inputs in association cortex via subcellular changes in synaptic AMPA-to-NMDA receptor ratio. Neuron 110, 1532-1546.e4. https://doi.org/10.1016/j.neuron.2022.01.025

Lamme, V.A., 1995. The neurophysiology of figure-ground segregation in primary visual cortex. J. Neurosci. 15, 1605–1615. https://doi.org/10.1523/JNEUROSCI.15-02-01605.1995

Larkman, A., Mason, A., 1990. Correlations between morphology and electrophysiology of pyramidal neurons in slices of rat visual cortex. I. Establishment of cell classes. J. Neurosci. 10, 1407–1414. https://doi.org/10.1523/JNEUROSCI.10-05-01407.1990

Larkman, A.U., 1991. Dendritic morphology of pyramidal neurones of the visual cortex of the rat: I. Branching patterns. Journal of Comparative Neurology 306, 307–319. https://doi.org/10.1002/cne.903060207

Larkum, M.E., Nevian, T., 2008. Synaptic clustering by dendritic signalling mechanisms. Current Opinion in Neurobiology, Signalling mechanisms 18, 321–331. https://doi.org/10.1016/j.conb.2008.08.013

Larkum, M.E., Petro, L.S., Sachdev, R.N.S., Muckli, L., 2018. A Perspective on Cortical Layering and Layer-Spanning Neuronal Elements. Frontiers in Neuroanatomy 12.

Larkum, M.E., Zhu, J.J., 2002. Signaling of Layer 1 and Whisker-Evoked Ca2+ and Na+ Action Potentials in Distal and Terminal Dendrites of Rat Neocortical Pyramidal Neurons In Vitro and In Vivo. J. Neurosci. 22, 6991–7005. https://doi.org/10.1523/JNEUROSCI.22-16-06991.2002

Larkum, M.E., Zhu, J.J., Sakmann, B., 1999. A new cellular mechanism for coupling inputs arriving at different cortical layers. Nature 398, 338–341. https://doi.org/10.1038/18686

Laubach, M., Amarante, L.M., Swanson, K., White, S.R., 2018. What, If Anything, Is Rodent Prefrontal Cortex? eNeuro 5. https://doi.org/10.1523/ENEURO.0315-18.2018

Lefort, S., Tomm, C., Floyd Sarria, J.-C., Petersen, C.C.H., 2009. The Excitatory Neuronal Network of the C2 Barrel Column in Mouse Primary Somatosensory Cortex. Neuron 61, 301–316. https://doi.org/10.1016/j.neuron.2008.12.020

Lei, Y.-T., Thuault, S.J., Launay, P., Margolskee, R.F., Kandel, E.R., Siegelbaum, S.A., 2014. Differential contribution of TRPM4 and TRPM5 nonselective cation channels to the slow afterdepolarization in mouse prefrontal cortex neurons. Front Cell Neurosci 8, 267. https://doi.org/10.3389/fncel.2014.00267

Lemon, N., Turner, R.W., 2000. Conditional Spike Backpropagation Generates Burst Discharge in a Sensory Neuron. Journal of Neurophysiology 84, 1519–1530. https://doi.org/10.1152/jn.2000.84.3.1519

Li, H., Li, Y., Lei, Z., Wang, K., Guo, A., 2013. Transformation of odor selectivity from projection neurons to single mushroom body neurons mapped with dual-color calcium imaging. Proceedings of the National Academy of Sciences 110, 12084–12089. https://doi.org/10.1073/pnas.1305857110

Li, L., Gratton, C., Yao, D., Knight, R.T., 2010. Role of frontal and parietal cortices in the control of bottom-up and top-down attention in humans. Brain Res 1344, 173–184. https://doi.org/10.1016/j.brainres.2010.05.016

Li, L., Ji, X., Liang, F., Li, Y., Xiao, Z., Tao, H.W., Zhang, L.I., 2014. A Feedforward Inhibitory Circuit Mediates Lateral Refinement of Sensory Representation in Upper Layer 2/3 of Mouse Primary Auditory Cortex. J. Neurosci. 34, 13670–13683. https://doi.org/10.1523/JNEUROSCI.1516-14.2014

Li, L., Lu, L., Ren, Y., Tang, G., Zhao, Y., Cai, X., Shi, Z., Ding, H., Liu, C., Cheng, D., Xie, Y., Wang, H., Fu, X., Yin, L., Luo, M., Sheng, X., 2022. Colocalized, bidirectional optogenetic modulations in freely behaving mice with a wireless dual-color optoelectronic probe. Nat Commun 13, 839. https://doi.org/10.1038/s41467-022-28539-7

Li, N., Chen, S., Guo, Z.V., Chen, H., Huo, Y., Inagaki, H.K., Chen, G., Davis, C., Hansel, D., Guo, C., Svoboda, K., 2019. Spatiotemporal constraints on optogenetic inactivation in cortical circuits. eLife 8, e48622. https://doi.org/10.7554/eLife.48622

Li, W., Piëch, V., Gilbert, C.D., 2004. Perceptual learning and top-down influences in primary visual cortex. Nat Neurosci 7, 651–657. https://doi.org/10.1038/nn1255

Lim, D., Mohajerani, M., LeDue, J., Boyd, J., Chen, S., Murphy, T., 2012. In vivo Large-Scale Cortical Mapping Using Channelrhodopsin-2 Stimulation in Transgenic Mice Reveals Asymmetric and Reciprocal Relationships between Cortical Areas. Frontiers in Neural Circuits 6.

Lin, J.Y., Knutsen, P.M., Muller, A., Kleinfeld, D., Tsien, R.Y., 2013. ReaChR: a red-shifted variant of channelrhodopsin enables deep transcranial optogenetic excitation. Nat Neurosci 16, 1499–1508. https://doi.org/10.1038/nn.3502

Lin, J.Y., Lin, M.Z., Steinbach, P., Tsien, R.Y., 2009. Characterization of engineered channelrhodopsin variants with improved properties and kinetics. Biophys J 96, 1803–1814. https://doi.org/10.1016/j.bpj.2008.11.034

Llinás, R., Nicholson, C., Freeman, J.A., Hillman, D.E., 1968. Dendritic spikes and their inhibition in alligator Purkinje cells. Science 160, 1132–1135. https://doi.org/10.1126/science.160.3832.1132

Llinás, R.R., Leznik, E., Urbano, F.J., 2002. Temporal binding via cortical coincidence detection of specific and nonspecific thalamocortical inputs: A voltage-dependent dye-imaging study in mouse brain slices. Proceedings of the National Academy of Sciences 99, 449–454. https://doi.org/10.1073/pnas.012604899

Lohuis, M.N.O., Marchesi, P., Pennartz, C.M.A., Olcese, U., 2022. Functional (ir)Relevance of Posterior Parietal Cortex during Audiovisual Change Detection. J. Neurosci. 42, 5229–5245. https://doi.org/10.1523/JNEUROSCI.2150-21.2022

Losonczy, A., Magee, J.C., 2006. Integrative properties of radial oblique dendrites in hippocampal CA1 pyramidal neurons. Neuron 50, 291–307. https://doi.org/10.1016/j.neuron.2006.03.016
Lur, G., Vinck, M.A., Tang, L., Cardin, J.A., Higley, M.J., 2016. Projection-Specific Visual Feature Encoding by Layer 5 Cortical Subnetworks. Cell Rep 14, 2538–2545. https://doi.org/10.1016/j.celrep.2016.02.050
Machens, C.K., Romo, R., Brody, C.D., 2005. Flexible control of mutual inhibition: a neural model of two-interval discrimination. Science 307, 1121–1124. https://doi.org/10.1126/science.1104171
Mackey, W.E., Devinsky, O., Doyle, W.K., Golfinos, J.G., Curtis, C.E., 2016. Human parietal cortex lesions impact the precision of spatial working memory. J Neurophysiol 116, 1049–1054. https://doi.org/10.1152/jn.00380.2016
Magee, J.C., 2000. Dendritic integration of excitatory synaptic input. Nat Rev Neurosci 1, 181–190. https://doi.org/10.1038/35044552
Mainen, Z.F., Sejnowski, T.J., 1996. Influence of dendritic structure on firing pattern in model neocortical neurons. Nature 382, 363–366. https://doi.org/10.1038/382363a0
Mangeot, S.D., Miller, L.J., McIntosh, D.N., McGrath-Clarke, J., Simon, J., Hagerman, R.J., Goldson, E., 2001. Sensory modulation dysfunction in children with attention-deficit-hyperactivity disorder. Developmental Medicine & Child Neurology 43, 399–406. https://doi.org/10.1111/j.1469-8749.2001.tb00228.x
Manor, Y., Gonczarowski, J., Segev, I., 1991. Propagation of action potentials along complex axonal trees. Model and implementation. Biophys J 60, 1411–1423. https://doi.org/10.1016/S0006-3495(91)82178-6
Marder, E., Abbott, L.F., Turrigiano, G.G., Liu, Z., Golowasch, J., 1996. Memory from the dynamics of intrinsic membrane currents. Proceedings of the National Academy of Sciences 93, 13481–13486. https://doi.org/10.1073/pnas.93.24.13481
Marder, E., Taylor, A.L., 2011. Multiple models to capture the variability in biological neurons and networks. Nat Neurosci 14, 133–138. https://doi.org/10.1038/nn.2735
Mardinly, A.R., Oldenburg, I.A., Pégard, N.C., Sridharan, S., Lyall, E.H., Chesnov, K., Brohawn, S.G., Waller, L., Adesnik, H., 2018. Precise multimodal optical control of neural ensemble activity. Nat Neurosci 21, 881–893. https://doi.org/10.1038/s41593-018-0139-8
Marek, S., Dosenbach, N.U.F., 2018. The frontoparietal network: function, electrophysiology, and importance of individual precision mapping. Dialogues Clin Neurosci 20, 133–140. https://doi.org/10.31887/DCNS.2018.20.2/smarek
Markov, N.T., Vezoli, J., Chameau, P., Falchier, A., Quilodran, R., Huissoud, C., Lamy, C., Misery, P., Giroud, P., Ullman, S., Barone, P., Dehay, C., Knoblauch, K., Kennedy, H., 2014. Anatomy of hierarchy: Feedforward and feedback pathways in macaque visual cortex. Journal of Comparative Neurology 522, 225–259. https://doi.org/10.1002/cne.23458
Marrosu, F., Portas, C., Mascia, M.S., Casu, M.A., Fà, M., Giagheddu, M., Imperato, A., Gessa, G.L., 1995. Microdialysis measurement of cortical and hippocampal acetylcholine release during sleep-wake cycle in freely moving cats. Brain Research 671, 329–332. https://doi.org/10.1016/0006-8993(94)01399-3
Marshel, J.H., Kim, Y.S., Machado, T.A., Quirin, S., Benson, B., Kadmon, J., Raja, C., Chibukhchyan, A., Ramakrishnan, C., Inoue, M., Shane, J.C., McKnight, D.J., Yoshizawa, S., Kato, H.E.,

Ganguli, S., Deisseroth, K., 2019. Cortical layer–specific critical dynamics triggering perception. Science 365, eaaw5202. https://doi.org/10.1126/science.aaw5202
Martínez, A., Anllo-Vento, L., Sereno, M.I., Frank, L.R., Buxton, R.B., Dubowitz, D.J., Wong, E.C., Hinrichs, H., Heinze, H.J., Hillyard, S.A., 1999. Involvement of striate and extrastriate visual cortical areas in spatial attention. Nature Neuroscience 2, 364–369. https://doi.org/10.1038/7274
Mason, A., Larkman, A., 1990. Correlations between morphology and electrophysiology of pyramidal neurons in slices of rat visual cortex. II. Electrophysiology. J. Neurosci. 10, 1415–1428. https://doi.org/10.1523/JNEUROSCI.10-05-01415.1990
McAdams, C.J., Maunsell, J.H.R., 1999. Effects of Attention on Orientation-Tuning Functions of Single Neurons in Macaque Cortical Area V4. J. Neurosci. 19, 431–441. https://doi.org/10.1523/JNEUROSCI.19-01-00431.1999
McMains, S., Kastner, S., 2011. Interactions of Top-Down and Bottom-Up Mechanisms in Human Visual Cortex. J. Neurosci. 31, 587–597. https://doi.org/10.1523/JNEUROSCI.3766-10.2011
Melancia, F., Trezza, V., 2018. Modelling fragile X syndrome in the laboratory setting: A behavioral perspective. Behavioural Brain Research 350, 149–163. https://doi.org/10.1016/j.bbr.2018.04.042
Meredith, M.A., Nemitz, J.W., Stein, B.E., 1987. Determinants of multisensory integration in superior colliculus neurons. I. Temporal factors. J. Neurosci. 7, 3215–3229. https://doi.org/10.1523/JNEUROSCI.07-10-03215.1987
Meredith, M.A., Stein, B.E., 1996. Spatial determinants of multisensory integration in cat superior colliculus neurons. J Neurophysiol 75, 1843–1857. https://doi.org/10.1152/jn.1996.75.5.1843
Meredith, M.A., Stein, B.E., 1983. Interactions among converging sensory inputs in the superior colliculus. Science 221, 389–391. https://doi.org/10.1126/science.6867718
Mermet-Joret, N., Moreno, A., Zbela, A., Ellendersen, B.E., Krauth, N., Philipsborn, A. von, Piriz, J., Lin, J.Y., Nabavi, S., 2021. Dual-color optical activation and suppression of neurons with high temporal precision. https://doi.org/10.1101/2021.05.05.442824
Mesulam, M.M., 1999. Spatial attention and neglect: parietal, frontal and cingulate contributions to the mental representation and attentional targeting of salient extrapersonal events. Philos Trans R Soc Lond B Biol Sci 354, 1325–1346.
Metherate, R., Ashe, J., 1993. Ionic flux contributions to neocortical slow waves and nucleus basalis- mediated activation: whole-cell recordings in vivo. J Neurosci 13, 5312–5323. https://doi.org/10.1523/JNEUROSCI.13-12-05312.1993
Milescu, L.S., Yamanishi, T., Ptak, K., Smith, J.C., 2010. Kinetic Properties and Functional Dynamics of Sodium Channels during Repetitive Spiking in a Slow Pacemaker Neuron. J. Neurosci. 30, 12113–12127. https://doi.org/10.1523/JNEUROSCI.0445-10.2010
Miller, E.K., Cohen, J.D., 2001. An integrative theory of prefrontal cortex function. Annu Rev Neurosci 24, 167–202. https://doi.org/10.1146/annurev.neuro.24.1.167
Milner, B., 1963. Effects of Different Brain Lesions on Card Sorting: The Role of the Frontal Lobes. Arch Neurol 9, 90. https://doi.org/10.1001/archneur.1963.00460070100010
Moberg, P.J., Arnold, S.E., Doty, R.L., Gur, R.E., Balderston, C.C., Roalf, D.R., Gur, R.C., Kohler, C.G., Kanes, S.J., Siegel, S.J., Turetsky, B.I., 2006. Olfactory functioning in schizophrenia:

relationship to clinical, neuropsychological, and volumetric MRI measures. J Clin Exp Neuropsychol 28, 1444–1461. https://doi.org/10.1080/13803390500434409
Mohan, H., Gallero-Salas, Y., Carta, S., Sacramento, J., Laurenczy, B., Sumanovski, L.T., de Kock, C.P.J., Helmchen, F., Sachidhanandam, S., 2018. Sensory representation of an auditory cued tactile stimulus in the posterior parietal cortex of the mouse. Sci Rep 8, 7739. https://doi.org/10.1038/s41598-018-25891-x
Moran, J., Desimone, R., 1985. Selective Attention Gates Visual Processing in the Extrastriate Cortex. Science 229, 782–784. https://doi.org/10.1126/science.4023713
Morishima, M., Kobayashi, Kenta, Kato, S., Kobayashi, Kazuto, Kawaguchi, Y., 2017. Segregated Excitatory–Inhibitory Recurrent Subnetworks in Layer 5 of the Rat Frontal Cortex. Cerebral Cortex 27, 5846–5857. https://doi.org/10.1093/cercor/bhx276
Morishima, M., Morita, K., Kubota, Y., Kawaguchi, Y., 2011. Highly Differentiated Projection-Specific Cortical Subnetworks. Journal of Neuroscience 31, 10380–10391. https://doi.org/10.1523/JNEUROSCI.0772-11.2011
Morishima, Y., Akaishi, R., Yamada, Y., Okuda, J., Toma, K., Sakai, K., 2009. Task-specific signal transmission from prefrontal cortex in visual selective attention. Nat Neurosci 12, 85–91. https://doi.org/10.1038/nn.2237
Murphy, A.P., Leopold, D.A., Humphreys, G.W., Welchman, A.E., 2016. Lesions to right posterior parietal cortex impair visual depth perception from disparity but not motion cues. Philos Trans R Soc Lond B Biol Sci 371, 20150263. https://doi.org/10.1098/rstb.2015.0263
Musall, S., Sun, X.R., Mohan, H., An, X., Gluf, S., Li, S.-J., Drewes, R., Cravo, E., Lenzi, I., Yin, C., Kampa, B.M., Churchland, A.K., 2023. Pyramidal cell types drive functionally distinct cortical activity patterns during decision-making. Nat Neurosci 26, 495–505. https://doi.org/10.1038/s41593-022-01245-9
Nagel, G., Brauner, M., Liewald, J.F., Adeishvili, N., Bamberg, E., Gottschalk, A., 2005. Light activation of channelrhodopsin-2 in excitable cells of Caenorhabditis elegans triggers rapid behavioral responses. Curr Biol 15, 2279–2284. https://doi.org/10.1016/j.cub.2005.11.032
Nagel, G., Ollig, D., Fuhrmann, M., Kateriya, S., Musti, A.M., Bamberg, E., Hegemann, P., 2002. Channelrhodopsin-1: a light-gated proton channel in green algae. Science 296, 2395–2398. https://doi.org/10.1126/science.1072068
Nagel, G., Szellas, T., Huhn, W., Kateriya, S., Adeishvili, N., Berthold, P., Ollig, D., Hegemann, P., Bamberg, E., 2003. Channelrhodopsin-2, a directly light-gated cation-selective membrane channel. Proceedings of the National Academy of Sciences 100, 13940–13945. https://doi.org/10.1073/pnas.1936192100
Naka, A., Adesnik, H., 2016. Inhibitory Circuits in Cortical Layer 5. Frontiers in Neural Circuits 10.
Nakamura, F., Kato, M., Kameyama, K., Nukada, T., Haga, T., Kato, H., Takenawa, T., Kikkawa, U., 1995. Characterization of Gq family G proteins GL1 alpha (G14 alpha), GL2 alpha (G11 alpha), and Gq alpha expressed in the baculovirus-insect cell system. J Biol Chem 270, 6246–6253. https://doi.org/10.1074/jbc.270.11.6246
Narayanan, N.S., Laubach, M., 2006. Top-Down Control of Motor Cortex Ensembles by Dorsomedial Prefrontal Cortex. Neuron 52, 921–931. https://doi.org/10.1016/j.neuron.2006.10.021

Nauer, R.K., Whiteman, A.S., Dunne, M.F., Stern, C.E., Schon, K., 2015. Hippocampal subfield and medial temporal cortical persistent activity during working memory reflects ongoing encoding. Frontiers in Systems Neuroscience 9.

Navaroli, V.L., Zhao, Y., Boguszewski, P., Brown, T.H., 2012. Muscarinic receptor activation enables persistent firing in pyramidal neurons from superficial layers of dorsal perirhinal cortex. Hippocampus 22, 1392–1404. https://doi.org/10.1002/hipo.20975

Nozawa, G., Reuter-Lorenz, P.A., Hughes, H.C., 1994. Parallel and serial processes in the human oculomotor system: bimodal integration and express saccades. Biol. Cybern. 72, 19–34. https://doi.org/10.1007/BF00206235

O'Connor, D.H., Fukui, M.M., Pinsk, M.A., Kastner, S., 2002. Attention modulates responses in the human lateral geniculate nucleus. Nat Neurosci 5, 1203–1209. https://doi.org/10.1038/nn957

Oda, K., Vierock, J., Oishi, S., Rodriguez-Rozada, S., Taniguchi, R., Yamashita, K., Wiegert, J.S., Nishizawa, T., Hegemann, P., Nureki, O., 2018. Crystal structure of the red light-activated channelrhodopsin Chrimson. Nat Commun 9, 3949. https://doi.org/10.1038/s41467-018-06421-9

Ohlemiller, K.K., Jones, S.M., Johnson, K.R., 2016. Application of Mouse Models to Research in Hearing and Balance. J Assoc Res Otolaryngol 17, 493–523. https://doi.org/10.1007/s10162-016-0589-1

Olatunji, B.O., Armstrong, T., Bilsky, S.A., Zhao, M., 2015. Threat modulation of visual search efficiency in PTSD: A comparison of distinct stimulus categories. Psychiatry Research 229, 975–982. https://doi.org/10.1016/j.psychres.2015.05.090

Olcese, U., Iurilli, G., Medini, P., 2013. Cellular and synaptic architecture of multisensory integration in the mouse neocortex. Neuron 79, 579–593. https://doi.org/10.1016/j.neuron.2013.06.010

Olsen, R.K., Nichols, E.A., Chen, J., Hunt, J.F., Glover, G.H., Gabrieli, J.D.E., Wagner, A.D., 2009. Performance-Related Sustained and Anticipatory Activity in Human Medial Temporal Lobe during Delayed Match-to-Sample. J. Neurosci. 29, 11880–11890. https://doi.org/10.1523/JNEUROSCI.2245-09.2009

Olson, I.R., Chun, M.M., Allison, T., 2001. Contextual guidance of attention: Human intracranial event-related potential evidence for feedback modulation in anatomically early temporally late stages of visual processing. Brain 124, 1417–1425. https://doi.org/10.1093/brain/124.7.1417

Osaka, N., Osaka, M., Kondo, H., Morishita, M., Fukuyama, H., Shibasaki, H., 2004. The neural basis of executive function in working memory: an fMRI study based on individual differences. Neuroimage 21, 623–631. https://doi.org/10.1016/j.neuroimage.2003.09.069

Oswald, M., Tantirigama, M., Sonntag, I., Hughes, S., Empson, R., 2013. Diversity of layer 5 projection neurons in the mouse motor cortex. Frontiers in Cellular Neuroscience 7.

Otsuka, Y., Osaka, N., Morishita, M., Kondo, H., Osaka, M., 2006. Decreased activation of anterior cingulate cortex in the working memory of the elderly. Neuroreport 17, 1479–1482. https://doi.org/10.1097/01.wnr.0000236852.63092.9f

Packer, A.M., Russell, L.E., Dalgleish, H.W.P., Häusser, M., 2015. Simultaneous all-optical manipulation and recording of neural circuit activity with cellular resolution in vivo. Nat Methods 12, 140–146. https://doi.org/10.1038/nmeth.3217

Palmer, L.M., Shai, A.S., Reeve, J.E., Anderson, H.L., Paulsen, O., Larkum, M.E., 2014. NMDA spikes enhance action potential generation during sensory input. Nat Neurosci 17, 383–390. https://doi.org/10.1038/nn.3646

Palomero-Gallagher, N., Zilles, K., 2015. Isocortex, in: The Rat Nervous System. Elsevier, pp. 601–625. https://doi.org/10.1016/B978-0-12-374245-2.00022-X

Papoutsi, A., Sidiropoulou, K., Cutsuridis, V., Poirazi, P., 2013. Induction and modulation of persistent activity in a layer V PFC microcircuit model. Frontiers in Neural Circuits 7.

Pardo, J.V., Pardo, P.J., Janer, K.W., Raichle, M.E., 1990. The anterior cingulate cortex mediates processing selection in the Stroop attentional conflict paradigm. Proceedings of the National Academy of Sciences 87, 256–259. https://doi.org/10.1073/pnas.87.1.256

Park, J., Phillips, J.W., Guo, J.-Z., Martin, K.A., Hantman, A.W., Dudman, J.T., 2022. Motor cortical output for skilled forelimb movement is selectively distributed across projection neuron classes. Science Advances 8, eabj5167. https://doi.org/10.1126/sciadv.abj5167

Peng, H., Xie, P., Liu, L., Kuang, X., Wang, Yimin, Qu, L., Gong, H., Jiang, S., Li, A., Ruan, Z., Ding, L., Yao, Z., Chen, C., Chen, M., Daigle, T.L., Dalley, R., Ding, Z., Duan, Y., Feiner, A., He, P., Hill, C., Hirokawa, K.E., Hong, G., Huang, L., Kebede, S., Kuo, H.-C., Larsen, R., Lesnar, P., Li, L., Li, Q., Li, X., Li, Yaoyao, Li, Yuanyuan, Liu, A., Lu, D., Mok, S., Ng, L., Nguyen, T.N., Ouyang, Q., Pan, J., Shen, E., Song, Y., Sunkin, S.M., Tasic, B., Veldman, M.B., Wakeman, W., Wan, W., Wang, P., Wang, Q., Wang, T., Wang, Yaping, Xiong, F., Xiong, W., Xu, W., Ye, M., Yin, L., Yu, Y., Yuan, Jia, Yuan, Jing, Yun, Z., Zeng, S., Zhang, S., Zhao, S., Zhao, Z., Zhou, Z., Huang, Z.J., Esposito, L., Hawrylycz, M.J., Sorensen, S.A., Yang, X.W., Zheng, Y., Gu, Z., Xie, W., Koch, C., Luo, Q., Harris, J.A., Wang, Yun, Zeng, H., 2021. Morphological diversity of single neurons in molecularly defined cell types. Nature 598, 174–181. https://doi.org/10.1038/s41586-021-03941-1

Pesaran, B., Nelson, M.J., Andersen, R.A., 2008. Free choice activates a decision circuit between frontal and parietal cortex. Nature 453, 406–409. https://doi.org/10.1038/nature06849

Petreanu, L., Huber, D., Sobczyk, A., Svoboda, K., 2007. Channelrhodopsin-2-assisted circuit mapping of long-range callosal projections. Nat Neurosci 10, 663–668. https://doi.org/10.1038/nn1891

Petreanu, L., Mao, T., Sternson, S.M., Svoboda, K., 2009. The subcellular organization of neocortical excitatory connections. Nature 457, 1142–1145. https://doi.org/10.1038/nature07709

Pho, G.N., Goard, M.J., Woodson, J., Crawford, B., Sur, M., 2018. Task-dependent representations of stimulus and choice in mouse parietal cortex. Nat Commun 9, 2596. https://doi.org/10.1038/s41467-018-05012-y

Pinsk, M.A., Doniger, G.M., Kastner, S., 2004. Push-Pull Mechanism of Selective Attention in Human Extrastriate Cortex. Journal of Neurophysiology 92, 622–629. https://doi.org/10.1152/jn.00974.2003

Polsky, A., Mel, B.W., Schiller, J., 2004. Computational subunits in thin dendrites of pyramidal cells. Nat Neurosci 7, 621–627. https://doi.org/10.1038/nn1253

Prasad, A.A., Xie, C., Chaichim, C., Nguyen, J.H., McClusky, H.E., Killcross, S., Power, J.M., McNally, G.P., 2020. Complementary Roles for Ventral Pallidum Cell Types and Their Projections in Relapse. J. Neurosci. 40, 880–893. https://doi.org/10.1523/JNEUROSCI.0262-19.2019

Pressler, R.T., Strowbridge, B.W., 2006. Blanes cells mediate persistent feedforward inhibition onto granule cells in the olfactory bulb. Neuron 49, 889–904. https://doi.org/10.1016/j.neuron.2006.02.019

Preuss, T.M., 1995. Do Rats Have Prefrontal Cortex? The Rose-Woolsey-Akert Program Reconsidered. Journal of Cognitive Neuroscience 7, 1–24. https://doi.org/10.1162/jocn.1995.7.1.1

Prigge, M., Schneider, F., Tsunoda, S.P., Shilyansky, C., Wietek, J., Deisseroth, K., Hegemann, P., 2012. Color-tuned channelrhodopsins for multiwavelength optogenetics. J Biol Chem 287, 31804–31812. https://doi.org/10.1074/jbc.M112.391185

Projection :: Allen Brain Atlas: Mouse Connectivity [WWW Document], n.d. URL http://connectivity.brain-map.org/projection (accessed 8.24.23).

Rahman, J., Berger, T., 2011. Persistent activity in layer 5 pyramidal neurons following cholinergic activation of mouse primary cortices. European Journal of Neuroscience 34, 22–30. https://doi.org/10.1111/j.1460-9568.2011.07736.x

Rainer, G., Asaad, W.F., Miller, E.K., 1998. Selective representation of relevant information by neurons in the primate prefrontal cortex. Nature 393, 577–579. https://doi.org/10.1038/31235

Ranck, J.B., 1975. Which elements are excited in electrical stimulation of mammalian central nervous system: a review. Brain Res 98, 417–440. https://doi.org/10.1016/0006-8993(75)90364-9

Raposo, D., Sheppard, J.P., Schrater, P.R., Churchland, A.K., 2012. Multisensory Decision-Making in Rats and Humans. J. Neurosci. 32, 3726–3735. https://doi.org/10.1523/JNEUROSCI.4998-11.2012

Regev, T.I., Winawer, J., Gerber, E.M., Knight, R.T., Deouell, L.Y., 2018. Human posterior parietal cortex responds to visual stimuli as early as peristriate occipital cortex. European Journal of Neuroscience 48, 3567–3582. https://doi.org/10.1111/ejn.14164

Remy, S., Spruston, N., 2007. Dendritic spikes induce single-burst long-term potentiation. Proceedings of the National Academy of Sciences 104, 17192–17197. https://doi.org/10.1073/pnas.0707919104

Rens, N., Bode, S., Burianová, H., Cunnington, R., 2017. Proactive Recruitment of Frontoparietal and Salience Networks for Voluntary Decisions. Front Hum Neurosci 11, 610. https://doi.org/10.3389/fnhum.2017.00610

Rickgauer, J.P., Deisseroth, K., Tank, D.W., 2014. Simultaneous cellular-resolution optical perturbation and imaging of place cell firing fields. Nat Neurosci 17, 1816–1824. https://doi.org/10.1038/nn.3866

Rindner, D.J., Proddutur, A., Lur, G., 2022. Cell-type-specific integration of feedforward and feedback synaptic inputs in the posterior parietal cortex. Neuron 110, 3760-3773.e5. https://doi.org/10.1016/j.neuron.2022.08.019

Ro, T., Rorden, C., Driver, J., Rafal, R., 2001. Ipsilesional Biases in Saccades but not Perception after Lesions of the Human Inferior Parietal Lobule. Journal of Cognitive Neuroscience 13, 920–929. https://doi.org/10.1162/089892901753165836

Rockland, K.S., Pandya, D.N., 1979. Laminar origins and terminations of cortical connections of the occipital lobe in the rhesus monkey. Brain Research 179, 3–20. https://doi.org/10.1016/0006-8993(79)90485-2

Rost, B.R., Schneider-Warme, F., Schmitz, D., Hegemann, P., 2017. Optogenetic Tools for Subcellular Applications in Neuroscience. Neuron 96, 572–603. https://doi.org/10.1016/j.neuron.2017.09.047

Rowe, J., Hughes, L., Eckstein, D., Owen, A.M., 2008. Rule-selection and action-selection have a shared neuroanatomical basis in the human prefrontal and parietal cortex. Cereb Cortex 18, 2275–2285. https://doi.org/10.1093/cercor/bhm249

Salazar, R.F., Dotson, N.M., Bressler, S.L., Gray, C.M., 2012. Content-specific fronto-parietal synchronization during visual working memory. Science 338, 1097–1100. https://doi.org/10.1126/science.1224000

Sanford, R.N., 1936. The effects of abstinence from food upon imaginal processes: a preliminary experiment. The Journal of Psychology: Interdisciplinary and Applied 2, 129–136. https://doi.org/10.1080/00223980.1936.9917447

Sarma, A., Masse, N.Y., Wang, X.-J., Freedman, D.J., 2016. Task-specific versus generalized mnemonic representations in parietal and prefrontal cortices. Nat Neurosci 19, 143–149. https://doi.org/10.1038/nn.4168

Schild, L.C., Glauser, D.A., 2015. Dual Color Neural Activation and Behavior Control with Chrimson and CoChR in Caenorhabditis elegans. Genetics 200, 1029–1034. https://doi.org/10.1534/genetics.115.177956

Schiller, J., Major, G., Koester, H.J., Schiller, Y., 2000. NMDA spikes in basal dendrites of cortical pyramidal neurons. Nature 404, 285–289. https://doi.org/10.1038/35005094

Schiller, J., Schiller, Y., Stuart, G., Sakmann, B., 1997. Calcium action potentials restricted to distal apical dendrites of rat neocortical pyramidal neurons. J Physiol 505 (Pt 3), 605–616. https://doi.org/10.1111/j.1469-7793.1997.605ba.x

Schon, K., Hasselmo, M.E., LoPresti, M.L., Tricarico, M.D., Stern, C.E., 2004. Persistence of Parahippocampal Representation in the Absence of Stimulus Input Enhances Long-Term Encoding: A Functional Magnetic Resonance Imaging Study of Subsequent Memory after a Delayed Match-to-Sample Task. J. Neurosci. 24, 11088–11097. https://doi.org/10.1523/JNEUROSCI.3807-04.2004

Schulz, J.M., Knoflach, F., Hernandez, M.-C., Bischofberger, J., 2018. Dendrite-targeting interneurons control synaptic NMDA-receptor activation via nonlinear α5-GABAA receptors. Nat Commun 9, 3576. https://doi.org/10.1038/s41467-018-06004-8

Seamans, J.K., Floresco, S.B., Phillips, A.G., 1995. Functional differences between the prelimbic and anterior cingulate regions of the rat prefrontal cortex. Behavioral Neuroscience 109, 1063–1073. https://doi.org/10.1037/0735-7044.109.6.1063

Seidenthal, M., Jánosi, B., Rosenkranz, N., Schuh, N., Elvers, N., Willoughby, M., Zhao, X., Gottschalk, A., 2023. pOpsicle: An all-optical reporter system for synaptic vesicle recycling combining pH-sensitive fluorescent proteins with optogenetic manipulation of neuronal activity. Frontiers in Cellular Neuroscience 17.

Serences, J.T., Schwarzbach, J., Courtney, S.M., Golay, X., Yantis, S., 2004. Control of object-based attention in human cortex. Cereb Cortex 14, 1346–1357. https://doi.org/10.1093/cercor/bhh095

Sereno, M.I., Pitzalis, S., Martinez, A., 2001. Mapping of Contralateral Space in Retinotopic Coordinates by a Parietal Cortical Area in Humans. Science 294, 1350–1354. https://doi.org/10.1126/science.1063695

Shadlen, M.N., Newsome, W.T., 2001. Neural Basis of a Perceptual Decision in the Parietal Cortex (Area LIP) of the Rhesus Monkey. Journal of Neurophysiology 86, 1916–1936. https://doi.org/10.1152/jn.2001.86.4.1916

Shao, Z., Burkhalter, A., 1996. Different Balance of Excitation and Inhibition in Forward and Feedback Circuits of Rat Visual Cortex. J. Neurosci. 16, 7353–7365. https://doi.org/10.1523/JNEUROSCI.16-22-07353.1996

Sheffield, J.M., Repovs, G., Harms, M.P., Carter, C.S., Gold, J.M., MacDonald, A.W., Daniel Ragland, J., Silverstein, S.M., Godwin, D., Barch, D.M., 2015. Fronto-parietal and cingulo-opercular network integrity and cognition in health and schizophrenia. Neuropsychologia 73, 82–93. https://doi.org/10.1016/j.neuropsychologia.2015.05.006

Shelton, A.M., Oliver, D.K., Grimstvedt, J.S., Lazarte, I.P., Kapoor, I., Swann, J.A., Ashcroft, C.A., Williams, S.N., Conway, N., Robinson, A., Kentros, C.G., Witter, M.P., Butt, S.J.B., Packer, A.M., 2022. Single neurons and networks in the claustrum integrate input from widespread cortical sources. https://doi.org/10.1101/2022.05.06.490864

Shpak, G., Zylbertal, A., Yarom, Y., Wagner, S., 2012. Calcium-Activated Sustained Firing Responses Distinguish Accessory from Main Olfactory Bulb Mitral Cells. J Neurosci 32, 6251–6262. https://doi.org/10.1523/JNEUROSCI.4397-11.2012

Smith, S.L., Smith, I.T., Branco, T., Häusser, M., 2013. Dendritic spikes enhance stimulus selectivity in cortical neurons in vivo. Nature 503, 115–120. https://doi.org/10.1038/nature12600

Snyder, J., Gregg, M., Weintraub, D., Alain, C., 2012. Attention, Awareness, and the Perception of Auditory Scenes. Frontiers in Psychology 3.

Snyder, L.H., Batista, A.P., Andersen, R.A., 1997. Coding of intention in the posterior parietal cortex. Nature 386, 167–170. https://doi.org/10.1038/386167a0

Spencer, D.G., Pontecorvo, M.J., Heise, G.A., 1985. Central cholinergic involvement in working memory: Effects of scopolamine on continuous nonmatching and discrimination performance in the rat. Behavioral Neuroscience 99, 1049–1065. https://doi.org/10.1037/0735-7044.99.6.1049

Spitzer, H., Desimone, R., Moran, J., 1988. Increased Attention Enhances Both Behavioral and Neuronal Performance. Science 240, 338–340. https://doi.org/10.1126/science.3353728

Stadler, K., Bierwirth, C., Stoenica, L., Battefeld, A., Reetz, O., Mix, E., Schuchmann, S., Velmans, T., Rosenberger, K., Bräuer, A.U., Lehnardt, S., Nitsch, R., Budt, M., Wolff, T., Kole, M.H.P., Strauss, U., 2014. Elevation in Type I Interferons Inhibits HCN1 and Slows Cortical Neuronal Oscillations. Cerebral Cortex 24, 199–210. https://doi.org/10.1093/cercor/bhs305

Stoet, G., Snyder, L.H., 2004. Single neurons in posterior parietal cortex of monkeys encode cognitive set. Neuron 42, 1003–1012. https://doi.org/10.1016/j.neuron.2004.06.003

Stuart, G.J., Spruston, N., 2015. Dendritic integration: 60 years of progress. Nat Neurosci 18, 1713–1721. https://doi.org/10.1038/nn.4157

Su, H., Alroy, G., Kirson, E.D., Yaari, Y., 2001. Extracellular Calcium Modulates Persistent Sodium Current-Dependent Burst-Firing in Hippocampal Pyramidal Neurons. J. Neurosci. 21, 4173–4182. https://doi.org/10.1523/JNEUROSCI.21-12-04173.2001

Sun, Y.J., Kim, Y.-J., Ibrahim, L.A., Tao, H.W., Zhang, L.I., 2013. Synaptic Mechanisms Underlying Functional Dichotomy between Intrinsic-Bursting and Regular-Spiking Neurons in Auditory Cortical Layer 5. J. Neurosci. 33, 5326–5339. https://doi.org/10.1523/JNEUROSCI.4810-12.2013

Suzuki, M., Gottlieb, J., 2013. Distinct neural mechanisms of distractor suppression in the frontal and parietal lobe. Nat Neurosci 16, 98–104. https://doi.org/10.1038/nn.3282

Suzuki, M., Larkum, M.E., 2017. Dendritic calcium spikes are clearly detectable at the cortical surface. Nat Commun 8, 276. https://doi.org/10.1038/s41467-017-00282-4

Szczepanski, S.M., Konen, C.S., Kastner, S., 2010. Mechanisms of spatial attention control in frontal and parietal cortex. J Neurosci 30, 148–160. https://doi.org/10.1523/JNEUROSCI.3862-09.2010

Takahashi, H., Magee, J.C., 2009. Pathway Interactions and Synaptic Plasticity in the Dendritic Tuft Regions of CA1 Pyramidal Neurons. Neuron 62, 102–111. https://doi.org/10.1016/j.neuron.2009.03.007

Takahashi, N., Ebner, C., Sigl-Glöckner, J., Moberg, S., Nierwetberg, S., Larkum, M.E., 2020. Active dendritic currents gate descending cortical outputs in perception. Nat Neurosci 23, 1277–1285. https://doi.org/10.1038/s41593-020-0677-8

Tanaka, H., Hachisuka, K., Ogata, H., 1999. Sound lateralisation in patients with left or right cerebral hemispheric lesions: relation with unilateral visuospatial neglect. J Neurol Neurosurg Psychiatry 67, 481–486.

Tang, L., Higley, M.J., 2020. Layer 5 Circuits in V1 Differentially Control Visuomotor Behavior. Neuron 105, 346-354.e5. https://doi.org/10.1016/j.neuron.2019.10.014

Tasic, B., Yao, Z., Graybuck, L.T., Smith, K.A., Nguyen, T.N., Bertagnolli, D., Goldy, J., Garren, E., Economo, M.N., Viswanathan, S., Penn, O., Bakken, T., Menon, V., Miller, J., Fong, O., Hirokawa, K.E., Lathia, K., Rimorin, C., Tieu, M., Larsen, R., Casper, T., Barkan, E., Kroll, M., Parry, S., Shapovalova, N.V., Hirschstein, D., Pendergraft, J., Sullivan, H.A., Kim, T.K., Szafer, A., Dee, N., Groblewski, P., Wickersham, I., Cetin, A., Harris, J.A., Levi, B.P., Sunkin, S.M., Madisen, L., Daigle, T.L., Looger, L., Bernard, A., Phillips, J., Lein, E., Hawrylycz, M., Svoboda, K., Jones, A.R., Koch, C., Zeng, H., 2018. Shared and distinct transcriptomic cell types across neocortical areas. Nature 563, 72–78. https://doi.org/10.1038/s41586-018-0654-5

Thimm, M., Weidner, R., Fink, G.R., Sturm, W., 2012. Neural mechanisms underlying freedom to choose an object. Hum Brain Mapp 33, 2686–2693. https://doi.org/10.1002/hbm.21393

Thuault, S.J., Malleret, G., Constantinople, C.M., Nicholls, R., Chen, I., Zhu, J., Panteleyev, A., Vronskaya, S., Nolan, M.F., Bruno, R., Siegelbaum, S.A., Kandel, E.R., 2013. Prefrontal cortex HCN1 channels enable intrinsic persistent neural firing and executive memory function. J Neurosci 33, 13583–13599. https://doi.org/10.1523/JNEUROSCI.2427-12.2013

Tigges, J., Tigges, M., Perachio, A.A., 1977. Complementary laminar terminations of afferents to area 17 originating in area 18 and in the lateral geniculate nucleus in squirrel monkey. Journal of Comparative Neurology 176, 87–100. https://doi.org/10.1002/cne.901760106

Todd, J.J., Marois, R., 2004. Capacity limit of visual short-term memory in human posterior parietal cortex. Nature 428, 751–754. https://doi.org/10.1038/nature02466
Totah, N.K.B., Kim, Y.B., Homayoun, H., Moghaddam, B., 2009. Anterior cingulate neurons represent errors and preparatory attention within the same behavioral sequence. J Neurosci 29, 6418–6426. https://doi.org/10.1523/JNEUROSCI.1142-09.2009
Toth, L.J., Assad, J.A., 2002. Dynamic coding of behaviourally relevant stimuli in parietal cortex. Nature 415, 165–168. https://doi.org/10.1038/415165a
Tran-Van-Minh, A., Abrahamsson, T., Cathala, L., DiGregorio, D.A., 2016. Differential Dendritic Integration of Synaptic Potentials and Calcium in Cerebellar Interneurons. Neuron 91, 837–850. https://doi.org/10.1016/j.neuron.2016.07.029
Traub, R.D., Wong, R.K., Miles, R., Michelson, H., 1991. A model of a CA3 hippocampal pyramidal neuron incorporating voltage-clamp data on intrinsic conductances. J Neurophysiol 66, 635–650. https://doi.org/10.1152/jn.1991.66.2.635
Treue, S., Trujillo, J.C.M., 1999. Feature-based attention influences motion processing gain in macaque visual cortex. Nature 399, 575–579. https://doi.org/10.1038/21176
Vélez-Fort, M., Rousseau, C.V., Niedworok, C.J., Wickersham, I.R., Rancz, E.A., Brown, A.P.Y., Strom, M., Margrie, T.W., 2014. The Stimulus Selectivity and Connectivity of Layer Six Principal Cells Reveals Cortical Microcircuits Underlying Visual Processing. Neuron 84, 238. https://doi.org/10.1016/j.neuron.2014.09.026
Vidyasagar, T.R., 1998. Gating of neuronal responses in macaque primary visual cortex by an attentional spotlight. NeuroReport 9, 1947.
Vierock, J., Rodriguez-Rozada, S., Dieter, A., Pieper, F., Sims, R., Tenedini, F., Bergs, A.C.F., Bendifallah, I., Zhou, F., Zeitzschel, N., Ahlbeck, J., Augustin, S., Sauter, K., Papagiakoumou, E., Gottschalk, A., Soba, P., Emiliani, V., Engel, A.K., Hegemann, P., Wiegert, J.S., 2021. BiPOLES is an optogenetic tool developed for bidirectional dual-color control of neurons. Nat Commun 12, 4527. https://doi.org/10.1038/s41467-021-24759-5
Vugt, B. van, Kerkoerle, T. van, Vartak, D., Roelfsema, P.R., 2020. The contribution of AMPA and NMDA receptors to persistent firing in the dorsolateral prefrontal cortex in working memory. J. Neurosci. https://doi.org/10.1523/JNEUROSCI.2121-19.2020
Waldton, S., 1974. Clinical Observations of Impaired Cranial Nerve Function in Senile Dementia. Acta Psychiatrica Scandinavica 50, 539–547. https://doi.org/10.1111/j.1600-0447.1974.tb09714.x
Wall, N.R., Parra, M.D.L., Sorokin, J.M., Taniguchi, H., Huang, Z.J., Callaway, E.M., 2016. Brain-Wide Maps of Synaptic Input to Cortical Interneurons. J. Neurosci. 36, 4000–4009. https://doi.org/10.1523/JNEUROSCI.3967-15.2016
Wall, N.R., Wickersham, I.R., Cetin, A., De La Parra, M., Callaway, E.M., 2010. Monosynaptic circuit tracing in vivo through Cre-dependent targeting and complementation of modified rabies virus. Proceedings of the National Academy of Sciences 107, 21848–21853. https://doi.org/10.1073/pnas.1011756107
Wallace, M.T., Meredith, M.A., Stein, B.E., 1992. Integration of multiple sensory modalities in cat cortex. Exp Brain Res 91, 484–488. https://doi.org/10.1007/BF00227844

Walter, E., Dassonville, P., 2008. VISUOSPATIAL CONTEXTUAL PROCESSING IN THE PARIETAL CORTEX: AN FMRI INVESTIGATION OF THE INDUCED ROELOFS EFFECT. Neuroimage 42, 1686–1697. https://doi.org/10.1016/j.neuroimage.2008.06.016

Wang, X.-J., 1999. Synaptic Basis of Cortical Persistent Activity: the Importance of NMDA Receptors to Working Memory. J. Neurosci. 19, 9587–9603. https://doi.org/10.1523/JNEUROSCI.19-21-09587.1999

Warren, S.G., Yacoub, E., Ghose, G.M., 2014. Featural and temporal attention selectively enhance task-appropriate representations in human primary visual cortex. Nat Commun 5, 5643. https://doi.org/10.1038/ncomms6643

Warrington, E.K., Logue, V., Pratt, R.T., 1971. The anatomical localisation of selective impairment of auditory verbal short-term memory. Neuropsychologia 9, 377–387. https://doi.org/10.1016/0028-3932(71)90002-9

Weissman, D.H., Roberts, K.C., Visscher, K.M., Woldorff, M.G., 2006. The neural bases of momentary lapses in attention. Nat Neurosci 9, 971–978. https://doi.org/10.1038/nn1727

Whitlock, J.R., Sutherland, R.J., Witter, M.P., Moser, M.-B., Moser, E.I., 2008. Navigating from hippocampus to parietal cortex. Proceedings of the National Academy of Sciences 105, 14755–14762. https://doi.org/10.1073/pnas.0804216105

Wickersham, I.R., Lyon, D.C., Barnard, R.J.O., Mori, T., Finke, S., Conzelmann, K.-K., Young, J.A.T., Callaway, E.M., 2007. Monosynaptic Restriction of Transsynaptic Tracing from Single, Genetically Targeted Neurons. Neuron 53, 639–647. https://doi.org/10.1016/j.neuron.2007.01.033

Wietek, J., Rodriguez-Rozada, S., Tutas, J., Tenedini, F., Grimm, C., Oertner, T.G., Soba, P., Hegemann, P., Wiegert, J.S., 2017. Anion-conducting channelrhodopsins with tuned spectra and modified kinetics engineered for optogenetic manipulation of behavior. Sci Rep 7, 14957. https://doi.org/10.1038/s41598-017-14330-y

Wilber, A.A., Clark, B.J., Demecha, A.J., Mesina, L., Vos, J.M., McNaughton, B.L., 2014. Cortical connectivity maps reveal anatomically distinct areas in the parietal cortex of the rat. Front Neural Circuits 8, 146. https://doi.org/10.3389/fncir.2014.00146

Williams, S.R., Stuart, G.J., 1999. Mechanisms and consequences of action potential burst firing in rat neocortical pyramidal neurons. J Physiol 521, 467–482. https://doi.org/10.1111/j.1469-7793.1999.00467.x

Wilson, B.A., Berry, E., Gracey, F., Harrison, C., Stow, I., Macniven, J., Weatherley, J., Young, A.W., 2005. Egocentric Disorientation following Bilateral Parietal Lobe Damage. Cortex 41, 547–554. https://doi.org/10.1016/S0010-9452(08)70194-1

Wong, R.K., Prince, D.A., 1978. Participation of calcium spikes during intrinsic burst firing in hippocampal neurons. Brain Res 159, 385–390. https://doi.org/10.1016/0006-8993(78)90544-9

Xia, S., Yu, J., Huang, X., Sesack, S.R., Huang, Y.H., Schlüter, O.M., Cao, J.-L., Dong, Y., 2020. Cortical and Thalamic Interaction with Amygdala-to-Accumbens Synapses. J. Neurosci. 40, 7119–7132. https://doi.org/10.1523/JNEUROSCI.1121-20.2020

Xin, Q., Zhang, W., Yuan, S., 2023. The Mechanism of the Channel Opening in Channelrhodopsin-2: A Molecular Dynamics Simulation. International Journal of Molecular Sciences 24, 5667. https://doi.org/10.3390/ijms24065667

Xu, N., Harnett, M.T., Williams, S.R., Huber, D., O'Connor, D.H., Svoboda, K., Magee, J.C., 2012. Nonlinear dendritic integration of sensory and motor input during an active sensing task. Nature 492, 247–251. https://doi.org/10.1038/nature11601

Yamashita, T., Petersen, C.C., 2016. Target-specific membrane potential dynamics of neocortical projection neurons during goal-directed behavior. eLife 5, e15798. https://doi.org/10.7554/eLife.15798

Yang, C.R., Seamans, J.K., Gorelova, N., 1996. Electrophysiological and morphological properties of layers V-VI principal pyramidal cells in rat prefrontal cortex in vitro. J. Neurosci. 16, 1904–1921. https://doi.org/10.1523/JNEUROSCI.16-05-01904.1996

Yang, W., Carrasquillo, Y., Hooks, B.M., Nerbonne, J.M., Burkhalter, A., 2013. Distinct Balance of Excitation and Inhibition in an Interareal Feedforward and Feedback Circuit of Mouse Visual Cortex. J. Neurosci. 33, 17373–17384. https://doi.org/10.1523/JNEUROSCI.2515-13.2013

Yang, W., Carrillo-Reid, L., Bando, Y., Peterka, D.S., Yuste, R., 2018. Simultaneous two-photon imaging and two-photon optogenetics of cortical circuits in three dimensions. eLife 7, e32671. https://doi.org/10.7554/eLife.32671

Yarkoni, T., Gray, J.R., Chrastil, E.R., Barch, D.M., Green, L., Braver, T.S., 2005. Sustained neural activity associated with cognitive control during temporally extended decision making. Brain Res Cogn Brain Res 23, 71–84. https://doi.org/10.1016/j.cogbrainres.2005.01.013

Yizhar, O., Fenno, L.E., Prigge, M., Schneider, F., Davidson, T.J., O'Shea, D.J., Sohal, V.S., Goshen, I., Finkelstein, J., Paz, J.T., Stehfest, K., Fudim, R., Ramakrishnan, C., Huguenard, J.R., Hegemann, P., Deisseroth, K., 2011. Neocortical excitation/inhibition balance in information processing and social dysfunction. Nature 477, 171–178. https://doi.org/10.1038/nature10360

Zajonc, R.B., 1968. Attitudinal effects of mere exposure. Journal of Personality and Social Psychology 9, 1–27. https://doi.org/10.1037/h0025848

Zanto, T.P., Rubens, M.T., Thangavel, A., Gazzaley, A., 2011. Causal role of the prefrontal cortex in top-down modulation of visual processing and working memory. Nat Neurosci 14, 656–661. https://doi.org/10.1038/nn.2773

Zeng, F.-G., Rebscher, S., Harrison, W., Sun, X., Feng, H., 2008. Cochlear implants: system design, integration, and evaluation. IEEE Rev Biomed Eng 1, 115–142. https://doi.org/10.1109/RBME.2008.2008250

Zhang, F., Gradinaru, V., Adamantidis, A.R., Durand, R., Airan, R.D., de Lecea, L., Deisseroth, K., 2010. Optogenetic interrogation of neural circuits: technology for probing mammalian brain structures. Nat Protoc 5, 439–456. https://doi.org/10.1038/nprot.2009.226

Zhang, F., Prigge, M., Beyrière, F., Tsunoda, S.P., Mattis, J., Yizhar, O., Hegemann, P., Deisseroth, K., 2008. Red-shifted optogenetic excitation: a tool for fast neural control derived from Volvox carteri. Nat Neurosci 11, 631–633. https://doi.org/10.1038/nn.2120

Zhang, F., Wang, L.-P., Brauner, M., Liewald, J.F., Kay, K., Watzke, N., Wood, P.G., Bamberg, E., Nagel, G., Gottschalk, A., Deisseroth, K., 2007. Multimodal fast optical interrogation of neural circuitry. Nature 446, 633–639. https://doi.org/10.1038/nature05744

Zhang, S., Xu, M., Chang, W.-C., Ma, C., Hoang Do, J.P., Jeong, D., Lei, T., Fan, J.L., Dan, Y., 2016. Organization of long-range inputs and outputs of frontal cortex for top-down control. Nat Neurosci 19, 1733–1742. https://doi.org/10.1038/nn.4417

Zhang, S., Xu, M., Kamigaki, T., Hoang Do, J.P., Chang, W.-C., Jenvay, S., Miyamichi, K., Luo, L., Dan, Y., 2014. Selective attention. Long-range and local circuits for top-down modulation of visual cortex processing. Science 345, 660–665. https://doi.org/10.1126/science.1254126

Zhang, Y., Rózsa, M., Liang, Y., Bushey, D., Wei, Z., Zheng, J., Reep, D., Broussard, G.J., Tsang, A., Tsegaye, G., Narayan, S., Obara, C.J., Lim, J.-X., Patel, R., Zhang, R., Ahrens, M.B., Turner, G.C., Wang, S.S.-H., Korff, W.L., Schreiter, E.R., Svoboda, K., Hasseman, J.P., Kolb, I., Looger, L.L., 2023. Fast and sensitive GCaMP calcium indicators for imaging neural populations. Nature 615, 884–891. https://doi.org/10.1038/s41586-023-05828-9

Zhang, Z., Reboreda, A., Alonso, A., Barker, P.A., Séguéla, P., 2011. TRPC channels underlie cholinergic plateau potentials and persistent activity in entorhinal cortex. Hippocampus 21, 386–397. https://doi.org/10.1002/hipo.20755

Zhao, Y., Araki, S., Wu, J., Teramoto, T., Chang, Y.-F., Nakano, M., Abdelfattah, A.S., Fujiwara, M., Ishihara, T., Nagai, T., Campbell, R.E., 2011. An Expanded Palette of Genetically Encoded Ca2+ Indicators. Science 333, 1888–1891. https://doi.org/10.1126/science.1208592

Zhong, L., Zhang, Y., Duan, C.A., Deng, J., Pan, J., Xu, N.-L., 2019. Causal contributions of parietal cortex to perceptual decision-making during stimulus categorization. Nat Neurosci 22, 963–973. https://doi.org/10.1038/s41593-019-0383-6

Zhou, Y., Freedman, D.J., 2019. Posterior parietal cortex plays a causal role in perceptual and categorical decisions. Science 365, 180–185. https://doi.org/10.1126/science.aaw8347

Zingg, B., Hintiryan, H., Gou, L., Song, M.Y., Bay, M., Bienkowski, M.S., Foster, N.N., Yamashita, S., Bowman, I., Toga, A.W., Dong, H.-W., 2014. Neural networks of the mouse neocortex. Cell 156, 1096–1111. https://doi.org/10.1016/j.cell.2014.02.023

Zomorrodi, R., Kröger, H., Timofeev, I., 2008. Modeling thalamocortical cell: impact of Ca2+ channel distribution and cell geometry on firing pattern. Frontiers in Computational Neuroscience 2.